POLITECNICO
MILANO 1863

SCUOLA DI INGEGNERIA INDUSTRIALE
E DELL'INFORMAZIONE

Ground Resonance Sensitivity Study for Unconventional Damper Configurations

Tesi di Laurea Magistrale in
Aeronautical Engineering - Ingegneria Aeronautica

Author: **Matteo Croci**

Student ID: 10677311
Advisor: Prof. Pierangelo Masarati
Academic Year: 2024-25

Abstract

This thesis further explores and investigates the innovative concept of the Inter-2-Blade (I2B) lead-lag damper arrangement for helicopter rotors. In order to obtain a model comparable to the conventional Inter-Blade (IB) configuration, I2B models are derived by exploiting eigenvalue sensitivity analysis and continuation methods applied to the ground resonance equations.

The work first presents a formal derivation of the sensitivity method applied to the ground resonance problem. This methodology is then applied to the so-called Hammond problem, demonstrating its capability to guide modifications of the geometry in the I2B configuration. By adjusting the geometrical characteristics of the damper, the method provides valuable insights to enhance system stability, introduce additional damping in critical modes, and mitigate previously undamped behaviors.

Subsequently, a general modeling framework is proposed, capable of assembling the coupled rotor-airframe system independently of the specific damper architecture or kinematic assumptions. Within this framework, two detailed kinematic models are developed: one representative of a modern medium-weight helicopter with the IB configuration, and the other adopting the I2B configuration. By applying the sensitivity-based approach, equivalent models are obtained by tuning the damper stiffness and damping coefficients, yielding an I2B model with improved damping characteristics on collective mode.

Finally, the damper configurations studied are implemented in MASST, an industrial-grade tool designed to simulate complex dynamic systems, where a comparison between the obtained results is performed.

This work represents a step forward in the study of this novel damper architecture, exploiting eigenvalue sensitivity analysis to derive comparable models for the I2B configuration with respect to the conventional IB configuration, while employing more detailed and realistic kinematic representations.

Keywords: Rotorcraft dynamics, Ground Resonance, Inter-blade damping, MASST, Helicopter Stability

Abstract in lingua italiana

La presente tesi analizza il concetto innovativo della configurazione Inter-2-Blade (I2B) per gli smorzatori di ritardo nei rotori di elicottero. Al fine di ottenere modelli comparabili con la configurazione convenzionale Inter-Blade (IB), vengono applicati l'analisi di sensibilità degli autovalori e i metodi di continuazione alle equazioni della risonanza al suolo.

Viene dapprima presentata la derivazione formale del metodo di sensibilità, applicata successivamente al problema di Hammond, dimostrando la capacità della metodologia di guidare le modifiche geometriche nella configurazione I2B. L'adattamento delle caratteristiche geometriche dello smorzatore consente di migliorare la stabilità del sistema, aumentare lo smorzamento nei modi critici e attenuare comportamenti precedentemente non smorzati.

Viene quindi proposto un modello generale per il sistema accoppiato rotore-fusoliera, indipendente dall'architettura dello smorzatore e dalle ipotesi cinematiche adottate. All'interno di tale framework sono sviluppati due modelli dettagliati: uno rappresentativo di un elicottero moderno con configurazione IB e uno con configurazione I2B. Regolando i coefficienti di rigidezza e smorzamento tramite l'approccio di sensibilità, si ottiene un modello I2B con migliorato smorzamento sul modo collettivo.

Infine, le configurazioni analizzate sono implementate in MASST, un software industriale per la simulazione di sistemi dinamici complessi, consentendo il confronto tra i risultati.

Il lavoro rappresenta un avanzamento nello studio di questa nuova architettura di smorzatori, sfruttando l'analisi di sensibilità degli autovalori per ottenere modelli equivalenti per la configurazione I2B rispetto a quella convenzionale IB, mediante modelli cinematici più dettagliati e realistici.

Parole chiave: Dinamica del rotore, Risonanza al suolo, Smorzamento inter-blade, MASST, Stabilità degli elicotteri

Contents

1 | Introduction

1.1. General Overview

A critical factor in ensuring the safe operation of rotorcraft is the stability of the vehicle during two particularly sensitive flight phases: take-off and landing.

In both cases, the rotor's angular velocity transitions through the full range of rotational speeds, from a complete stop up to nominal operating RPM during take-off, and the reverse during landing.

Throughout these transitions, even minor imbalances in the rotor or blade masses, or small disturbances in the system, can trigger a dynamic interaction between the spinning rotor and the stationary airframe resting on the landing gear. This interaction may lead to a phenomenon known as ground resonance a self-excited instability that, if not promptly addressed, can rapidly grow in intensity and result in serious structural damage or the destruction of the entire rotorcraft.

The phenomenon was first identified in the first half of the twentieth century, and thanks to the pioneering analytical work of Coleman and Hammond [3], it is now a well-understood aspect of rotorcraft dynamics. Modern helicopters are specifically designed to prevent ground resonance through a combination of mechanical dampers, optimized landing gear stiffness, rigorous maintenance protocols, and simulation-based certification processes; nonetheless, this phenomenon is crucial for satisfying stability requirements and represents a fundamental aspect of helicopter certification.

Ground resonance primarily occurs in fully articulated rotor systems, where each blade is free to flap, drag (lead-lag), and feather independently. Among these motions, the lead-lag (or drag) motion—commonly denoted by $\boldsymbol{\xi}$—plays a critical role in triggering the instability. An unbalanced or asymmetric lag response can couple with the natural frequency of the landing gear system, setting up conditions for a self-excited resonance.

The mechanism of ground resonance is inherently mechanical: it does not require aerodynamic forces to develop and is typically triggered while the helicopter is on the ground

with the rotor spinning. Small asymmetries or perturbations—such as blade lead-lag displacements—can initiate the instability. If the damping system is inadequate, the phase lag between blade motion and fuselage response may cause energy to be fed back into the system rather than being dissipated. Figure 1.1 shows still images from a ground resonance test intentionally conducted to trigger the phenomenon on a CH-47 helicopter. The full video is available in [16].

Figure 1.1: Ground resonance test in a Boeing CH-47 Chinook helicopter, source in [16].

The key components responsible for controlling this phenomenon are the lead-lag dampers. These devices are specifically designed to attenuate the motion of the blades in the lead-lag direction, which lies within the rotor plane. By suppressing excessive lead-lag oscillations, the dampers play a crucial role in preventing the onset of instability and the development of large-amplitude vibrations that could lead to ground resonance.

Lead-lag dampers can operate based on different mechanisms, including mechanical or viscoelastic principles. Regardless of the damping technology employed, one of the most critical aspects—and a central topic of this thesis—is the arrangement of the dampers. In this context, "arrangement" refers to the specific blade or blades on which the dampers are mounted, and how this configuration influences the dynamic behavior of the rotor system.

Damper configuration plays a crucial role in mitigating this instability. By providing sufficient in-plane damping, particularly to the regressive modes of the rotor, dampers can effectively suppress the onset of ground resonance. In this context, the correct tuning of damper parameters (stiffness and damping coefficients), their geometrical placement, and their topological arrangement (e.g., BTH, IB, I2B) are all critical.

Certification standards, such as CS 29.251 [6], mandate that no instability may occur in the full operational range of rotor speeds—from 40% to 120% of the nominal rotational speed. As stated in CS 29.251 [6]:

> "The applicant should investigate each individual installation of the rotorcraft for compliance with CS 29.251. The absence of coupling with the rotor's vibration frequencies should be demonstrated by a combination of analysis, vibration and flight tests. Qualitative and quantitative flight tests should be performed depending on the extent of the change. For any installation, the failure of which or its attachment would have a catastrophic consequence, a fatigue evaluation should be performed when the vibrations are likely to affect the fatigue strength."

This ensures a robust margin of safety not only during steady-state operation but also during transient phases such as take-off and landing, where the rotor may pass through resonance conditions.

1.2. Damping Arrangements

The most widely used blade damper configuration in helicopter rotors is the so-called Blade-To-Hub (BTH) arrangement, in which each damper connects the corresponding blade directly to the rotor hub. This configuration, the first historically adopted, from a mechanical standpoint enables a straightforward force transmission path and simplifies the design of the damper housing and attachments, which can be integrated into the hub or pitch horn structure. Damping forces are typically generated through hydraulic or elastomeric elements designed to dissipate energy over a range of lead-lag displacements and frequencies. An example of BTH arrangement with a hydraulic arm is reported in the figure below Fig. 1.2.

Figure 1.2: Four-blade rotor with blade-to-hub arrangement of a Sikorsky MH-60 helicopter, source in [10].

The consequent evolution of the BTH configuration is called Interblade (IB), in which each damper connects two adjacent blades, without any direct connection between the dampers and the rotor hub. This configuration represents a significant topological evolution in the distribution of damping forces, as it relies exclusively on the relative in-plane motion between adjacent blades to induce energy dissipation. Compared to the BTH arrangement, the IB configuration offers several advantages. Since damping in each blade is governed by its motion relative to the preceding and following blades, the required damping coefficients are typically lower than those used in BTH systems. Additionally, relocating the dampers away from the rotor center leads to a mechanically simpler rotor architecture. The absence of a direct connection to the hub alleviates interference with pitch control mechanisms, such as the swashplate and pitch links, thereby easing mechanical integration and offering increased design flexibility for damper placement and tuning.

Despite these advantages, the IB configuration introduces its own set of design challenges. It necessitates precise control of phasing and positioning between adjacent blades. Moreover, the lack of direct damping at the hub limits the system's ability to effectively attenuate pure collective in-plane modes, unless asymmetries or specific stiffness distributions are deliberately introduced into the design.

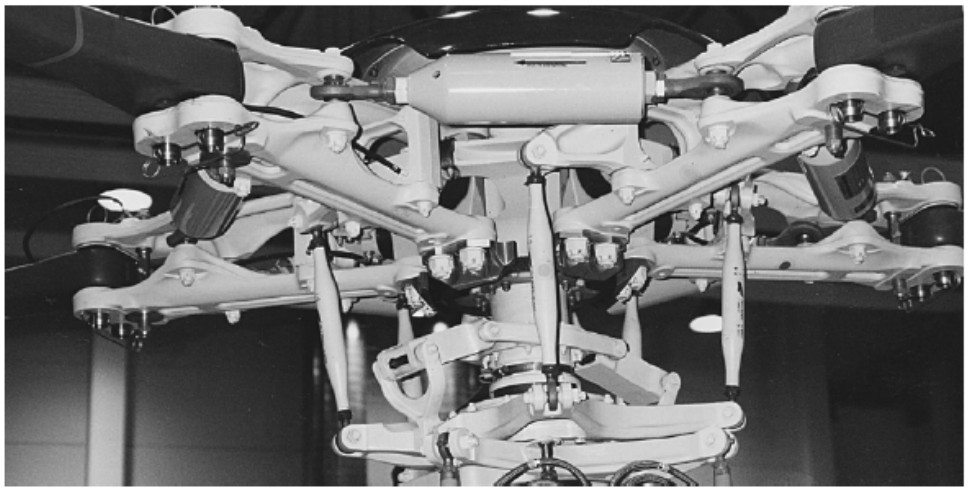

Figure 1.3: Close view of the main rotor of the Eurocopter EC155 with inter-blade damping, source in [11].

Recently a configuration called Inter-2-Blade (I2B) has been proposed [7, 13]. In this arrangement, each damper connects two non-adjacent blades through a complex kinematic arrangement. The I2B configuration aims to combine the benefits of the IB, reduced damper loads, and decoupling from hub kinematics, with an improved ability to damp cyclic in-plane modes, at the cost of a slightly more complex kinematics.

By coupling non-neighboring blades, the I2B layout allows for damping forces to act on global motion patterns of the rotor, including both collective and regressive modes. Furthermore, the I2B configuration can offer greater flexibility in damper placement and leverage longer kinematic arms, which may reduce the required stiffness and damping coefficients while maintaining effectiveness. However, this solution comes with increased mechanical complexity and requires precise alignment and synchronization of the kinematic system to ensure consistent performance across all blades.

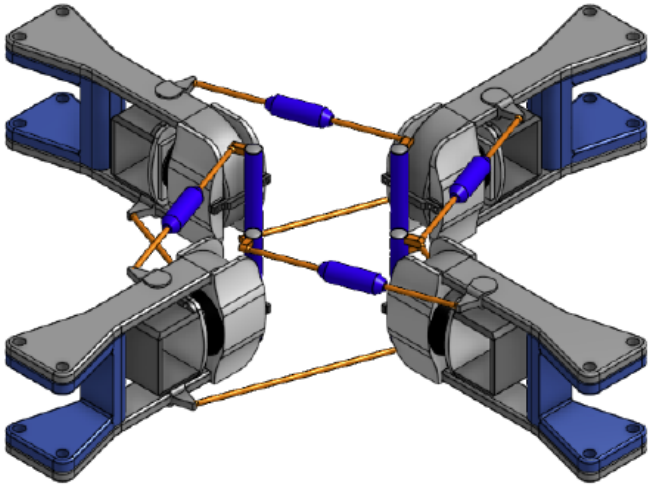

Figure 1.4: Render of a four-blade rotor scheme with I2B arrangement, as shown on page 73 of the thesis [8].

1.3. Description of the Thesis

This work represents the third thesis chronologically focused on the innovative Inter-2-Blade (I2B) damper configuration. The first thesis [8] laid the mathematical foundation for the I2B kinematic arrangement and developed the governing equations of motion. The second thesis [1] extended this work by conducting a more detailed performance analysis using numerical models in MATLAB and MBDyn. It explored load sensitivity and identified an optimal geometric configuration, which serves as the starting point for the present study.

In Chapter 2, are described the general equation of lag motion that leads to the ground resonance problem, and their subsequent expression for the IB configuration and I2B configuration, both in nominal and failure condition of the dampers.

In Chapter 3 with the geometry defined in the previous thesis and referencing the Hammond dataset—commonly used for preliminary assessments of rotor system behavior—a mathematical framework is introduced to investigate the impact of geometric parameters on the GR problem. This is achieved by developing a mathematical approach that exploits the sensitivity of eigenvalues to the main geometrical elements. The analysis is performed for the nominal GR scenario, where all dampers are operative (ADO). Sensitivity analyses were carried out not only to asses the evolution of the eigenvalues but also to investigate the loads transmitted from the dampers to the rotor hub (Appendix C).

These calculations allow a more comprehensive understanding of how geometry affects both dynamic stability and structural load paths.

All sensitivity results were validated, and comparisons between the predictions of the sensitivity-based model and those of full simulations using modified geometries are reported in Appendix B.

In Chapter 4, to extend the study toward more realistic applications and enable a deeper comparison between different damper arrangements, a theoretical framework was initially developed to model arbitrary kinematic configurations and damper arrangements. This provided the foundation for generating realistic kinematic models, each based on parameters representative of a modern medium-weight helicopter.

Based on these models, the global governing equations for the ground resonance problem are formulated and analyzed under both nominal and damper-failure conditions. Leveraging the insights from the two-dimensional kinematic analysis, a refined geometry for the I2B configuration is selected. This geometry is capable of replicating the dynamic behavior of the IB setup while also introducing damping on the collective lag mode, which was previously undamped. The design of this configuration is guided by the sensitivity-based approach presented in Chapter 3.

Subsequently, the damper configurations are tuned to provide comparable damping characteristics for selected MBC modes. These configurations are then evaluated under both nominal and failure scenarios of the ground resonance problem. The final comparison highlights the improved robustness and damping performance offered by the I2B architecture.

This enabled the development and comparison, presented in Chapter 5, of kinematic models in which both the IB and I2B geometries are implemented in MASST, a modern aeroelastic simulation environment. This implementation allows for a more in-depth assessment of the performance and integration of the proposed damper architectures under realistic operating conditions.

2 | Ground Resonance Problem

As explained in the introduction, the ground resonance problem involves the coupling between the in-plane lag movement of the blade and the in-plane hub movement. Considering only the lead-lag movement of a blade, mounted on a flexible support, as done by the work of Coleman [3, 4], the ground resonance problem can be developed.

2.1. Lag Motion of the Blade with Center Hub Movement

Regarding the blade equations, the dynamics of the blades can be obtained by applying the Lagrange formalism of the articulated rotor, as shown in Fig. 2.1, from [9].

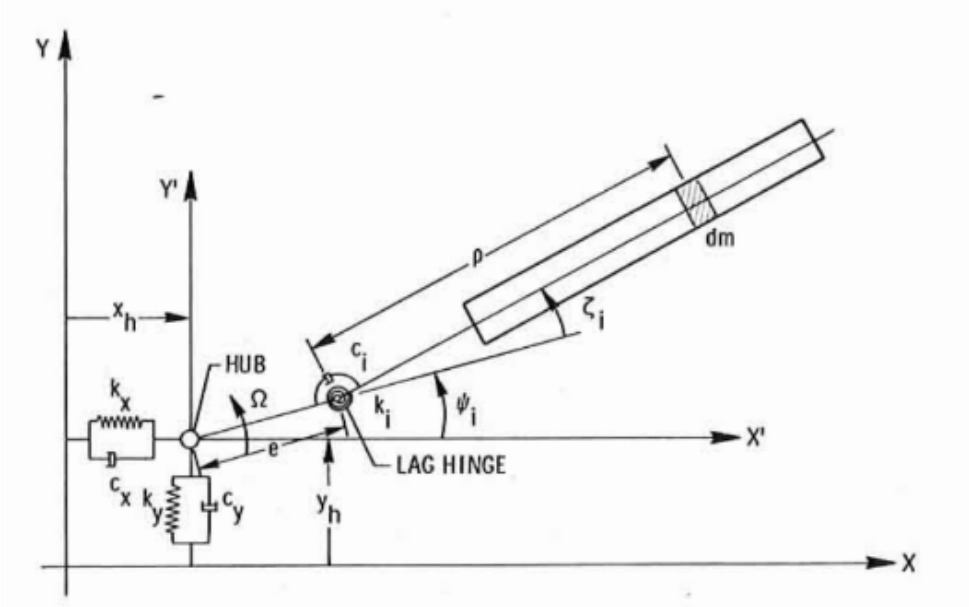

Figure 2.1: Sketch of a single blade mounted on a flexible support, from [9], p. 15.

The absolute position of the center of mass of the blade is:

$$\mathbf{p}_{\mathrm{CM}}^{(m)} = \begin{Bmatrix} x \\ y \end{Bmatrix} + e \begin{Bmatrix} \cos\psi^{(m)} \\ \sin\psi^{(m)} \end{Bmatrix} + r_{\mathrm{CM}} \begin{Bmatrix} \cos\left(\psi^{(m)} + \xi^{(m)}\right) \\ \sin\left(\psi^{(m)} + \xi^{(m)}\right) \end{Bmatrix}. \tag{2.1}$$

The following notation will be used in the document. The apex (m) stand for the m blade, the lag angle of the mth blade will be expressed as: $\psi^{(m)} = \psi + m\Delta\psi$ with $\Delta\psi = 2\pi/N_{\mathrm{blades}}$.

Once the absolute position of the center of mass is obtained, the velocity can be retrieved deriving respect time, and so under the approximation of small lag angle, the kinetic energy of the mth blade can be computed. Applying the Lagrange formalism respect the blade coordinate $\xi^{(m)}$ the blade equation can be obtained.

Without loss of generality, the expression governing the lag motion of blade m, under the assumption of small lag angle, $|\xi^{(m)}| << 1$, so:

$$\cos(\psi^{(m)} + \xi^{(m)}) \approx \cos\psi^{(m)} - \xi^{(m)}\sin\psi^{(m)} \tag{2.2a}$$

$$\sin(\psi^{(m)} + \xi^{(m)}) \approx \sin\psi^{(m)} + \xi^{(m)}\cos\psi^{(m)}, \tag{2.2b}$$

is given by:

$$J_\xi\,\ddot{\xi}^{(m)} + C_\xi\,\dot{\xi}^{(m)} + \left(K_\xi + \Omega^2 e S_\xi\right)\,\xi^{(m)} + S_\xi\,\ddot{y}\cos\psi^{(m)} - S_\xi\,\ddot{x}\sin\psi^{(m)} = 0. \tag{2.3}$$

The development of the GR equations without the assumption of small lead-lag angles can be found in [2].

The terms C_ξ and K_ξ denote the damping and stiffness contributions associated with the linear visco-elastic lead-lag damper. These dampers are modeled as BTH, as they act exclusively on the lag rotation of each individual blade.

It is worth noting that the lag dynamics are influenced by the hub translational motion. This component, which depends on the azimuth angle $\psi^{(m)}$, plays a crucial role in ground resonance phenomena, as it introduces coupling between the blade lag motion and the hub displacement.

2.2. Motion of the Airframe

The equations governing the airframe dynamics can be derived by applying the Lagrangian formalism with respect to the airframe coordinates x and y, which represent the in-plane displacement of the hub center.

The expression for the airframe dynamics is given by:

$$\begin{aligned}
&\mathbf{M}_a \begin{Bmatrix} \ddot{x} \\ \ddot{y} \end{Bmatrix} + \mathbf{C}_a \begin{Bmatrix} \dot{x} \\ \dot{y} \end{Bmatrix} + \mathbf{K}_a \begin{Bmatrix} x \\ y \end{Bmatrix} \\
&+ S_\xi \sum_{m=1}^{N_b} \begin{Bmatrix} -\sin\psi^{(m)} \\ \cos\psi^{(m)} \end{Bmatrix} \ddot{\xi}^{(m)} - 2\Omega S_\xi \sum_{m=1}^{N_b} \begin{Bmatrix} \cos\psi^{(m)} \\ \sin\psi^{(m)} \end{Bmatrix} \dot{\xi}^{(m)} \\
&+ \Omega^2 S_\xi \sum_{m=1}^{N_b} \begin{Bmatrix} \sin\psi^{(m)} \\ -\cos\psi^{(m)} \end{Bmatrix} \xi^{(m)} = \begin{Bmatrix} 0 \\ 0 \end{Bmatrix}.
\end{aligned} \tag{2.4}$$

The properties of the airframe are condensed in the matrices of Eq. (2.4). In the airframe mass matrix $\mathbf{M}_a$ is present the generalized mass coefficient reduced to the motion of the hub center, including the mass of the blades. In the damping matrix $\mathbf{C}_a$, the effective hub damping in x and y direction, and in the stiffness matrix $\mathbf{K}_a$, the effective hub stiffness along x and y.

As stated in Eq. (2.3), the problem is clearly coupled: the in-plane displacement of the hub center interacts dynamically with the lag motion of the blades.

The complete system, obtained by assembling the contributions of all blades and the airframe, can be rewritten as:

$$\hat{\mathbf{M}}_b\, \ddot{\hat{\mathbf{q}}}_b + \hat{\mathbf{C}}_b\, \dot{\hat{\mathbf{q}}}_b + \hat{\mathbf{K}}_b\, \hat{\mathbf{q}}_b + \hat{\mathbf{S}}_b\, \ddot{\mathbf{q}}_a = \mathbf{0} \tag{2.5a}$$

$$\mathbf{M}_a\, \ddot{\mathbf{q}}_a + \mathbf{C}_a\, \dot{\mathbf{q}}_a + \mathbf{K}_a\, \mathbf{q}_a + \hat{\mathbf{S}}_b^T\, \ddot{\hat{\mathbf{q}}}_b + 2\dot{\hat{\mathbf{S}}}_b^T\, \dot{\hat{\mathbf{q}}}_b + \ddot{\hat{\mathbf{S}}}_b^T\, \hat{\mathbf{q}}_b = \mathbf{0} \tag{2.5b}$$

The detailed derivation and theoretical foundations of these equations can be found in [9, 12].

Inside the blade matrices of Eq. (2.5a), are reported, along the main diagonal the contribute of each blade, as written in Eq. (2.3). The term $\hat{\mathbf{S}}_b$ consider the motion of the hub center, that acts as an azimuth dependent forcing term for each blade. It is important to note that the system has a number of degrees of freedom equal to the number of blades $\hat{\mathbf{q}}_b$, plus the two in-plane motions of the hub center $\mathbf{q}_a$. Moreover, the system is described by differential equations with periodic coefficients, due to the azimuth dependent terms associated with each blade, the dependence is denoted by the term $\hat{}$.

2.3. Multiblade Coordinates Transformation

The periodic coefficients differential equation that describes the dynamics of the coupled blade–airframe system can be converted into a non-periodic differential equation by introducing the multiblade coordinate transformation. In fact, due to the isotropy of the rotor, the system described by (2.5) can become azimuth-independent.

The concept of multiblade coordinates was first introduced by Coleman in [3, 4].

Defining the lag angles of the mth blade as the sum of N_c components, where $N_c = N_b/2-1$ when N_b is even, and $N_c = (N_b - 1)/2$ when N_b is odd:

$$\xi^{(m)} = \xi_0 + \sum_{n=1}^{N_c} [\cos(n\psi^{(m)})\, \xi_{n_c} + \sin(n\psi^{(m)})\, \xi_{n_s}] + (-1)^m \xi_{N_b/2} \tag{2.6}$$

The lag angles, one for each blade, which are the unknowns of the problem related to lag dynamics, can be transformed, exploiting the multiblade formulation, into multiblades coordinates, now azimuth-independent, through the transformation matrix $\mathbf{T}(\psi)$.

$$\begin{Bmatrix} \xi^{(1)} \\ \xi^{(2)} \\ \cdots \\ \xi^{(N_b)} \end{Bmatrix} = \begin{bmatrix} 1 & \cos\psi_1 & \sin\psi_1 & \cos(2\psi_1) & \sin(2\psi_1) & \cdots & -1 \\ 1 & \cos\psi_2 & \sin\psi_2 & \cos(2\psi_2) & \sin(2\psi_2) & \cdots & -1 \\ \vdots & & & & & & \vdots \\ 1 & \cos\psi_{N_b} & \sin\psi_{N_b} & \cos(2\psi_{N_b}) & \sin(2\psi_{N_b}) & \cdots & -1 \end{bmatrix} \begin{Bmatrix} \xi_0 \\ \xi_{1c} \\ \xi_{1s} \\ \xi_{2c} \\ \xi_{2s} \\ \cdots \\ \xi_{N_b/2} \end{Bmatrix} \tag{2.7}$$

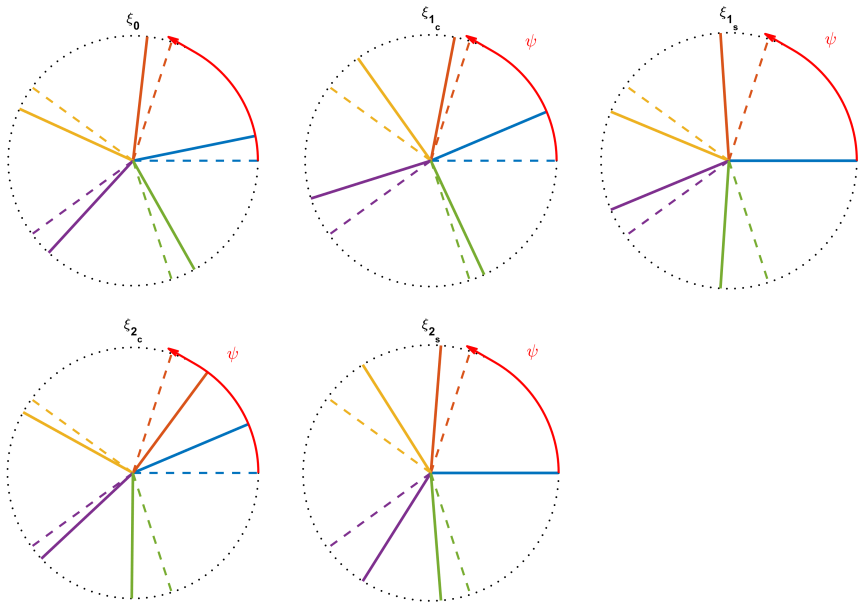

Figure 2.2: MBC for a 5 blades rotor.

The number of unknowns of the problem remain unchanged, since after the multiblade transformation they are still $N_b + 2$. Through the MBCT the unknowns of the blade problem are no more the lead-lag rotations of the blades $\hat{\mathbf{q}}_b$ but the multiblade coordinates $\mathbf{q}_b$, which can be visualized, for a five-blade rotor in Fig. 2.2, where the corresponding transformation is:

$$\hat{\mathbf{q}}_b = \mathbf{T}(\psi)\mathbf{q}_b \tag{2.8}$$

The multiblade coordinate transformation can be applied to the system of Eqs. (2.5) leading to:

$$\begin{aligned} &\mathbf{T}^T \hat{\mathbf{M}}_b \mathbf{T} \ddot{\mathbf{q}}_b + \mathbf{T}^T \left(\hat{\mathbf{C}}_b \mathbf{T} + 2\hat{\mathbf{M}}_b \dot{\mathbf{T}}\right) \dot{\mathbf{q}}_b \\ &+ \mathbf{T}^T \left(\hat{\mathbf{K}}_b \mathbf{T} + \hat{\mathbf{C}}_b \dot{\mathbf{T}} + \hat{\mathbf{M}}_b \ddot{\mathbf{T}}\right) \mathbf{q}_b + \mathbf{T}^T \hat{\mathbf{S}}_b \ddot{\mathbf{q}}_a = \mathbf{0} \end{aligned} \tag{2.9a}$$

$$\mathbf{M}_a \ddot{\mathbf{q}}_a + \mathbf{C}_a \dot{\mathbf{q}}_a + \mathbf{K}_a \mathbf{q}_a + \hat{\mathbf{S}}_b^T \mathbf{T} \ddot{\mathbf{q}}_b = \mathbf{0} \tag{2.9b}$$

The mass, damping, and stiffness matrices transformed through the multiblade transformation becomes diagonal and block-diagonal matrices, as shown in Eq. 2.9a. All these matrices are constant, since the azimuthal dependence has been eliminated thanks to the isotropy of the blades.

Depending on the architecture of the dampers employed, the formulation of the damping and stiffness matrix $\hat{\mathbf{C}}_b$, $\hat{\mathbf{K}}_b$ will exhibit a different structure. This aspect plays a critical role in the damping of the critical multiblade modes, as will be discussed later.

2.3.1. Blade to Hub Ground Resonance Formulation

The general expression of the damping matrix, in the non-rotating frame of reference, can be derived from the application of the Principle of Virtual Work (PVW) of the damper.

$$\Delta\xi^{(m)} = \xi^{(m)}, \tag{2.10}$$

due to the BTH configuration, see Fig. 1.2, the rotation of the damper coincides with the blade lag rotation. The virtual work of the damper can be written as:

$$\delta\mathcal{W}_{\text{damper}} = -\delta\Delta\xi^{(m)}\, c_\xi\, \Delta\dot{\xi}^{(m)} - \delta\Delta\xi^{(m)}\, k_\xi\, \Delta\xi^{(m)} = -(\delta\xi^{(m)})c_\xi(\dot{\xi}^{(m)}) - (\delta\xi^{(m)})k_\xi(\xi^{(m)}), \tag{2.11}$$

the expression of the damping and stiffness matrix in the rotating frame is thus a diagonal matrix, where each term corresponds to the stiffness and damping coefficient of the damper on blade m.

The portion of the problem related to the ground resonance phenomenon involves the first pair of cyclic equations, ξ_{1_c} and ξ_{1_s}, together with the in-plane motion of the airframe, x and y:

$$\mathbf{M}_{\text{GR, BTH}} = \begin{bmatrix} N_b I_\xi/2 & 0 & 0 & N_b S_\xi/2 \\ 0 & N_b I_\xi/2 & -N_b S_\xi/2 & 0 \\ 0 & -N_b S_\xi/2 & M_x + N_b M & 0 \\ N_b S_\xi/2 & 0 & 0 & M_y + N_b M \end{bmatrix} \tag{2.12}$$

$$\mathbf{C}_{\text{GR, BTH}} = \begin{bmatrix} N_b c_\xi/2 & N_b I_b \Omega & 0 & 0 \\ -N_b I_b \Omega & N_b c_\xi/2 & 0 & 0 \\ 0 & 0 & C_x & 0 \\ 0 & 0 & 0 & C_y \end{bmatrix} \tag{2.13}$$

$$\mathbf{K}_{\text{GR, BTH}} = \begin{bmatrix} N_b[k_\xi - (I_\xi - eS_\xi)\Omega^2]/2 & N_b\Omega c_\xi/2 & 0 & 0 \\ -N_b\Omega c_\xi/2 & N_b[k_\xi - (I_\xi - eS_\xi)\Omega^2]/2 & 0 & 0 \\ 0 & 0 & K_x & 0 \\ 0 & 0 & 0 & K_y \end{bmatrix} \tag{2.14}$$

2.3.2. Interblade Ground Resonance Formulation

For this arrangement, the relative motion of the damper's parts is the difference between the rotations of adjacent blades:

$$\Delta\xi^{(m)} = \xi^{(m+1)} - \xi^{(m)}, \tag{2.15}$$

the virtual work of the damper now takes the form:

$$\begin{aligned} \delta\mathcal{W}_{\text{damper}} &= -\delta\Delta\xi^{(m)}\, c_\xi\, \Delta\dot{\xi}^{(m)} - \delta\Delta\xi^{(m)}\, k_\xi\, \Delta\xi^{(m)} \\ &= -(\delta\xi^{(m+1)} - \delta\xi^{(m)})\, c_\xi\, (\dot{\xi}^{(m+1)} - \dot{\xi}^{(m)}) \\ &\quad - (\delta\xi^{(m+1)} - \delta\xi^{(m)})\, k_\xi\, (\xi^{(m+1)} - \xi^{(m)}). \end{aligned} \tag{2.16}$$

The expression of the mass matrix for the ground resonance problem remains unaltered. The difference lies in terms of the damping and stiffness matrix. Since the dampers are considered with negligible stiffness terms—otherwise, in the PVW formulation is still reported their stiffness work contribution, but assembling the problem matrices their contribution is considered null. The damping and stiffness matrix of the coupled portion of the ground resonance problem for the IB damping arrangement:

$$\mathbf{C}_{\text{GR, IB}} = \begin{bmatrix} \frac{N_b}{2}\, c_\xi\, \Xi_1 & \frac{N_b}{2}\, I_b\Omega\, 2 & 0 & 0 \\ -\frac{N_b}{2}\, I_b\Omega\, 2 & \frac{N_b}{2}\, c_\xi\, \Xi_1 & 0 & 0 \\ 0 & 0 & C_x & 0 \\ 0 & 0 & 0 & C_y \end{bmatrix}, \tag{2.17}$$

where the term Ξ_1, as presented in [13], is equal to $2(1-\cos\Delta\psi) \approx 1.3820$ for a five-blade rotor.

$$\mathbf{K}_{\text{GR, IB}} = \begin{bmatrix} \frac{N_b}{2}[-(I_\xi - eS_\xi)\Omega^2] & \frac{N_b}{2}\Omega c_\xi \,\Xi_1 & 0 & 0 \\ -\frac{N_b}{2}\Omega c_\xi \,\Xi_1 & \frac{N_b}{2}[-(I_\xi - eS_\xi)\Omega^2] & 0 & 0 \\ 0 & 0 & K_x & 0 \\ 0 & 0 & 0 & K_y \end{bmatrix}. \tag{2.18}$$

It can be observed that, independently from the damper characteristics, c_ξ and k_ξ, the ground resonance matrices have different elements directly depending on the architecture employed for the dampers.

2.3.3. Inter-2-Blade Ground Resonance Formulation

Employing this new innovative architecture, the damper rotation is now related to the preceding and successive blades:

$$\Delta\xi^{(m)} = \xi^{(m+2)} - \xi^{(m)} \tag{2.19}$$

The virtual work of the damper becomes:

$$\delta\mathcal{W}_{\text{damper}} = -(\delta\xi^{(m+2)} - \delta\xi^{(m)})\, c_\xi\, (\dot{\xi}^{(m+2)} - \dot{\xi}^{(m)}) - (\delta\xi^{(m+2)} - \delta\xi^{(m)})\, k_\xi\, (\xi^{(m+2)} - \xi^{(m)}), \tag{2.20}$$

thus, the expressions of the damping and stiffness matrices for the I2B damper configuration become:

$$\mathbf{C}_{\text{GR, I2B}} = \begin{bmatrix} \frac{N_b}{2}\, c_\xi\, \Xi_2 & \frac{N_b}{2}\, I_b\Omega\, 2 & 0 & 0 \\ -\frac{N_b}{2}\, I_b\Omega\, 2 & \frac{N_b}{2}\, c_\xi\, \Xi_2 & 0 & 0 \\ 0 & 0 & C_x & 0 \\ 0 & 0 & 0 & C_y \end{bmatrix} \tag{2.21}$$

where the term Ξ_2 is equal to $2(1 - \cos(2\Delta\psi)) \approx 3.6180$.

$$\mathbf{K}_{\text{GR, I2B}} = \begin{bmatrix} \frac{N_b}{2}[-(I_\xi - eS_\xi)\Omega^2] & \frac{N_b}{2}\Omega c_\xi \,\Xi_2 & 0 & 0 \\ -\frac{N_b}{2}\Omega c_\xi \,\Xi_2 & \frac{N_b}{2}[-(I_\xi - eS_\xi)\Omega^2] & 0 & 0 \\ 0 & 0 & K_x & 0 \\ 0 & 0 & 0 & K_y. \end{bmatrix} \tag{2.22}$$

An essential aspect of adopting an alternative damper configuration concerns its effect on the cyclic modes, particularly ξ_{1_c} and ξ_{1_s}, which are primarily involved in the ground resonance phenomenon. These configurations introduce an "amplification factor" that increases the damping associated with these modes.

For the Inter-Blade configuration, this amplification factor is defined as: $\Xi_1 = 2(1 - \cos(\Delta\psi))$, which, for a five-blade rotor—the configuration investigated in this thesis—with $\Delta\psi = 72$ deg results in $\Xi_1 = 1.382$. In contrast, for the I2B configuration, the factor is given by: $\Xi_2 = 2(1 - \cos(2\Delta\psi))$, which evaluates to $\Xi_2 = 3.618$ for the same rotor.

These factors are of primary importance, as they show how dampers with lower mechanical characteristics — specifically reduced values of c_ξ and k_ξ — can nevertheless achieve stability performances comparable to a conventional BTH configuration. This outcome is made possible by the additional effective damping introduced through the particular geometric arrangement of the I2B configuration.

This aspect becomes evident when applying the Deutsch criterion for evaluating the stability of the coupled rotor-fuselage system [5].

2.4. Deutsch Criteria for Different Damper Architectures

The advantages of the different damper arrangements, compared to the classical BTH configuration, become evident when analyzing the Deutsch criterion. Originally formulated for blade-to-hub damper configurations, this criterion relates the minimum damping required to prevent instability of the first cyclic multiblade modes in the ground resonance problem.

The criterion was initially formulated for the first damper arrangement developed (see [5]), but it has subsequently been extended to different damper architectures and can be found in [7].

The general formulation of the Deutsch criterion for a BTH arrangement states that no instability arises in the ground resonance problem if the following relation between the different coefficients is satisfied:

$$C_\xi^{\mathrm{BTH}} \frac{C_\clubsuit}{\omega_\clubsuit^2} > \frac{N_b}{4} \frac{1 - \nu_\xi^2}{\nu_\xi^2} S_\xi^2, \tag{2.23}$$

where $\clubsuit = (x, y)$ denotes the in-plane hub displacement, $\omega_{\clubsuit} = \sqrt{K_{\clubsuit}/M_{\clubsuit}}$, and $\nu_{\xi} = \sqrt{\frac{eS_{\xi}}{I_{\xi}}}$. For the IB configuration, the Deutsch criterion can be rewritten as:

$$C_{\xi}^{\mathrm{IB}} \frac{C_{\clubsuit}}{\omega_{\clubsuit}^2} > \frac{N_b}{4\,\Xi_1} \frac{1-\nu_{\xi}^2}{\nu_{\xi}^2} S_{\xi}^2, \tag{2.24}$$

where Ξ_1 is the amplification factor associated with the IB damper arrangement, as introduced in Eq. (2.17).

Similarly, for the I2B configuration, the stability condition becomes:

$$C_{\xi}^{\mathrm{I2B}} \frac{C_{\clubsuit}}{\omega_{\clubsuit}^2} > \frac{N_b}{4\,\Xi_2} \frac{1-\nu_{\xi}^2}{\nu_{\xi}^2} S_{\xi}^2, \tag{2.25}$$

where Ξ_2 is was defined in Eq. (2.22).

Thus, the stability condition required by the extended Deutsch criterion for both the IB and I2B arrangements can be rewritten in terms of the standard damping requirement of the classical BTH configuration.

$$C_{\xi}^{\mathrm{IB}} = \frac{1}{2(1-\cos(\Delta\psi))} C_{\xi}^{\mathrm{BTH}}, \tag{2.26}$$

$$C_{\xi}^{\mathrm{I2B}} = \frac{1}{2(1-\cos(2\Delta\psi))} C_{\xi}^{\mathrm{BTH}}. \tag{2.27}$$

Observing that, for a helicopter equipped with five blades — as considered in this work — the non-standard damping arrangements require a lower amount of damping to achieve the same stability margin when compared to the classical BTH configuration.

2.5. Ground Resonance Equations for Damper Failure

The analysis of damper failure scenarios highlights the importance of evaluating the residual stability margin when a damper becomes inoperative. This concept was first introduced by Peters and Hohenemser in [15], the failure problem is of fundamental importance since is a mandatory regulatory requirement in both CS 27 and CS 29.

Consequently, the rotor must not only be free from dangerous ground resonance oscilla-

tions within the typical operating speed range in the nominal condition but also in the case of a single damper failure.

In the event of damper failure, the rotor can no longer be considered isotropic. Due to this asymmetry, the periodic nature of the problem can no longer be neglected, and thus the system of equations developed in Eq. (2.9) is no longer valid.

To address the system behavior in the presence of one or more failed dampers, a different approach has to be employed. As described in [15], the analysis relies on the computation of the Floquet Transition Matrix to the ground resonance problem. In this method, the Floquet Transition Matrix relates the state variables from the beginning to the end of one period, capturing the periodic coefficients introduced by the asymmetry.

This approach is applicable to all linearized rotorcraft stability problems involving lifting rotors, including failure scenarios of one or more lead-lag dampers.

2.5.1. Floquet Transition Matrix

The solution of the LTP system, as reported in [15], revolves around the formulation of the Floquet Transition Matrix $\mathbf{Q}$.

The GR system, with damper failure or not, can be written reducing to state formulation to a first order system, which in general may be written as:

$$\dot{\mathbf{x}} + \mathbf{D}(t)\mathbf{x} = \mathbf{G}(t) \tag{2.28}$$

where the vector $\mathbf{x}$ contains the state variables of the problem, the MBC coordinates and their derivative and the airframe in-plane displacement and velocities, the matrices $\mathbf{D}(t)$ and $\mathbf{G}(t)$ are periodic with period $T = \frac{2\pi}{\Omega}$. Exploiting the periodicity of the problem, the Floquet Transition Matrix $\mathbf{Q}$ of the system is defined by

$$\mathbf{x}(t) = \mathbf{Q}\mathbf{x}(0) \tag{2.29}$$

where $\mathbf{x}(0)$ is a general set of initial conditions for Eq. (2.28). Floquet's Theorem states that for an Nth order system of ordinary differential equation, such as Eq. (2.28) having coefficients periodic with T has transients solution of the form:

$$\mathbf{x} = \mathbf{A}(t)\boldsymbol{\alpha}_k^{\eta_k t} \tag{2.30}$$

where $\mathbf{A}(t)$ si periodic with T, η_k are complex characteristic numbers and the $\boldsymbol{\alpha}_k$ are

constants derived from initial conditions

$$\alpha_K = \mathbf{A}(0)^{-1}\,\mathbf{x}(0) \tag{2.31}$$

The stability of the system can be completely determined form the values of η_K, Eq. (2.30) can be written for $t = T$, and $t = 0$, exploiting the propriety of the matrix $\mathbf{A}$ respectively $\mathbf{A}(0) = \mathbf{A}(T)$, and expressing $\Lambda_k = \exp(\eta_k T)$:

$$\begin{aligned} \mathbf{x}(T) &= \mathbf{A}(0)\Lambda_k\boldsymbol{\alpha}_k \\ \mathbf{x}(0) &= \mathbf{A}(0)\boldsymbol{\alpha}_k \end{aligned} \tag{2.32}$$

Substituting Eq. (2.32) in Eq. (2.28) and rearranging yields:

$$\mathbf{Q}\mathbf{A}(0)\boldsymbol{\alpha}_k - \mathbf{A}(0)\Lambda_k\boldsymbol{\alpha}_k = \mathbf{0} \tag{2.33}$$

Let the i-th column of $\mathbf{A}(0)$ be denoted as $\{\mathbf{a}_0\}_i$. Substituting into Eq. (2.33) yields:

$$\sum_{i=1}^{N} \left(\mathbf{Q} - \Lambda_i\mathbf{I}\right)\{\mathbf{a}_0\}_i\alpha_i \tag{2.34}$$

Note that since $\mathbf{x}(0)_i$ is arbitrary, the coefficients a_i are also arbitrary. Accordingly, each term in the summation of Eq. (2.34) must independently vanish. From Eq. (2.31), we know that $\mathbf{A}(0)$ is invertible, so none of the columns $\{\mathbf{a}_0\}_i$ can be zero. Therefore, we obtain:

$$|\mathbf{Q} - \Lambda_i\mathbf{I}| = 0 \qquad i = 1, \ldots, N \tag{2.35}$$

According to Eq. (2.35), the values Λ_i are the eigenvalues of $\mathbf{Q}$, which are generally complex numbers. We now define the characteristic complex numbers η_k as:

$$\eta_k = \lambda_k + \mathrm{j}\omega_k \tag{2.36}$$

Substituting into Eq. (2.30), we obtain:

$$\mathbf{x}(t) = \mathbf{A}(T)\boldsymbol{\alpha}_k e^{\lambda_k t}\left(\cos\omega_k t + \mathrm{j}\sin\omega_k t\right) \tag{2.37}$$

The stability of the system is determined by the real part λ_k. The eigenvalues of the system are obtained by recalling that $\eta_k = \frac{1}{T}\ln\Lambda_k$, so:

$$\lambda_k = \frac{1}{T}\ln\left[(\mathrm{Re}\Lambda_k)^2 + (\mathrm{Im}\Lambda_k)^2\right] \tag{2.38}$$

The corresponding frequency is evaluated as:

$$\omega_k = \frac{1}{T}\arctan\left(\frac{\mathrm{Im}\Lambda_k}{\mathrm{Re}\Lambda_k}\right) \tag{2.39}$$

Since the arctangent function is multi-valued, each frequency can only be determined as a fundamental frequency $\pm\frac{n2\pi}{T}$, with $n \in \mathbb{N}$. These integer multiples represent the coefficients of the exponential terms $e^{\eta_k t}$ with period T, and can therefore be incorporated into the periodic matrix $\mathbf{A}(t)$ in Eq. (2.30).

Although the governing equations remain unchanged from the all-dampers-operative (ADO) configuration, particular care must be taken in assembling the matrices used in Eq. (2.9).

As a result of the damper failure, the matrices $\mathbf{C}_{\mathrm{GR}}$ and $\mathbf{K}_{\mathrm{GR}}$ are no longer constant with respect to the azimuthal position, since the loss of isotropy reintroduces this dependence. Therefore, the entire ground resonance equations—must be integrated at each time step.

The two systems employed for the solution of the GR problem in case of damper failure differs on the computation of the monodromy matrix that governs the stability of the LTP system.

The first method relies on numerical integration using a fourth-order Runge-Kutta scheme. For each angular velocity Ω within the swept range of the ground resonance analysis, the system is discretized into N azimuth steps per revolution. The monodromy matrix $\mathbf{Q}$ is then computed as:

$$\begin{aligned}
\mathbf{K}_1^{(k)} &= \mathbf{A}^{(j)}\mathbf{Q}^{(k)} \\
\mathbf{K}_2^{(k)} &= \mathbf{A}^{(j+1)}\left(\mathbf{Q}^{(k)} + \frac{h}{2}\mathbf{K}_1^{(k)}\right) \\
\mathbf{K}_3^{(k)} &= \mathbf{A}^{(j+1)}\left(\mathbf{Q}^{(k)} + \frac{h}{2}\mathbf{K}_2^{(k)}\right) \\
\mathbf{K}_4^{(k)} &= \mathbf{A}^{(j+2)}\left(\mathbf{Q}^{(k)} + h\mathbf{K}_3^{(k)}\right) \\
\mathbf{Q}^{(k+1)} &= \mathbf{Q}^{(k)} + \frac{h}{6}\left(\mathbf{K}_1^{(k)} + 2\mathbf{K}_2^{(k)} + 2\mathbf{K}_3^{(k)} + \mathbf{K}_4^{(k)}\right)
\end{aligned}$$

where $\mathbf{A}$ is the periodic system matrix and h the time step for Runge-Kutta equal to $\frac{2}{N}\frac{2\pi}{\Omega}$.

Computed the monodromy matrix for the given angular velocity, the eigenvalues where computed as showed in Eq. (2.35)

In contrast, the computation of the monodromy matrix using the Hsu method differs from the Runge-Kutta approach. In this case, the number of azimuth steps j at which the periodic system matrix $\mathbf{A}$ is evaluated is doubled with respect to the previous method. The monodromy matrix is then progressively updated at each step by applying the matrix exponential:

$$\hat{\mathbf{A}} = \left(\mathbf{A}^{(j)} + \mathbf{A}^{(j+1)}\right)/2 \tag{2.40}$$

$$\mathbf{Q}^{(k+1)} = \mathrm{e}^{\left(\hat{\mathbf{A}}\,\Delta t\right)}\mathbf{Q}^{(k)} \tag{2.41}$$

where Δt is now equal$\frac{1}{N}\frac{2\pi}{\Omega}$, half respect the previous problem.

Nonetheless, regardless of the method used, the same eigenvalues were obtained for all damper failure problems. The Hsu exponential method was implemented to assess the sensitivity of the monodromy matrix with respect to the geometrical parameters, as will be shown later in Chapter 2.

In Fig. 2.3 the results obtained for the ODI problem are reported for the three damper configurations, derived from the two methods employed for the construction of the monodromy matrix, it can be observed that independently from the method employed the results are coincident.

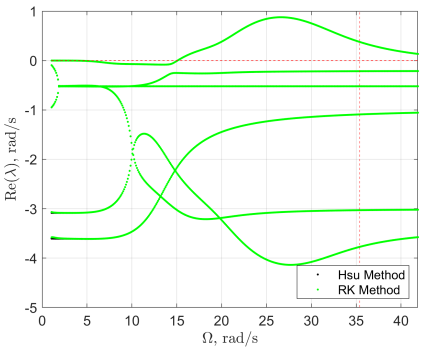

(a) BTH ground resonance in case of damper failure

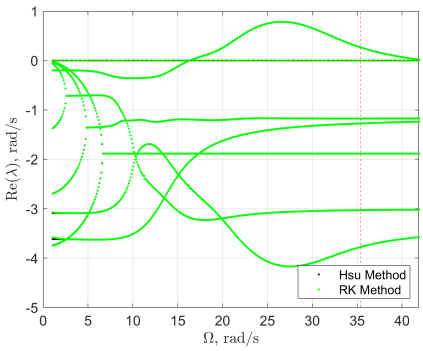

(b) IB ground resonance in case of damper failure

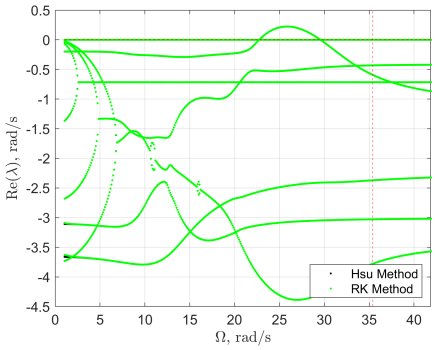

(c) I2B ground resonance in case of damper failure

Figure 2.3: Ground resonance problem in case of a damper failure, Hsu vs R-K, for differente dampers arrangements

3 | Eigensolution Sensitivity to a Generic Parameter

In this chapter, the mathematical formulation of the general sensitivity analysis problem is first formally introduced. The methodology is then applied to a generic rotor equipped with an I2B damper configuration, in the context of ground resonance analysis. This procedure will serve as the foundation not only for this chapter but also for the following ones. By employing the continuation approach—presented in [14]—it becomes possible to investigate the system's stability and track the evolution of eigenvalues. This study is not limited to analyzing the variation of eigenvalues with respect to geometrical parameters, as done for the Hammond I2B case in this chapter, but also extends to tuning the damper characteristics in order to obtain dynamically equivalent rotor models in terms of damping on main blade modes.

The generic ground resonance problem, independently from the damper configuration can be written as a second order differential problem

$$\mathbf{M}\ddot{\mathbf{q}} + \mathbf{C}\dot{\mathbf{q}} + \mathbf{K}\mathbf{q} = \mathbf{0} \tag{3.1}$$

the vector $\mathbf{q}$ collects the MBC of the rotor and also the airframe displacement in hub plane $(N_b + 2)$ unknowns, its eigensolution can be obtained by recasting the problem into linear state space form:

$$\begin{Bmatrix} \dot{\mathbf{q}} \\ \ddot{\mathbf{q}} \end{Bmatrix} = \begin{bmatrix} \mathbf{0} & \mathbf{I} \\ -\mathbf{M}^{-1}\mathbf{K} & -\mathbf{M}^{-1}\mathbf{C} \end{bmatrix} \begin{Bmatrix} \mathbf{q} \\ \dot{\mathbf{q}} \end{Bmatrix} \tag{3.2}$$

or

$$\dot{\mathbf{x}} = \mathbf{A}\mathbf{x} \tag{3.3}$$

The eigensolution is found solving the problem

$$(s\mathbf{I} - \mathbf{A})\ \mathbf{x} = \mathbf{0} \tag{3.4}$$

Once the eigensolution is found, the sensitivity of the eigenvalue indicated s and the corresponding eigenvector $\mathbf{x}$ can be obtained by computing their partial derivatives with respect to a generic parameter p. To solve the problem, a normalization equation for the eigenvector must first be added

$$\mathbf{x}^H\mathbf{x} = 1 \tag{3.5}$$

Formally the derivative respect p of Eq. (3.5) is

$$\mathbf{x}_{/p}^H\mathbf{x} + \mathbf{x}^H\mathbf{x}_{/p} = 0 \quad \text{(which implies } \mathbf{x}^H\mathbf{x}_{/p} = 0\text{)}. \tag{3.6}$$

More information regards the normalization condition can be found in [14], § 4.3.

Thus, the system to be solved becomes:

$$s_{/p}\,\mathbf{x} - \mathbf{A}_{/p}\,\mathbf{x} + (s\mathbf{I} - \mathbf{A})\,\mathbf{x}_{/p} = \mathbf{0}, \tag{3.7a}$$

$$\mathbf{x}^H\mathbf{x}_{/p} = 0. \tag{3.7b}$$

The linear problem can be written as:

$$\begin{bmatrix} (s\mathbf{I} - \mathbf{A}) & \mathbf{x} \\ \mathbf{x}^H & 0 \end{bmatrix} \begin{Bmatrix} \mathbf{x}_{/p} \\ s_{/p} \end{Bmatrix} = \begin{Bmatrix} \mathbf{A}_{/p}\,\mathbf{x} \\ 0 \end{Bmatrix} \tag{3.8}$$

The matrix on the left-hand side is the Jacobian matrix of the system and remains the same regardless of the specific parameter p. In contrast, the parameter p only affects the right-hand side of the equation. As a result, the same matrix can be used to evaluate the sensitivity of the system with respect to all parameters; only the right-hand side changes depending on the chosen parameter.

3.1. Problem Definition

The rotor configuration considered for the sensitivity analysis applied to the ground resonance problem is a five-blade rotor equipped with an I2B damper configuration. The geometrical parameters of the rotor are taken from the previous thesis [1].

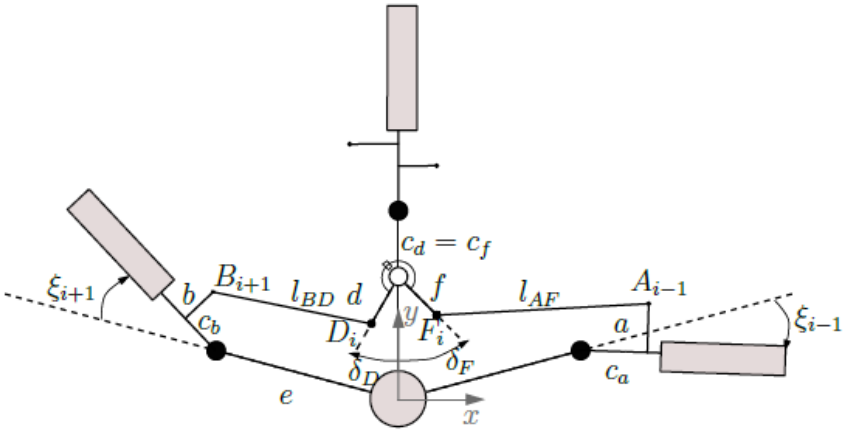

Figure 3.1: Kinematic model for I2B rotor, source in [1].

Through a series of kinematic relationship, that are discussed in more detail in Appendix A, regarding the right side of the damper, a link between the angle γ_F, and the lag angle ξ_{i-1} can found, the connection of the point A_{i-1} and F_i is given by the rigid rod l_{AF}. In an analogous way, for the left side of the damper, kinematic relationships can be developed in order to link the damper angle γ_D to the lag angle ξ_{i+1}, the connection between B_{i+1} and D_i is considered rigid and is given by the rod l_{BD}.

The other relevant rotor characteristics required to solve the ground resonance problem are those described by Hammond in [9] and are reported in Table 3.1.

Table 3.1: Hammond Model's Data, source in [9].

Parameter	**Value**	**Units**
Number of blades, N_b	5	–
Blade mass, m_b	94.9	kg
Blade mass static moment, S_ξ	289.1	kg m
Blade mass moment of inertia, I_ξ	1084.7	kg m^2
Lag hinge offset, e	0.3048	m
Lag spring, K_ξ	0	N m rad^{-1}
Lag damper, C_ξ	4067.5	N m s rad^{-1}
Hub mass, m_x	8026.6	kg
Hub mass, m_y	3283.6	kg
Hub spring, K_x, K_y	124081.8	N m^{-1}
Hub damper, C_x	51078.7	N s m^{-1}
Hub damper, C_y	25539.35	N s m^{-1}

It is note to observed that in the work of Hammond the lag spring has null value, $K_\xi = 0$. So the sensitivity of the eigenvalues respect the stiffness term will be written and computed, but for the Hammond problem will play no role.

The main geometrical parameters of the system, whose influence on the eigenvalue sensitivity will be investigated, are listed in Table 3.2. These parameters were obtained in the previous thesis [1] and allow for a certain degree of variability in the possible configurations of the I2B geometry.

Table 3.2: List of geometrical parameters for the I2B configuration.

Parameter	**Description**	**Units**
c_a, c_b	Radial attachment positions on the rear and front blades	m
a, b	Chordwise attachment positions of the damper on rear and front blades	m
d, f	Lengths of the left and right intermediate damper arms	m
c_d	Hinge positions along the middle blade	m

The values of the geometrical parameters, normalized for the lag-hinge offset are reported in Table 3.3.

Table 3.3: Normalized geometrical parameters for the I2B configuration.

Parameter	**Value**
a/e	0.5
b/e	0.5
c_a/e	0.25
c_b/e	0.25
d/e	0.5
f/e	0.5
c_d/e	0.25

Solving the GR problem for this rotor model, implementing the I2B damper's architecture leads to the following results:

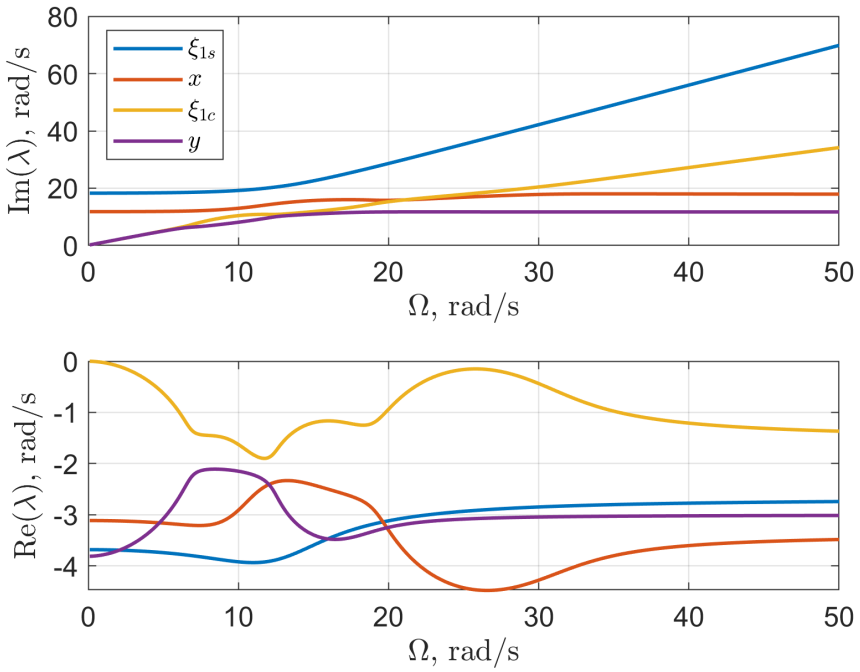

Figure 3.2: GR results for I2B rotor with Hammond data.

Figure 3.2 reports the imaginary and real part of the eigenvalues for the GR problem, solving the system of Eq. (2.9). It can be observed how the real part of the cyclic eigenvalue get closer to zero at high RPM, this is due to the coupling with the airframe, and may lead to an instability if the damping of the mode doesn't satisfy the Deutsch criteria.

The condition reported in Fig. 3.2 will be considered as the baseline solution for the sensitivity analysis, perturbations of the parameters values will be imposed starting from this configuration.

3.2. Development of Sensitivity Problem

Once the baseline solution for the ground resonance problem has been obtained, (Fig. 3.2), the sensitivity of its eigenvalues with respect to the geometrical parameters of the system was developed as follows:

Taking the chordwise attachment positions of the blade to the damper (rear/front blade) as an example, though the procedure will be repeated for all parameters listed in Table 3.2, a and b of the arms A_i and B_{i+2}, the perturbation of the parameter was defined as follows:

$$a = c_0 + \Delta, \quad b = c_0 + \Delta. \tag{3.9}$$

Where c_o stands for the reference value.

Starting from the kinematic relationships that describe the I2B kinematic model, explained in detail in Appendix A as outlined in § 3.1, the damping and stiffness of the dampers are linked directly to the kinematic model from two parameters, $\Psi_{\xi_{i-1}\gamma_F}$ and $\Psi_{\xi_{i+1}\gamma_D}$, that links respectively the angle γ_F of the damper to the lag angle ξ_{i-1}, and the angle γ_D to the lag angle ξ_{i+1}.

Considering the geometry selected for the I2B kinematics, the lengths of the two rods connecting the blades are not independent parameters. In fact, the lengths of the arms l_{BD} and l_{AF} depend on:

$$\mathbf{l}_{AF} = f(\xi_{i-1}, \gamma_F, N_b, a, c_a, f, c_f), \tag{3.10}$$

$$\mathbf{l}_{BD} = f(\xi_{i+1}, \gamma_D, N_b, b, c_b, d, c_d), \tag{3.11}$$

additionally assuming small displacements and linearizing, yields:

$$\begin{aligned} l_{AF} = \sqrt{\mathbf{l}_{AF}^{\top} \cdot \mathbf{l}_{AF}} \approx L_0 + \frac{\partial l_{AF}}{\partial \xi_{i-1}}\Big|_E \Delta\xi_{i-1} + \frac{\partial l_{AF}}{\partial \gamma_F}\Big|_E \Delta\gamma_F + \frac{\partial l_{AF}}{\partial a}\Big|_E \Delta a \\ + \frac{\partial l_{AF}}{\partial c_a}\Big|_E \Delta c_a + \frac{\partial l_{AF}}{\partial f}\Big|_E \Delta f + \frac{\partial l_{AF}}{\partial c_f}\Big|_E \Delta c_f. \end{aligned} \tag{3.12}$$

In a similar manner, the same expression can be developed for the arm l_{BD}.

The rods are considered sufficiently stiff, so initially the contributions of the lead-lag angle and the orientation of the damper arm must be of the same magnitude but opposite in sign to maintain a constant length of the rigid rods. By treating the other derivatives as second-order terms, an initial relationship can be obtained between the cylindrical damper angles, γ_F or γ_D, and the corresponding lead-lag angles, ξ_{i-1} or ξ_{i+1}.

$$\frac{\partial l_{AF}}{\partial \xi_{i-1}}\Big|_E \Delta\xi_{i-1} = -\frac{\partial l_{AF}}{\partial \gamma_F}\Big|_E \Delta\gamma_F \tag{3.13}$$

$$\frac{\partial l_{BD}}{\partial \xi_{i+1}}\Big|_E \Delta\xi_{i+1} = -\frac{\partial l_{BD}}{\partial \gamma_D}\Big|_E \Delta\gamma_D \tag{3.14}$$

This expression represent the parameters $\Psi_{\xi_{i-1}\gamma_F}$ and $\Psi_{\xi_{i+1}\gamma_D}$

$$\Psi_{\xi_{i-1}\gamma_F} = -\frac{\left.\dfrac{\partial l_{AF}}{\partial \xi_{i-1}}\right|_E}{\left.\dfrac{\partial l_{AF}}{\partial \gamma_F}\right|_E} \tag{3.15}$$

$$\Delta\gamma_F = \Psi_{\xi\gamma_F}\Delta\xi_{i-1} \tag{3.16}$$

Once the relationship between the damper angle and the lag angles—expressed through the dimensionless parameter in Eq. 3.15—is established, the sensitivity of this coefficient with respect to the system's geometrical parameters can be evaluated.

With this sensitivity determined, it is then possible to assemble the mass, damping, and stiffness matrices of the system. Subsequently, the sensitivity of the system's eigenvalues to each parameter is computed, leveraging the linearity of the model and the principle of superposition. This enables the analysis of how variations in individual parameters—while holding the others constant—affect the eigenvalues relevant to ground resonance stability.

Since the model is based on Hammond's rotor configuration, the stiffness contributions associated with the damper are null. Therefore, only the sensitivity of the damping-related terms is developed. Nevertheless, the full expression, including the stiffness terms, is presented for the sake of completeness.

3.2.1. Sensitivity of Stiffness and Damping Terms

The dimensionless ratios $\Psi_{\xi_{i-1}\gamma_F}$ and $\Psi_{\xi_{i+1}\gamma_D}$, that links the lag angles to the damper's angles are retrieved as follows:

For the arm AF, right side of Fig. 3.1:

$$\begin{aligned}
\mathbf{l}_{AF} &= \mathbf{F} - \mathbf{A} && \text{(vector between the ends of the arms)} \\
l_{AF} &= \|\mathbf{l}_{AF}\| = \sqrt{\mathbf{l}_{AF}^{\top}\cdot\mathbf{l}_{AF}} && \text{(vector norm)} \\
\Psi_{\xi_{i-1}\gamma_F} &= -\frac{\frac{\partial\|F-A\|}{\partial\xi_{i-1}}}{\frac{\partial\|F-A\|}{\partial\gamma_F}} && \text{(dimensionless parameter)}
\end{aligned} \tag{3.17}$$

For the arm BD, left side of Fig. 3.1:

$$\begin{aligned}
\mathbf{l}_{BD} &= \mathbf{D} - \mathbf{B} && \text{(vector between the ends of the arms)} \\
l_{BD} &= \|\mathbf{l}_{BD}\| = \sqrt{\mathbf{l}_{BD}^{\top}\cdot\mathbf{l}_{BD}} && \text{(vector norm)} \\
\Psi_{\xi_{i+1}\gamma_D} &= -\frac{\frac{\partial\|D-B\|}{\partial\xi_{i+1}}}{\frac{\partial\|D-B\|}{\partial\gamma_D}}. && \text{(dimensionless parameter)}
\end{aligned} \tag{3.18}$$

Starting from the formulation of the PVW considering the single damper, the virtual work

of the damper for the I2B arrangements with both damping and stiffness terms takes the form

$$\delta\mathcal{W}_{\text{damper}} = -\delta\Delta\xi K_\xi \Delta\xi - \delta\Delta\xi C_\xi \Delta\dot{\xi} \tag{3.19}$$

where the relative motion of the damper's parts is the difference between the rotation of the blades, so for the I2B damper arrangements,

$$\Delta\xi = \xi^{(m+2)} - \xi^{(m)} \tag{3.20}$$

So the virtual work expression of Eq. (3.19) can be rewritten as:

$$\delta\mathcal{W}_{\text{damper}} = -(\delta\xi^{(m+2)} - \delta\xi^{(m)})K_\xi(\xi^{(m+2)} - \xi^{(m)}) - (\delta\xi^{(m+2)} - \delta\xi^{(m)})C_\xi(\dot{\xi}^{(m+2)} - \dot{\xi}^{(m)}) \tag{3.21}$$

for $m = 1 \rightarrow N_b$ (where $m = N_b{+}1$, is interpreted as $m = 1$). Considering the contribution of all dampers, the equivalent moment acting on blade m is:

$$C^{(m)} = -K_\xi\left(2\xi^{(m)} - \xi^{(m+2)} - \xi^{(m-2)}\right) - C_\xi\left(2\dot{\xi}^{(m)} - \dot{\xi}^{(m+2)} - \dot{\xi}^{(m-2)}\right) \tag{3.22}$$

Indeed, once the dimensionless groups are defined, starting from Eq. 3.22 it becomes possible to obtain the damping matrix for the single blade, written in the rotating reference frame.

$$\begin{aligned}\delta\mathcal{W}_i = -\delta\begin{Bmatrix}\xi^{(m)}\\ \xi^{(m+2)}\end{Bmatrix}^T \Bigg(& K_\xi\begin{bmatrix}\Psi^2_{\xi\gamma_F} & -\Psi_{\xi\gamma_F}\Psi_{\xi\gamma_D}\\ -\Psi_{\xi\gamma_F}\Psi_{\xi\gamma_D} & \Psi^2_{\xi\gamma_D}\end{bmatrix}\begin{Bmatrix}\xi^{(m)}\\ \xi^{(m+2)}\end{Bmatrix}\\ & + C_\xi\begin{bmatrix}\Psi^2_{\xi\gamma_F} & -\Psi_{\xi\gamma_F}\Psi_{\xi\gamma_D}\\ -\Psi_{\xi\gamma_F}\Psi_{\xi\gamma_D} & \Psi^2_{\xi\gamma_D}\end{bmatrix}\begin{Bmatrix}\dot{\xi}^{(m)}\\ \dot{\xi}^{(m+2)}\end{Bmatrix}\Bigg)\end{aligned} \tag{3.23}$$

Assembling each damper contributes, and so each local damping and stiffness term, the global stiffness and damping matrices are assembled; those matrices will result in a tri-diagonal matrix, where the terms on the main diagonal will be:

$$\begin{aligned}K_{\xi_{\text{diag}}} &= K_\xi(\Psi^2_{\xi\gamma_F} + \Psi^2_{\xi\gamma_D})\\ C_{\xi_{\text{diag}}} &= C_\xi(\Psi^2_{\xi\gamma_F} + \Psi^2_{\xi\gamma_D})\end{aligned} \tag{3.24}$$

while the extra-diagonal terms:

$$K_{\xi_{\text{extra-diag}}} = K_{\xi}(-\Psi_{\xi\gamma_F}\Psi_{\xi\gamma_D}) \tag{3.25}$$
$$C_{\xi_{\text{extra-diag}}} = C_{\xi}(-\Psi_{\xi\gamma_F}\Psi_{\xi\gamma_D})$$

Once the direct relationship between the kinematic and lag angles has been obtained, the sensitivity of these terms with respect to the generic parameter p can be developed:

$$\frac{\partial \Psi_{\xi_{i-1}\gamma_F}}{\partial p} = \frac{\partial}{\partial p}\left(-\frac{\frac{\partial \|F-A\|}{\partial \xi_{i-1}}}{\frac{\partial \|F-A\|}{\partial \gamma_F}}\right). \tag{3.26}$$

$$\frac{\partial \Psi_{\xi_{i-1}\gamma_F}}{\partial p} = -\frac{\frac{\partial}{\partial p}\left(\frac{\partial \|F-A\|}{\partial \xi_{i-1}}\right)\cdot\frac{\partial \|F-A\|}{\partial \gamma_F} - \frac{\partial}{\partial p}\left(\frac{\partial \|F-A\|}{\partial \gamma_F}\right)\cdot\frac{\partial \|F-A\|}{\partial \xi_{i-1}}}{\left(\frac{\partial \|F-A\|}{\partial \gamma_F}\right)^2}. \tag{3.27}$$

An analogous expression holds for $\Psi_{\xi_{i+1}\gamma_D}$

$$\frac{\partial \Psi_{\xi_{i+1}\gamma_D}}{\partial p} = -\frac{\frac{\partial}{\partial p}\left(\frac{\partial \|D-B\|}{\partial \xi_{i+1}}\right)\cdot\frac{\partial \|D-B\|}{\partial \gamma_D} - \frac{\partial}{\partial p}\left(\frac{\partial \|D-B\|}{\partial \gamma_D}\right)\cdot\frac{\partial \|D-B\|}{\partial \xi_{i+1}}}{\left(\frac{\partial \|D-B\|}{\partial \gamma_D}\right)^2}. \tag{3.28}$$

Once the derivative of the non-dimensional terms is obtained, the derivative of the damping and stiffness matrix with respect to the parameter p can be computed. The global derivative of the damping matrix for the entire system ($N_{\text{blade}} \times N_{\text{blade}}$) can be assembled from the local damping blade matrices, denoted as $\mathbf{C}_{\xi}$ and $\mathbf{K}_{\xi}$.

The local derivative of the damping and stiffness matrix, in rotating coordinates, is shown in Eq. (3.23), derived with respect to parameter p as

$$\mathbf{K}_{\xi/p} = K_{\xi}\begin{bmatrix} 2\Psi_{\xi\gamma_F}\dfrac{\partial \Psi_{\xi\gamma_F}}{\partial p} & -\left(\dfrac{\partial \Psi_{\xi\gamma_F}}{\partial p}\Psi_{\xi\gamma_D} + \Psi_{\xi\gamma_F}\dfrac{\partial \Psi_{\xi\gamma_D}}{\partial p}\right) \\ -\left(\dfrac{\partial \Psi_{\xi\gamma_F}}{\partial p}\Psi_{\xi\gamma_D} + \Psi_{\xi\gamma_F}\dfrac{\partial \Psi_{\xi\gamma_D}}{\partial p}\right) & 2\Psi_{\xi\gamma_D}\dfrac{\partial \Psi_{\xi\gamma_D}}{\partial p} \end{bmatrix} \tag{3.29}$$

$$\mathbf{C}_{\xi/p} = C_{\xi}\begin{bmatrix} 2\Psi_{\xi\gamma_F}\dfrac{\partial \Psi_{\xi\gamma_F}}{\partial p} & -\left(\dfrac{\partial \Psi_{\xi\gamma_F}}{\partial p}\Psi_{\xi\gamma_D} + \Psi_{\xi\gamma_F}\dfrac{\partial \Psi_{\xi\gamma_D}}{\partial p}\right) \\ -\left(\dfrac{\partial \Psi_{\xi\gamma_F}}{\partial p}\Psi_{\xi\gamma_D} + \Psi_{\xi\gamma_F}\dfrac{\partial \Psi_{\xi\gamma_D}}{\partial p}\right) & 2\Psi_{\xi\gamma_D}\dfrac{\partial \Psi_{\xi\gamma_D}}{\partial p} \end{bmatrix} \tag{3.30}$$

Then the derivatives of the global stiffness and damping matrix for the rotor system, in rotating coordinates, are assembled similarly as already shown for the damping and stiffness matrices in Eqs. (3.24) and (3.25).

3.3. Expression of Ground Resonance Equations with Sensitivity

Once the sensitivity of the stiffness and damping terms with respect to the geometrical parameters has been computed, it is possible to assemble the full GR system. The resulting global system matrices are block-diagonal, with distinct contributions: one block corresponds to the blade dynamics, another to the airframe, and a third represents the cross-coupling between the blade and airframe equations.

Based on this structure, the coupled blade–airframe system can be expressed as a homogeneous second-order differential equation, where the sensitivity information previously derived directly feeds into the definition of the global stiffness and damping matrices. This formulation enables a comprehensive stability analysis of the blade-airframe system and provides a foundation for investigating how variations in geometric parameters affect the system's eigensolutions.

$$\mathbf{M}\ddot{\mathbf{q}} + \mathbf{C}\dot{\mathbf{q}} + \mathbf{K}\mathbf{q} = \mathbf{0} \tag{3.31}$$

where the single matrices of the system are defined as follows:

$$\mathbf{M} = \begin{bmatrix} \mathbf{M}_b & \mathbf{T}^T\mathbf{S}_b \\ \mathbf{S}_b^T\mathbf{T} & \mathbf{M}_a \end{bmatrix}, \tag{3.32}$$

$$\mathbf{C} = \begin{bmatrix} \mathbf{C}_b & \mathbf{0}_{N_b\times 2} \\ \mathbf{0}_{2\times N_b} & \mathbf{C}_a \end{bmatrix}, \tag{3.33}$$

$$\mathbf{K} = \begin{bmatrix} \mathbf{K}_b & \mathbf{0}_{N_b\times 2} \\ \mathbf{0}_{2\times N_b} & \mathbf{K}_a \end{bmatrix}. \tag{3.34}$$

the matrices with the subscript **b** represent diagonal matrices for $\mathbf{M}_b$ and block-diagonal matrices for $\mathbf{C}_b$ and $\mathbf{K}_b$ written in multiblade coordinates.

The reduced system relevant for GR is the portion of interest limited to the first cyclic mode, which couples with the airframe, extracting these matrices and starting from the equations for studying the sensitivity of eigenvalues to the generic parameter p, the fol-

lowing system can be developed:

$$\begin{cases} (\lambda^2 \mathbf{M}_{\mathrm{GR}} + \lambda \mathbf{C}_{\mathrm{GR}} + \mathbf{K}_{\mathrm{GR}})\mathbf{q} = \mathbf{0} \\ \mathbf{q}^H \mathbf{q} = 1 \end{cases} \tag{3.35}$$

The first set of equations represents the generic eigenvalue definition for coupled the GR system, while the last equation represents the normalization condition for the corresponding eigenvector.

To study the sensitivity of the eigensolution, it is necessary to develop the system by differentiating the eigenvalue λ and the corresponding eigenvector $\mathbf{q}$ with respect to the generic parameter p, so:

$$\begin{bmatrix} (\lambda^2 \mathbf{M}_{\mathrm{GR}} + \lambda \mathbf{C}_{\mathrm{GR}} + \mathbf{K}_{\mathrm{GR}}) & (2\lambda \mathbf{M}_{\mathrm{GR}} + \mathbf{C}_{\mathrm{GR}})\mathbf{q} \\ \mathbf{q}^H & 0 \end{bmatrix} \begin{Bmatrix} \mathbf{q}_{/p} \\ \lambda_{/p} \end{Bmatrix} = \begin{Bmatrix} -(\lambda^2 \mathbf{M}_{\mathrm{GR}/p} + \lambda \mathbf{C}_{\mathrm{GR}/p} + \mathbf{K}_{\mathrm{GR}/p})\,\mathbf{q} \\ 0 \end{Bmatrix} \tag{3.36}$$

This is the general formulation that will be used to study the sensitivity of all eigenvalues and eigenvectors to the generic parameter p. For each parameter, it will be necessary to evaluate the derivative of the mass, damping, and stiffness matrices, as shown in Section 3.2.1. However, the structure of the matrix of the left side of the problem remains unchanged.

By solving the system, the sensitivity of the eigenvalue and eigenvector to the generic parameter p is obtained. This parameter will be one of those influencing the length of the damper arms, as defined in Eq. (3.10) and Eq. (3.11).

3.3.1. System's Eigenvalues Calculation

To calculate the eigenvalues and eigenvectors of the system, for which the sensitivity to the generic parameter p has been studied in Eqs. (3.3), the following approach was adopted:

To ensure the correct tracking of the same eigenvalue evolution and avoid jumps in the plots, the sensitivity of the eigenvalue to the angular velocity Ω was studied.

Therefore, for each angular velocity, was the developed the eigenvalue sensitivity with respect to the angular velocity:

$$\begin{bmatrix} (\lambda^2\mathbf{M}_{\mathrm{GR}} + \lambda\mathbf{C}_{\mathrm{GR}} + \mathbf{K}_{\mathrm{GR}}) & (2\lambda\mathbf{M}_{\mathrm{GR}} + \mathbf{C}_{\mathrm{GR}})\mathbf{q} \\ \mathbf{q}^H & 0 \end{bmatrix} \begin{Bmatrix} \mathbf{q}_{/\Omega} \\ \lambda_{/\Omega} \end{Bmatrix} = \begin{pmatrix} -(\lambda^2\mathbf{M}_{\mathrm{GR}/\Omega} + \lambda\mathbf{C}_{\mathrm{GR}/\Omega} + \mathbf{K}_{\mathrm{GR}/\Omega})\,\mathbf{q} \\ 0 \end{pmatrix} \tag{3.37}$$

Formally, the left matrix of the problem is the same as in Eq. (3.36), however, this has to be evaluated at each angular velocity. Instead, the right side term, similarly to Eq. (3.36), is the derivative of the mass, damping, and stiffness matrices with respect to the angular velocity was evaluated.

By solving this system, the sensitivity of the eigenvalue and eigenvector to the angular velocity is obtained. This allows us to update them for the next increment of angular velocity. Specifically, the eigenvalues and eigenvectors will be updated as follows:

$$\lambda_{\mathrm{next}} = \lambda_{\mathrm{previous}} + \lambda_{/\Omega}\,\Delta\Omega \tag{3.38}$$

$$\mathbf{q}_{\mathrm{next}} = \mathbf{q}_{\mathrm{previous}} + \mathbf{q}_{/\Omega}\,\Delta\Omega \tag{3.39}$$

3.4. Sensitivity Results

The result obtained from solving the system of Eqs. (3.36) is a vector whose first 8 terms represent $\frac{\partial \mathbf{q}}{\partial p}$, i.e., the sensitivity of the eigenvector with respect to p, while the last term represents the sensitivity of the eigenvalue with respect to p, i.e., $\frac{\partial \lambda}{\partial p}$.

If the real part of λ is positive, the system is unstable (with exponential growth). Conversely, if it is negative, the system is stable (with exponential decay).

The derivative $\frac{\partial \lambda}{\partial p}$ indicates how the stability of the system varies with respect to the parameter p:

- If $\frac{\partial \lambda}{\partial p} > 0$, the stability worsens, and the system becomes more unstable.
- If $\frac{\partial \lambda}{\partial p} < 0$, the stability improves, making the system more stable.

Starting from the reference condition of Fig. 3.2, the sensitivity of the eigenvalues with respect to the given parameter is analyzed. Subsequently, the real and imaginary parts of the sensitivity are plotted.

To verify the accuracy of this method, Appendix B provides, for each parameter, a comparison between the eigenvalues obtained by directly modifying the geometrical parame-

ters of the GR problem and those computed using the sensitivity-based evolution of the eigenvalues.

3.4.1. Chordwise Position of Damper Attachments

The sensitivity to variations in the offset along the chord of the damper attachment points was evaluated using the method described earlier.

The sensitivity of the eigensolution with respect to the chordwise parameter is investigated for a positive perturbation:

$$a = a_0 + \Delta, \quad b = b_0 + \Delta \tag{3.40}$$

each case separately, where the value $_0$ stands for the reference value.

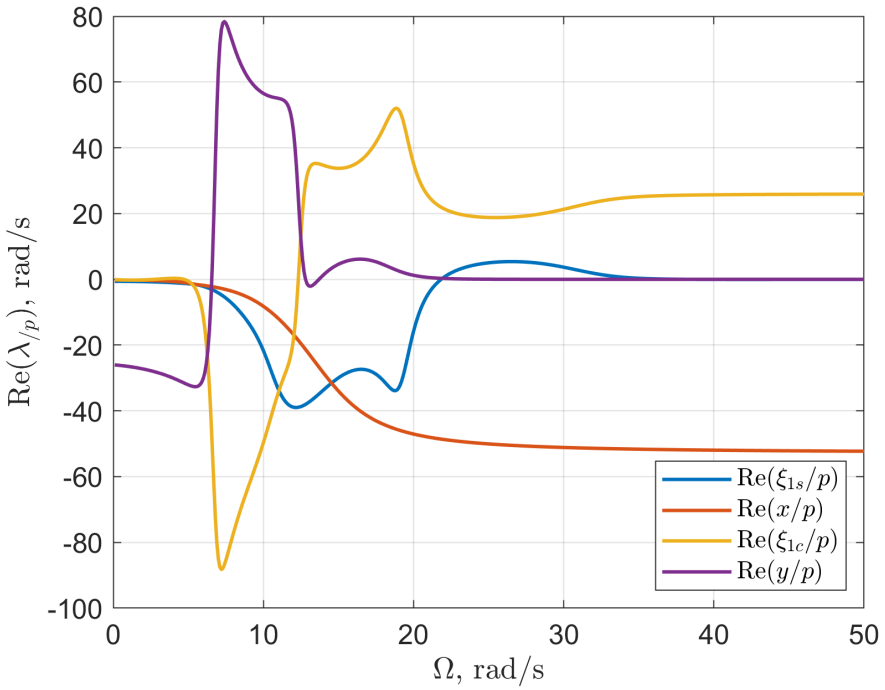

Figure 3.3: Real part of the sensitivity of the eigenvalues with respect to the chordwise attachment position on the blades as a function of Ω, for a positive perturbation of parameter a

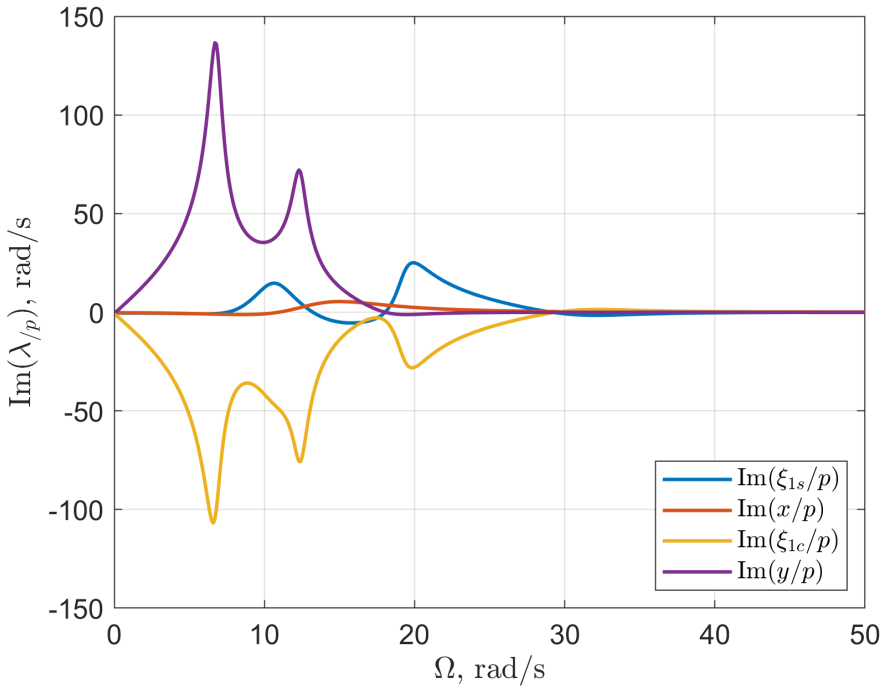

Figure 3.4: Imaginary part of the sensitivity of the eigenvalues with respect to the chord-wise attachment position on the blades as a function of Ω, for a positive perturbation of parameter a

For a positive perturbation of parameter b, due to the symmetry of the geometry, the results are the same of the perturbation to the parameters b.

3.4.2. Radial Position of Damper Attachment Points

Similarly to the previous case, the sensitivity of the eigenvalues to a perturbation in the radial parameter has been investigated. Referring to Fig. 3.1, the parameters describing the radial position of the damper attachments are defined as follows:

$$c_a = c_0 + \Delta, \quad c_b = c_0 + \Delta. \tag{3.41}$$

The derivative of the global damping and stiffness matrix with respect to this parameter was then evaluated, and the eigenvalues of the system were subsequently analyzed. Due to the symmetry of the configuration chosen, Fig. 3.1, the eigenvalue derivatives are equal regardless of whether the perturbation is on the left or right side (c_a or c_b), so only the derivatives with respect to c_a are reported.

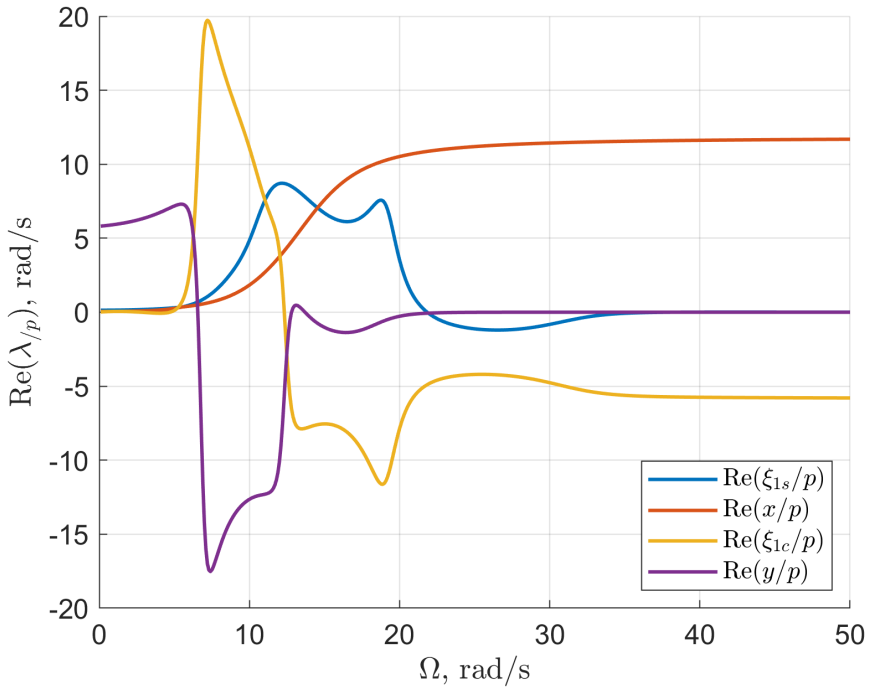

Figure 3.5: Real part of the sensitivity of the eigenvalues with respect to the radial attachment position parameter as a function of Ω, for a positive perturbation of parameter c_a

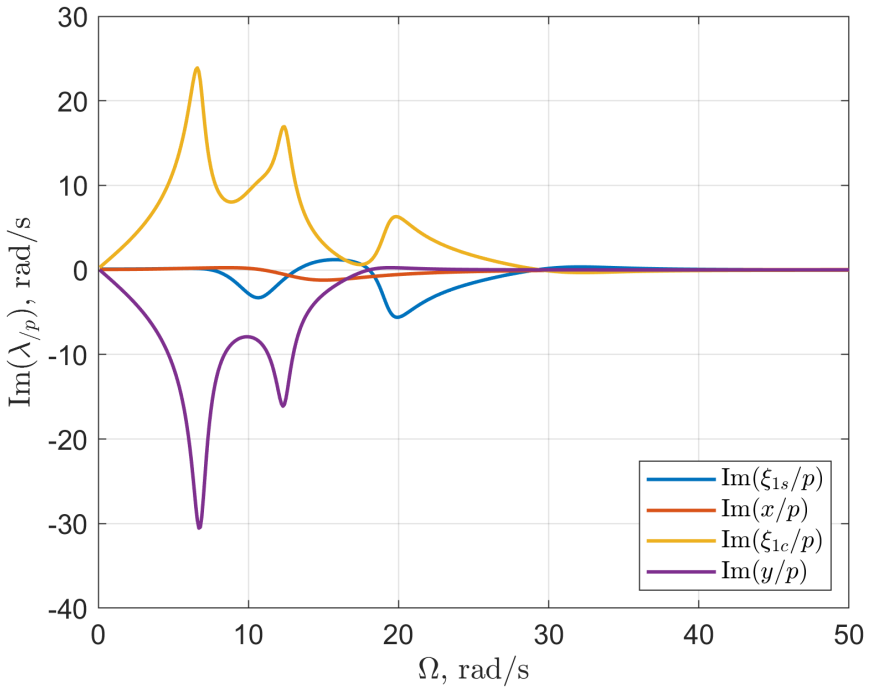

Figure 3.6: Imaginary part of the sensitivity of the eigenvalues with respect to the radial attachment position parameter as a function of Ω, for a positive perturbation of parameter c_a

3.4.3. Parameters Related to the Central Blade

Referring to the configuration in 3.1, the influence of geometric parameters related to the position of the dampers with respect to the central blade has been investigated. The azimuthal angle of the blade is given by $\xi^{(m+1)}$, while the lengths of the damper arms connecting to the blade, d and f, and the hinge position along the blade is described by the parameter c_d.

Arm Lengths

The lengths d and f, which attach to the points D_{i+1} and F_{i+1} respectively, are expressed as follows.

$$d = r_0 + \Delta, \quad f = r_0 + \Delta \tag{3.42}$$

The derivative of the damping matrix with respect to this parameter was calculated, and the sensitivity of the eigenvalues of the GR system to this parameter were evaluated.

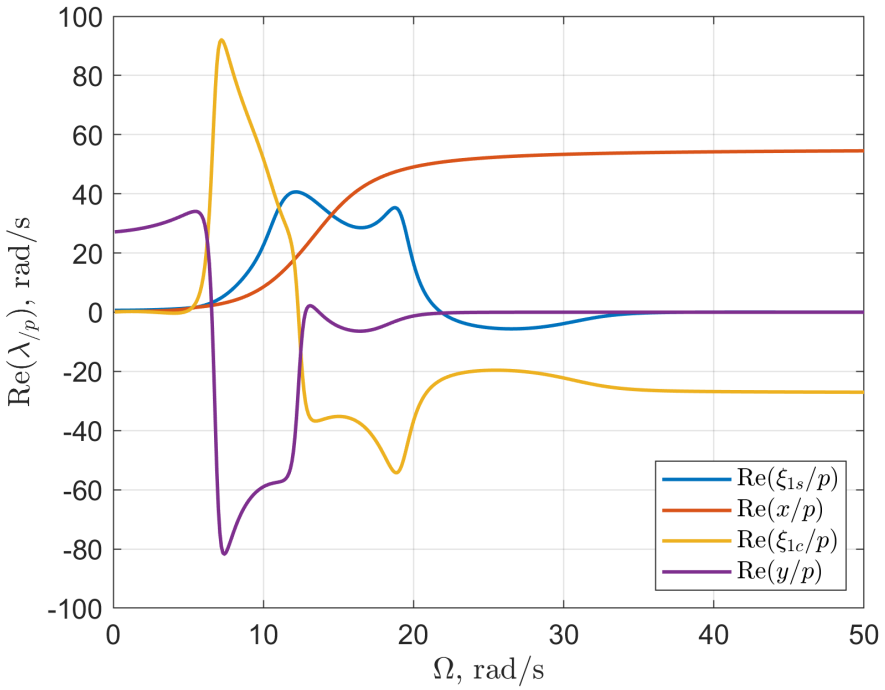

Figure 3.7: Real part of the sensitivity of the eigenvalues with respect to the link arms to the central blade as a function of Ω, for a positive perturbation of parameter d

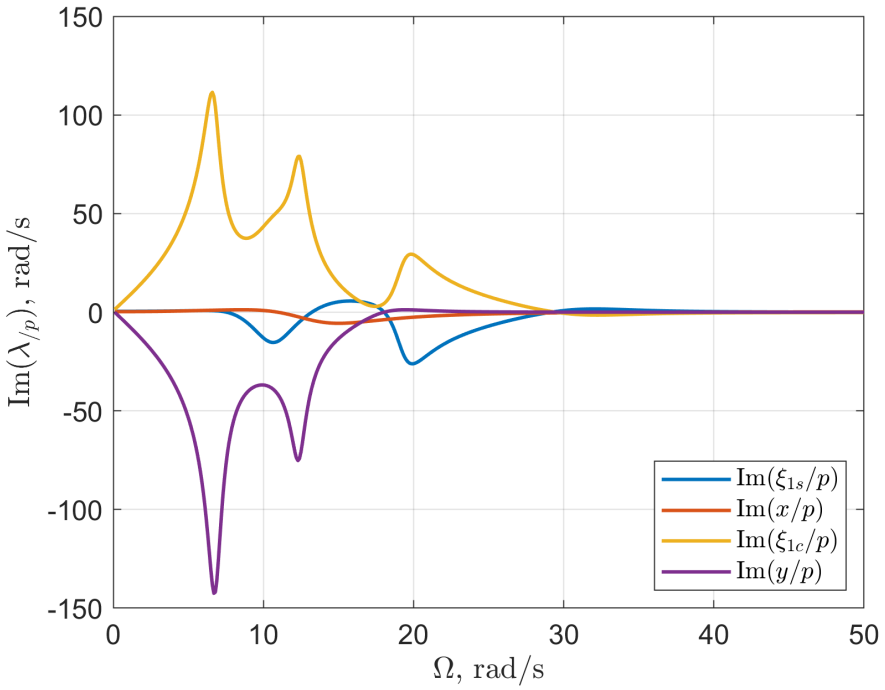

Figure 3.8: Imaginary part of the sensitivity of the eigenvalues with respect to the link arms to the central blade as a function of Ω, for a positive perturbation of parameter d

Radial Position of the Hinge on the Central Blade

Regarding the geometry of the damper on the blade with azimuthal angle ξ_{i+1}, the sensitivity of the eigenvalues to the hinge position has also been investigated. In the adopted geometry, this is represented by the parameters c_d and c_f.

$$c_d = c_f = c_0 \pm \Delta \tag{3.43}$$

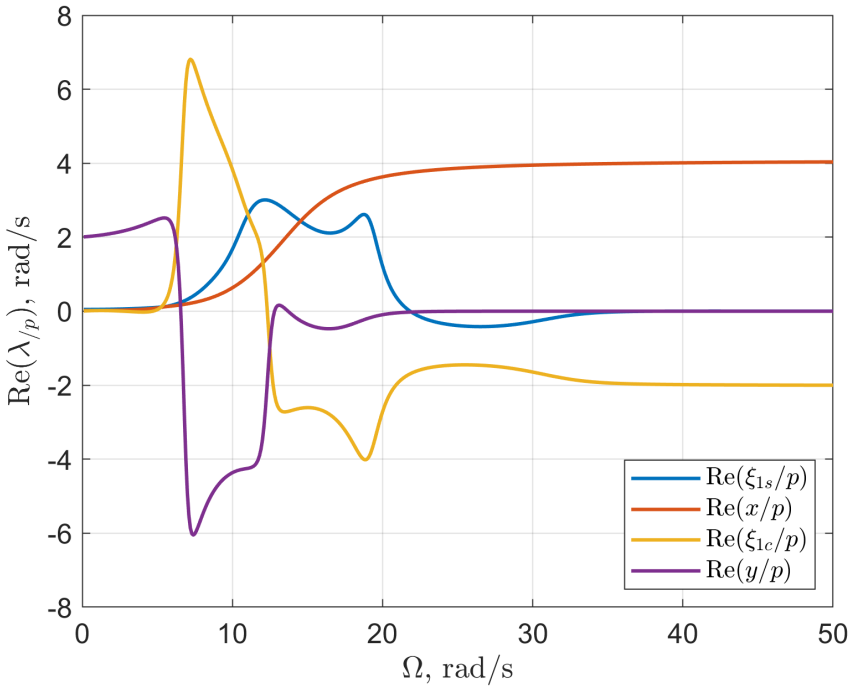

Figure 3.9: Real part of the sensitivity of the eigenvalues with respect to hinge position along the intermediate blade Ω, for a positive perturbation of parameter d

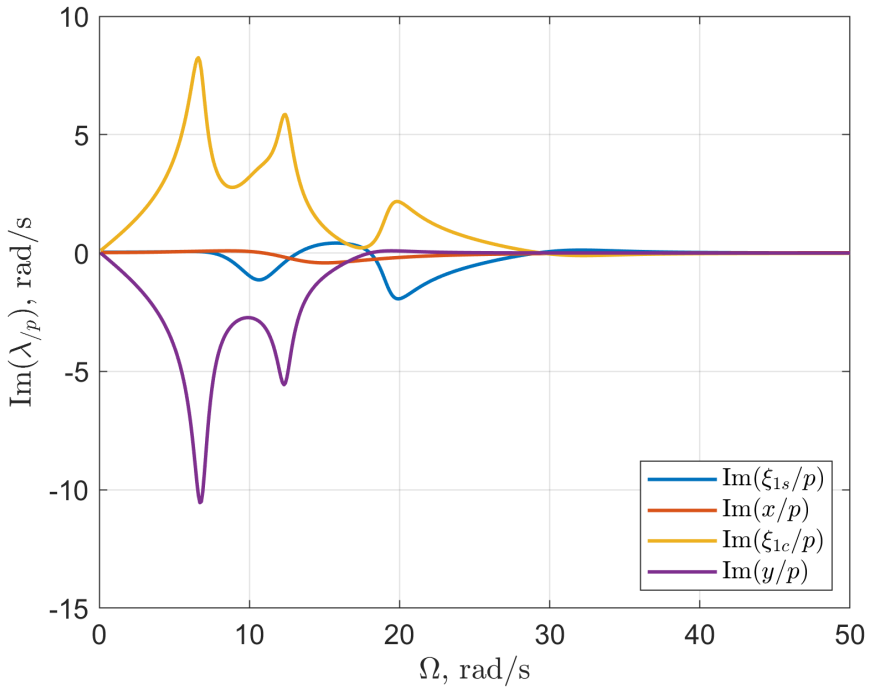

Figure 3.10: Imaginary part of the sensitivity of the eigenvalues with respect to hinge position along the intermediate blade Ω, for a positive perturbation of parameter d

3.5. Application of Sensitivity Analysis

Once the sensitivity of each eigenvalue with respect to the geometrical parameters presented in Table 3.2 has been computed, the sensitivity-based approach can be extended to formulate and solve various optimization problems. This methodology proves particularly useful in guiding design modifications aimed at improving the dynamic stability of the rotor system.

By leveraging the computed sensitivities, it becomes possible to define objective functions and constraints directly in terms of eigenvalue behavior. The following subsections demonstrate how this theoretical framework can be applied across different scenarios and how it will be applied in the next chapters of the thesis.

3.5.1. Influence of a Single Parameter on the Modal Damping

As shown in the previous analysis, the behavior of the system due to a geometrical change in the length of one of the parameters can be determined by knowing the sensitivity of the eigenvalues to that parameter. In fact, at each angular velocity, the sensitivity of the eigenvalue to the parameter is known by solving Eq. (3.36). The new value of the real

part of the eigenvalue can then be determined as follows:

$$\mathrm{Re}(\lambda_i) = \mathrm{Re}(\lambda_{i,0}) + \mathrm{Re}\left(\lambda_i/p\right) \cdot (p - p_0) \tag{3.44}$$

Thus, for a given angular velocity Ω, with a variation of one of the geometrical parameters $p - p_0$, the real part of the eigenvalue can be computed. By observing the modal damping, it can be determined whether the system will remain stable in this new configuration.

This is precisely what has been carried out in Chapter 3, where the variation of individual geometrical parameters was used to assess the modal evolution of the system.

3.5.2. Combination of Multiple Parameter Sensitivities to Achieve Prescribed Damping of a Specific Eigenvalue

Knowing the sensitivity of the eigenvalue λ_i to multiple parameters, a linear system can be developed in order to find a combination of those parameters to achieve a desired damping of the mode.

So the following linear system, in this case with only two parameters, can be determined to obtain a desired modal damping:

$$\mathrm{Re}(\lambda_i) = \mathrm{Re}(\lambda_{i,o}) + \mathrm{Re}(\lambda_{i/p_1}) \cdot (p_1 - p_{1,0}) + \mathrm{Re}(\lambda_{i/p_2}) \cdot (p_2 - p_{2,0}) \tag{3.45}$$

By solving this linear system, the parameters can be tuned to achieve a specific modal damping. This is particularly useful for optimization tasks in systems where fine-tuning of geometrical or physical parameters is required to meet stability or performance objectives.

In the present thesis, this approach is employed to tune the damper characteristics by exploiting the sensitivity of the critical regressive eigenvalue with respect to the damper coefficients K_d and C_d. Specifically, this methodology is applied to different damper configurations to ensure the prescribed damping on the targeted mode.

In § 4.2.5, it is used to reproduce an equivalent BTH model that matches the damping on mode ξ_{1_c} of the IB configuration. Similarly, in § 4.3.3, the damper coefficients of the I2B configuration are tuned to achieve the same damping level on mode ξ_{1_c}.

3.5.3. Combination of Multiple Parameter Sensitivities to Achieve Prescribed Damping of Multiple Eigenvalues

The system in Eq. (3.45) can be extended to a more complex scenario, in which we choose a combination of the geometrical parameters to achieve a particular damping on a certain eigenvalue while maintaining the damping on another different eigenvalue unchanged at the same time.

$$\begin{cases} \mathrm{Re}(\lambda_i) = \mathrm{Re}(\lambda_{i,0}) + \mathrm{Re}(\lambda_{i/p_1}) \cdot (p_1 - p_{1,0}) + \mathrm{Re}(\lambda_{i/p_2}) \cdot (p_2 - p_{2,0}) + \mathrm{Re}(\lambda_{i/p_3}) \cdot (p_3 - p_{3,0}) \\ \mathrm{Re}(\lambda_{j,0}) = \mathrm{Re}(\lambda_{j,0}) + \mathrm{Re}(\lambda_{j/p_1}) \cdot (p_1 - p_{1,0}) + \mathrm{Re}(\lambda_{j/p_2}) \cdot (p_2 - p_{2,0}) + \mathrm{Re}(\lambda_{j/p_3}) \cdot (p_3 - p_{3,0}) \end{cases} \tag{3.46}$$

By developing this system, it is possible to identify a combination of parameters p_1, p_2, p_3 that achieves the desired modal damping of a specific eigenvalue λ_i, i.e., $\mathrm{Re}(\lambda_i)$, while maintaining the damping of another eigenvalue λ_j unchanged, such that:

$$\mathrm{Re}(\lambda_j) = \mathrm{Re}(\lambda_{j,0}) \tag{3.47}$$

In this thesis, the presented approach is used in a slightly different manner to tune the damper coefficients for an I2B configuration, as described in § 4.3.4. By exploiting the sensitivity of the modal damping with respect to all relevant geometrical parameters of the kinematic model, as well as the damper characteristics, and applying the continuation approach, the parameters are tuned to achieve prescribed damping on both the collective mode ξ_0 and the cyclic regressive mode ξ_{1_c}. This ensured the realization of an equivalent I2B configuration that allows for a more meaningful and in-depth comparison with the corresponding IB model.

3.5.4. Application of the Sensitivity Approach in the Case of Damper Failure

As outlined in § 1.1, assessing the dynamic stability of the helicopter throughout the 40%–120% range of nominal rotor speed remains essential, even in scenarios involving damper malfunction. The asymmetry introduced by such a failure compromises the system's periodicity, making it impossible to simplify the dynamics as in the ADO framework. As a result, solving the GR equations under ODI conditions requires integrating the system

across discrete azimuthal positions for each rotor speed.

To enable sensitivity-based analysis in this failure configuration, two computational strategies have been developed as explained in § 2.5.

The first relies on direct numerical integration of the GR equations at every time–azimuth point and for each rotational velocity, employing a fourth-order Runge-Kutta scheme.

The second strategy adopts Hsu's method, which yields comparable results and offers distinct advantages for sensitivity analysis. In particular, this formulation produces a monodromy matrix **H**, in a form that facilitates its eigenvalue sensitivity evaluation under parameter perturbations, as demonstrated in [17].

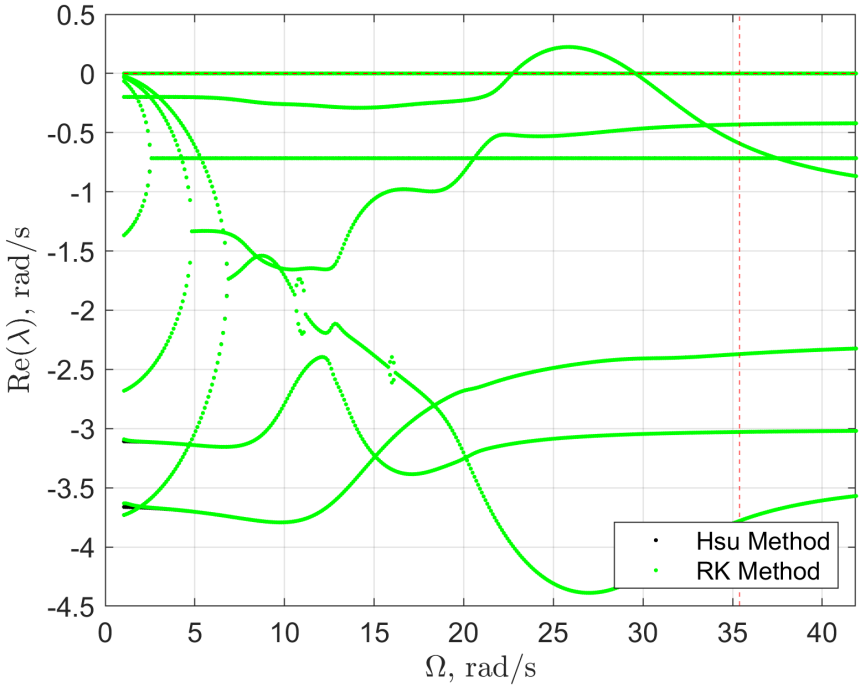

Figure 3.11: Eigenvalues of the system as function of Ω, in case of a damper failure (I2B config.), comparison between methods

Sensitivity Problem in Case of ODI

In this section is reported and implemented, the method proposed in [17] to compute the sensitivity of the monodromy matrix to different geometrical parameters.

The monodromy matrix is the one that governs the state space description of the problem reported in Eq. (2.30).

Having defined the matrix **A** as the matrix that, integrated at each azimuth step, describes

the evolution of the system after a failure of a damper, the monodromy matrix $\mathbf{H}$, using Hsu's method, has been computed in the following:

$$\mathbf{H} = \mathbf{Y}_N \mathbf{Y}_{N-1} ... \mathbf{Y}_2 \mathbf{Y}_1 \mathbf{Y}_0 \tag{3.48}$$

where

$$\mathbf{Y}_n = \mathrm{e}^{\hat{\mathbf{A}}_n \ \Delta t} \tag{3.49}$$

$$\hat{\mathbf{A}}_n = (\mathbf{A}(n+1) + \mathbf{A}(n))/2; \tag{3.50}$$

From the implementation of the Hsu method, the sensitivity of the monodromy matrix with respect to one of the geometrical parameters of the problem p can be formulated as:

$$\begin{aligned} \mathbf{H}_{/p} = & \mathbf{Y}_{N/p} \mathbf{Y}_{N-1} ... \mathbf{Y}_2 \mathbf{Y}_1 \\ & + \mathbf{Y}_N \mathbf{Y}_{N-1/p} ... \mathbf{Y}_2 \mathbf{Y}_1 \\ & + \mathbf{Y}_N \mathbf{Y}_{N-1} ... \mathbf{Y}_{2/p} \mathbf{Y}_1 \end{aligned} \tag{3.51}$$

Due to the expression of $\mathbf{Y}_n$, its derivative will be:

$$\mathbf{Y}_{n/p} = \hat{\mathbf{A}}_{n/p} \Delta t \ \mathrm{e}^{\hat{\mathbf{A}}_n \Delta t} = \hat{\mathbf{A}}_{n/p} \Delta t \ \mathbf{Y}_n \tag{3.52}$$

So the derivative of the monodromy matrix can be reformulated as:

$$\begin{aligned} \mathbf{H}_{/p} = & \hat{\mathbf{A}}_{N/p} \Delta t \mathbf{Y}_N \mathbf{Y}_{N-1} ... \mathbf{Y}_2 \mathbf{Y}_1 \\ & + \mathbf{Y}_N \hat{\mathbf{A}}_{N-1/p} \Delta t \mathbf{Y}_{N-1/p} ... \mathbf{Y}_2 \mathbf{Y}_1 \\ & + \mathbf{Y}_N \mathbf{Y}_{N-1} ... \hat{\mathbf{A}}_{2/p} \Delta t \mathbf{Y}_{2/p} \mathbf{Y}_1 \end{aligned} \tag{3.53}$$

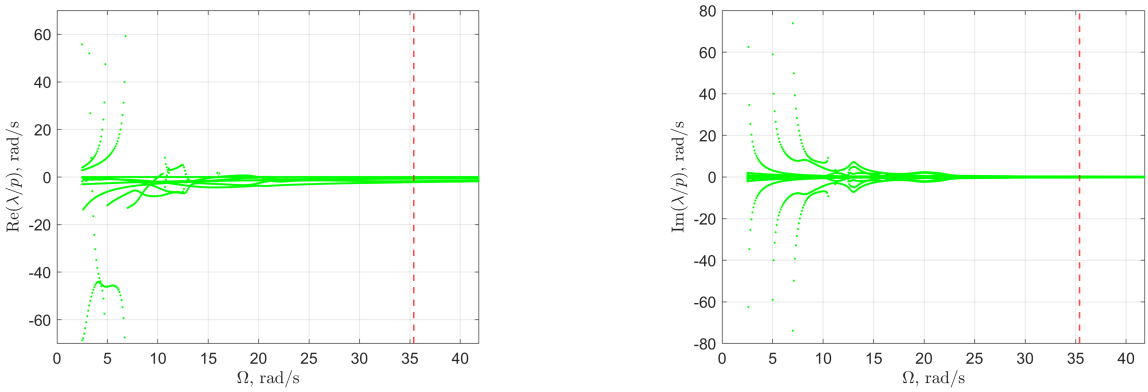

Figure 3.12: Real and imaginary part of the sensitivity of the eigenvalues of the GR problem in case of damper failure, respect the chordwise position of the damper arms.

In Fig. 3.12 the sensitivity of all the eigenvalues of the entire GR problem is reported in the case of a failure of the first damper with respect to the chordwise parameter. Similarly to the ADO problem, from the computation of these values it is possible to assess how a perturbation in the length affects the eigenvalue evolution and, consequently, the system stability.

4 | Analysis of Realistic Damper Configurations

This chapter presents a methodology for integrating a detailed damper kinematic model with a "black-box" rotor model that encapsulates the rotor's aeromechanical behavior. The objective is to obtain a representative coupled model capable of accurately predicting the dynamic response of the system, accounting for both the mechanical characteristics of the damper and the complex aeroelastic interactions within the rotor.

The results presented are initially based on a simplified rotor structural dynamics model, as proposed by Hammond. Nevertheless, the methodology is formulated in a general framework, allowing its application to a broad range of damper configurations and kinematics. A realistic IB model, representative of a modern medium-weight helicopter, is introduced in § 4.2. Subsequently, in § 4.3, equivalent BTH and I2B configurations are developed. These models are obtained by exploiting the eigenvalue sensitivity method, applied to the GR problem as discussed in Chapter 3. This approach enables the tuning of the rotor model to achieve equivalent damping on both the cyclic regressive mode and the collective mode, thus ensuring a consistent dynamic response across different damper arrangements.

The generality of the proposed formulation and the structure of the assembled problem allow its implementation within MASST—a modern aeroelastic state-space tool developed in collaboration between Politecnico di Milano and Leonardo Helicopters Division. MASST, being an industrial-grade software capable of simulating complex dynamic systems, provides a valuable platform for further verification of the developed models, as will be discussed in Chapter 5.

4.1. General Model

The general formulation of the second-order differential equation governing the dynamic behavior of the rotor, regardless of the specific damper arrangement, can be written as:

$$\mathbf{A}_2\ddot{\mathbf{x}}_m + \mathbf{A}_1\dot{\mathbf{x}}_m + \mathbf{A}_0\mathbf{x}_m = \mathbf{B}\mathbf{u} + \mathbf{f} \tag{4.1}$$

$$\mathbf{y} = \mathbf{C}\mathbf{x}_m + \cancel{\mathbf{D}\mathbf{u}} \tag{4.2}$$

where $\mathbf{x}_m$ represents the state vector of the system, $\mathbf{u}$ denotes the input vector, and $\mathbf{f}$ is the general forcing term. By assembling the system using a general formulation, it is important to note that the output vector $\mathbf{y}$ does not necessarily coincide with the state vector $\mathbf{x}_m$.

Assuming that the blade lag rotation angles, $\xi^{(m)}$, with $m = 1..N_b$, collected in vector $\boldsymbol{\xi}$,

$$\boldsymbol{\xi} = \begin{Bmatrix} \xi^{(1)} \\ \xi^{(2)} \\ \cdots \\ \xi^{(N_b)} \end{Bmatrix} \tag{4.3}$$

can be extracted from the output as

$$\boldsymbol{\xi} = \mathbf{C}_{\xi y}\mathbf{y}, \tag{4.4}$$

considering that the input vector $\mathbf{u}$ can be constructed from the lag moments about the blade, $m_\xi^{(m)}$, collected in vector $\mathbf{m}_\xi$,

$$\mathbf{m}_\xi = \begin{Bmatrix} m_\xi^{(1)} \\ m_\xi^{(2)} \\ \cdots \\ m_\xi^{(N_b)} \end{Bmatrix} \tag{4.5}$$

as

$$\mathbf{u} = \mathbf{B}_{u\xi}\mathbf{m}_\xi \tag{4.6}$$

The inputs of the rotor model are the lag moments acting on each blade. However, since rotational dampers are considered, these moments can be more conveniently computed by introducing the relative rotation of each mth damper, denoted $\varphi^{(m)}$, and collected in the vector $\boldsymbol{\varphi}$. Therefore, it is necessary to establish a relationship between the rotation of

each damper and the corresponding blade lag angles. In a general framework, the relative rotation of a given damper may depend not solely on the lag motion of multiple blades, as in the Hammond-type formulation, but can be extended to account for the full set of blade motions — including pitch, flap, and lag degrees of freedom — of multiple blades.

To include the dampers as external contributions to the system, their effect is introduced through the corresponding virtual work expression.

$$\sum_m \delta\xi^{(m)} m_\xi^{(m)} = \sum_m \delta\varphi^{(m)} m_\varphi^{(m)} \tag{4.7}$$

where $\varphi^{(m)}$ is the rotation of the mth damper and $m_\varphi^{(m)}$ is the corresponding moment, with

$$m_\varphi^{(m)} = -K_\varphi \left(\varphi^{(m)} - \varphi_{\text{ref}}\right) - C_\varphi \dot{\varphi}^{(m)} \tag{4.8}$$

when a simple linear visco-elastic constitutive law is considered (alternatively, a general function $m_\varphi^{(m)} = m_\varphi(\varphi^{(m)}, \dot{\varphi}^{(m)})$ needs to be considered).

The virtual work equivalence can be generalized as

$$\delta\boldsymbol{\xi}^T \mathbf{m}_\xi = \delta\boldsymbol{\varphi}^T \mathbf{m}_\varphi \tag{4.9}$$

with

$$\boldsymbol{\varphi} = \left\{ \begin{array}{c} \varphi^{(1)} \\ \varphi^{(2)} \\ \cdots \\ \varphi^{(N_b)} \end{array} \right\} \tag{4.10}$$

$$\mathbf{m}_\varphi = \left\{ \begin{array}{c} m_\varphi^{(1)} \\ m_\varphi^{(2)} \\ \cdots \\ m_\varphi^{(N_b)} \end{array} \right\} \tag{4.11}$$

The blades and dampers' kinematics can be expressed as a function of a set of damper internal coordinates $\mathbf{x}_d \in \mathbb{R}^{N_b N_d}$, i.e., N_d coordinates for each damper (at least $N_d \geq 1$ for the damper rotation). The introduction of the internal kinematics of the dampers extends the applicability of this method, allowing for increased complexity in the kinematic chain. As will be discussed later, § 3.2.1, this enables the inclusion of individual joints and their respective contributions to the overall stiffness and damping characteristics of the system.

The linearized damper rotation can be expressed as a function of the internal coordinates

as

$$\boldsymbol{\varphi} = \mathbf{C}_{\varphi x_d}\mathbf{x}_d. \tag{4.12}$$

A "closure" relationship is established between the dampers' internal coordinates, $\mathbf{x}_d$, and those of the blades, $\boldsymbol{\xi}$, of the form

$$\boldsymbol{\phi}\left(\boldsymbol{\xi}, \mathbf{x}_d\right) = \mathbf{0} \tag{4.13}$$

such that

$$\mathbf{0} = \delta\boldsymbol{\phi} = \boldsymbol{\phi}_{/\boldsymbol{\xi}}\delta\boldsymbol{\xi} + \boldsymbol{\phi}_{/\mathbf{x}_d}\delta\mathbf{x}_d \tag{4.14}$$

which can be used to determine a relationship between the virtual rotations of the blades and the virtual perturbations of the dampers' internal states, namely

$$\boldsymbol{\phi}_{/\mathbf{x}_d}\delta\mathbf{x}_d = -\boldsymbol{\phi}_{/\boldsymbol{\xi}}\delta\boldsymbol{\xi} \tag{4.15}$$

so that, after expressing the virtual perturbation of the damper rotations as

$$\delta\boldsymbol{\varphi} = \mathbf{C}_{\varphi x_d}\delta\mathbf{x}_d = -\mathbf{C}_{\varphi x_d}\boldsymbol{\phi}^{-1}_{/\mathbf{x}_d}\boldsymbol{\phi}_{/\boldsymbol{\xi}}\delta\boldsymbol{\xi} = \Psi\delta\boldsymbol{\xi} \tag{4.16}$$

the generalized moments about the lead-lag hinges can be written as

$$\mathbf{m}_\xi = \Psi^T\mathbf{m}_\varphi \tag{4.17}$$

In the end, the equations governing the problem can be written as

$$\mathbf{A}_2\ddot{\mathbf{x}}_m + \mathbf{A}_1\dot{\mathbf{x}}_m + \mathbf{A}_0\mathbf{x}_m = \mathbf{B}\mathbf{B}_{u\xi}\boldsymbol{\Psi}^T\mathbf{m}_\varphi + \mathbf{f} \tag{4.18a}$$

$$\mathbf{m}_\varphi = -\mathbf{K}_\varphi\left(\boldsymbol{\Psi}\xi - \varphi_{\text{ref}}\right) - \mathbf{C}_\varphi\boldsymbol{\Psi}\dot{\xi} \tag{4.18b}$$

$$\boldsymbol{\xi} = \mathbf{C}_{\xi y}\mathbf{C}\mathbf{x}_m \tag{4.18c}$$

$$\phi\left(\xi, \mathbf{x}_d\right) = \mathbf{0} \tag{4.18d}$$

with $\mathbf{x}_m \in \mathbb{R}^{N_m}$, $\mathbf{m}_\varphi \in \mathbb{R}^{N_b}$, $\xi \in \mathbb{R}^{N_b}$, and $\mathbf{x}_d \in \mathbb{R}^{N_b N_d}$,

where

$$\dot{\boldsymbol{\xi}} = \mathbf{C}_{\xi y}\mathbf{C}\dot{\mathbf{x}}_m \qquad \in \mathbb{R}^{N_b}, \text{ with } \dot{\boldsymbol{\xi}} \in \mathbb{R}^{N_b} \tag{4.19a}$$

$$\boldsymbol{\phi}_{/\boldsymbol{\xi}}\dot{\boldsymbol{\xi}} + \boldsymbol{\phi}_{/\mathbf{x}_d}\dot{\mathbf{x}}_d = \mathbf{0} \qquad \in \mathbb{R}^{N_b N_d}, \text{ with } \dot{\mathbf{x}}_d \in \mathbb{R}^{N_b N_d} \tag{4.19b}$$

The unknowns are $\mathbf{x}_m \in \mathbb{R}^{N_m}$, $\mathbf{m}_\varphi \in \mathbb{R}^{N_b}$, and $\mathbf{x}_d \in \mathbb{R}^{N_b N_d}$, for a total of $N_m + N_b(1+N_d)$. The equations are $N_m + N_b + N_b N_d = N_m + N_b(1+N_d)$. Equation $\boldsymbol{\xi} = \mathbf{C}_{\xi y}\mathbf{C}\mathbf{x}_m$ can be directly replaced;while equation $\boldsymbol{\phi} = \mathbf{0}$ completely defines the variables $\mathbf{x}_d$, and thus $\boldsymbol{\varphi}$.

After finding a steady solution for the nonlinear problem (made nonlinear by $\boldsymbol{\phi}$ and possibly by the constitutive law of equation $\mathbf{m}_\varphi$ for generic dampers),

$$\mathbf{A}_0\mathbf{x}_{m_0} = \mathbf{B}\mathbf{B}_{u\xi}\Psi^T\mathbf{m}_{\varphi_0} + \mathbf{f}_0 \tag{4.20}$$

$$\mathbf{m}_{\varphi_0} = -\mathbf{K}_\varphi\left(\mathbf{C}_{\varphi x_d}\mathbf{x}_{d_0} - \boldsymbol{\varphi}_{\text{ref}}\right) \tag{4.21}$$

$$\boldsymbol{\xi}_0 = \mathbf{C}_{\xi y}\mathbf{C}\mathbf{x}_{m_0} \tag{4.22}$$

$$\boldsymbol{\phi}\left(\boldsymbol{\xi}_0, \mathbf{x}_{d_0}\right) = \mathbf{0} \tag{4.23}$$

the problem can be consistently linearized, introducing

$$\left\{ \begin{array}{c} \dot{\mathbf{x}}_m \\ \dot{\mathbf{x}}_d \end{array} \right\} = \mathbf{T}\dot{\mathbf{x}}_m \tag{4.24}$$

where $\mathbf{T}$ is the projection matrix. Consider the time derivative of function $\boldsymbol{\phi}$,

$$\boldsymbol{\phi}_{/\boldsymbol{\xi}}\dot{\boldsymbol{\xi}} + \boldsymbol{\phi}_{/\mathbf{x}_d}\dot{\mathbf{x}}_d = \mathbf{0} \tag{4.25}$$

and replace $\dot{\boldsymbol{\xi}} = \mathbf{C}_{\xi y}\mathbf{C}\dot{\mathbf{x}}_m$, yielding

$$\boldsymbol{\phi}_{/\boldsymbol{\xi}}\mathbf{C}_{\xi y}\mathbf{C}\dot{\mathbf{x}}_m + \boldsymbol{\phi}_{/\mathbf{x}_d}\dot{\mathbf{x}}_d = \mathbf{0} \tag{4.26}$$

Matrix $\mathbf{T}$ is

$$\mathbf{T} = \left[\begin{array}{c} \mathbf{I} \\ -\boldsymbol{\phi}_{/\mathbf{x}_d}^{-1}\boldsymbol{\phi}_{/\boldsymbol{\xi}}\mathbf{C}_{\xi y}\mathbf{C} \end{array} \right] \tag{4.27}$$

Linearization about steady configuration. For the coordinates:

$$\left\{ \begin{array}{c} \Delta\mathbf{x}_m \\ \Delta\mathbf{x}_d \end{array} \right\} = \mathbf{T}\Delta\mathbf{x}_m \qquad \left\{ \begin{array}{c} \Delta\dot{\mathbf{x}}_m \\ \Delta\dot{\mathbf{x}}_d \end{array} \right\} = \mathbf{T}\Delta\dot{\mathbf{x}}_m \qquad \left\{ \begin{array}{c} \Delta\ddot{\mathbf{x}}_m \\ \Delta\ddot{\mathbf{x}}_d \end{array} \right\} = \mathbf{T}\Delta\ddot{\mathbf{x}}_m \tag{4.28}$$

For the damper moment:

$$\Delta\mathbf{m}_\varphi = -\mathbf{K}_\varphi\Delta\boldsymbol{\varphi} - \mathbf{C}_\varphi\Delta\dot{\boldsymbol{\varphi}} \tag{4.29}$$

the latter is also valid in the case of nonlinear damper characteristics.

Replacing the linearized damper moment in the EoM, namely

$$\mathbf{A}_2\Delta\ddot{\mathbf{x}}_m + \mathbf{A}_1\Delta\dot{\mathbf{x}}_m + \mathbf{A}_0\Delta\mathbf{x}_m = \mathbf{B}\mathbf{B}_{u\xi}\boldsymbol{\Psi}^T\Delta\mathbf{m}_\varphi \tag{4.30}$$

The problem, expanded, becomes

$$\begin{aligned}
&\begin{bmatrix} \mathbf{A}_2 & \mathbf{0} \\ \mathbf{0} & \mathbf{0} \end{bmatrix} \begin{Bmatrix} \Delta\ddot{\mathbf{x}}_m \\ \Delta\ddot{\mathbf{x}}_d \end{Bmatrix} \\
&+ \begin{bmatrix} \mathbf{A}_1 & \mathbf{B}\mathbf{B}_{u\xi}\Psi^T\mathbf{C}_\varphi\Psi\mathbf{C}_{\xi y}\mathbf{C} \\ \mathbf{0} & \mathbf{0} \end{bmatrix} \begin{Bmatrix} \Delta\dot{\mathbf{x}}_m \\ \Delta\dot{\mathbf{x}}_d \end{Bmatrix} \\
&+ \begin{bmatrix} \mathbf{A}_0 & \mathbf{B}\mathbf{B}_{u\xi}\Psi^T\mathbf{K}_\varphi\Psi\mathbf{C}_{\xi y}\mathbf{C} \\ \boldsymbol{\phi}_{/\boldsymbol{\xi}}\mathbf{C}_{\xi y}\mathbf{C} & \boldsymbol{\phi}_{/\mathbf{x}_d} \end{bmatrix} \begin{Bmatrix} \Delta\mathbf{x}_m \\ \Delta\mathbf{x}_d \end{Bmatrix} = \begin{Bmatrix} \mathbf{0} \\ \mathbf{0} \end{Bmatrix}
\end{aligned} \tag{4.31}$$

Replacing the above-described perturbations and premultiplying by $\mathbf{T}^T$ yields

$$\mathbf{A}_2\Delta\ddot{\mathbf{x}}_m + \left(\mathbf{A}_1 + \mathbf{B}\mathbf{B}_{u\xi}\Psi^T\mathbf{C}_\varphi\Psi\mathbf{C}_{\xi y}\mathbf{C}\right)\Delta\dot{\mathbf{x}}_m + \left(\mathbf{A}_0 + \mathbf{B}\mathbf{B}_{u\xi}\Psi^T\mathbf{K}_\varphi\Psi\mathbf{C}_{\xi y}\mathbf{C}\right)\Delta\mathbf{x}_m = \mathbf{0} \tag{4.32}$$

The general formulation of the approach enables the modeling of a wide range of damping configurations. Notably, no specific assumptions regarding the damper arrangement or kinematic layout are introduced explicitly; instead, all such information is implicitly embedded within the closure equations $\boldsymbol{\phi}$ and the transformation matrix Ψ.

4.2. Interblade Model

The general method presented in § 4.1 is now applied considering an IB setup in two dimensions with a rotational damper mounted on blade m and connected to blade $m+1$ by a rod.

4.2.1. Geometry and Kinematic Model Definition

The geometrical data for the IB rotor model with chordwise and radial damper offset are reported in Table 4.1.

The relevant points that define the IB kinematic chosen are the following:

- Each lead-lag hinge presents an offset in x direction, if we consider a rotor with a

blade, with an angle of zero degrees with respect to the x direction:

$$\mathbf{H}^{(m)} = \begin{pmatrix} x_h \\ 0 \\ 0 \end{pmatrix} \tag{4.33}$$

Considering then a new local frame of reference centered on the lead-lag hinge, with $\tilde{x}$ along the blade and $\tilde{y}$ along the chord.

- The position of the damper hinge, $\mathbf{D}^{(m)}$, with respect to the lead-lag hinge in this frame of reference results to be:

$$\mathbf{D}^{(m)} = \begin{pmatrix} x_D \\ y_D \\ 0 \end{pmatrix} \tag{4.34}$$

- The position of the extremity of the rod that connects to blade $m-1$, the previous blade considering counter-clockwise succession, identified as $\mathbf{R}^{(m)}$, its position with respect to the damper position in the blade local reference frame is:

$$\mathbf{R}^{(m)} = \begin{pmatrix} x_R \\ y_R \\ 0 \end{pmatrix} \tag{4.35}$$

The position of the extremity of the rod that connects the damper to the next blade $m+1$, $\mathbf{A}^{(m)}$, can be expressed from the damper position, in the blade local reference frame:

$$\mathbf{A}^{(m)} = \begin{pmatrix} x_A \\ y_A \\ 0 \end{pmatrix} \tag{4.36}$$

Kinematic relations can be derived to determine the distance between points $\mathbf{A}^{(m)}$ and $\mathbf{R}^{(m)}$, the length of the rod results to be $\ell = 0.2459$ m.

The kinematic model with all the relevant points listed before is represented in Fig. 4.2.1

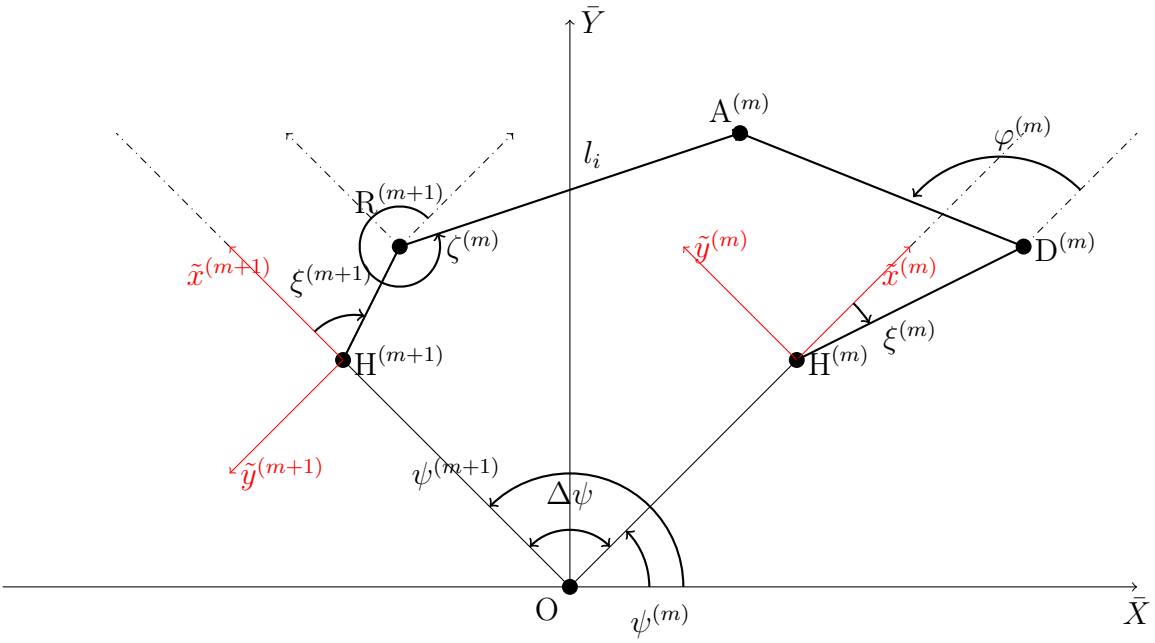

The point O denotes the center of the hub, while the angle $\Delta\psi$ defines the angular spacing between adjacent blades, where $\Delta\psi = 2\pi/N_b$.

For each blade, the key geometrical points are highlighted in bold and represent the vertices of the associated kinematic chain. The kinematic relationship linking the orientation of the damper arm $\zeta^{(m)}$ and its effective length l_i is established; solving this relationship provides the connection between the blade's azimuthal position and the damper's relative rotation.

These kinematic relations are obtained through the closure equation formed by the loop connecting the sequence of points O,$H^{(m)}$, $D^{(m)}$, $A^{(m)}$, $R^{(m+1)}$, and $H^{(m+1)}$. The formulation of these relationships is conveniently carried out in the local blade reference frame and subsequently projected into the global coordinate system.

$$\overline{\mathbf{OH}^{(m)}} + \overline{\mathbf{H}^{(m)}\mathbf{D}^{(m)}} + \overline{\mathbf{D}^{(m)}\mathbf{A}^{(m)}} = \overline{\mathbf{OH}^{(m+1)}} + \overline{\mathbf{H}^{(m+1)}\mathbf{R}^{(m+1)}} + \overline{\mathbf{R}^{(m+1)}\mathbf{A}^{(m)}} \tag{4.37}$$

The complex form of the closure equation will have the following expression:

$$\begin{aligned}(x_{\mathrm{H}} + \mathrm{j}y_{\mathrm{H}})\mathrm{e}^{\mathrm{j}\Delta\psi} + (x_{\mathrm{R}} + \mathrm{j}y_{\mathrm{R}})\mathrm{e}^{\mathrm{j}(\Delta\psi+\xi^{(m+1)})} + \ell\mathrm{e}^{\mathrm{j}(\Delta\psi+\xi^{(m+1)}+\zeta^{(m)})} \\ - \Big((x_{\mathrm{H}} + \mathrm{j}y_{\mathrm{H}}) + (x_{\mathrm{D}} + \mathrm{j}y_{\mathrm{D}})\mathrm{e}^{\mathrm{j}\xi^{(m)}} + d\mathrm{e}^{\mathrm{j}(\xi^{(m)}+\varphi^{(m)})}\Big) = 0\end{aligned} \tag{4.38}$$

By separating real and imaginary part of Eq. 4.38 two real scalar equations are obtained,

$$
\begin{aligned}
& x_{\mathrm{H}} \cos\Delta\psi - y_{\mathrm{H}} \sin\Delta\psi \\
+ x_{\mathrm{R}} \cos(\Delta\psi + \xi^{(m+1)}) - y_{\mathrm{R}} \sin(\Delta\psi + \xi^{(m+1)}) + \ell \cos(\Delta\psi + \xi^{(m+1)} + \zeta^{(m)}) \\
- x_{\mathrm{H}} - x_{\mathrm{D}} \cos\xi^{(m)} + y_{\mathrm{D}} \sin\xi^{(m)} - d\cos(\xi^{(m)} + \varphi^{(m)}) = 0 \quad (4.39a) \\
& x_{\mathrm{H}} \sin\Delta\psi + y_{\mathrm{H}} \cos\Delta\psi \\
+ x_{\mathrm{R}} \sin(\Delta\psi + \xi^{(m+1)}) + y_{\mathrm{R}} \cos(\Delta\psi + \xi^{(m+1)}) + \ell \sin(\Delta\psi + \xi^{(m+1)} + \zeta^{(m)}) \\
y_{\mathrm{H}} - x_{\mathrm{D}} \sin\xi^{(m)} - y_{\mathrm{D}} \cos\xi^{(m)} - d\sin(\xi^{(m)} + \varphi^{(m)}) = 0 \quad (4.39b)
\end{aligned}
$$

which can be solved numerically for given values of the blade angles, $\xi^{(m)}$ and $\xi^{(m+1)}$. Starting from the reference condition, null lead-lag angles, a value for $\varphi^{(m)}$ and $\zeta^{(m)}$ can be found.

From the computation of the time derivative of the closure equation, the matrices that link the blade lead-lag angles to the relative damper angles can be obtained:

$$
\boldsymbol{\phi}_{/\boldsymbol{\xi}} = \begin{bmatrix} \phi_{1/\xi^{(m)}} & \phi_{1/\xi^{(m+1)}} \\ \phi_{2/\xi^{(m)}} & \phi_{2/\xi^{(m+1)}} \end{bmatrix} \tag{4.40}
$$

The first row represents the Re part of the closure equation, while the second row stands for the Im.
The matrix related to the internal coordinates:

$$
\boldsymbol{\phi}_{/\mathrm{x_d}} = \begin{bmatrix} \phi_{1/\varphi^{(m)}} & \phi_{1/\zeta^{(m)}} \\ \phi_{2/\varphi^{(m)}} & \phi_{2/\zeta^{(m)}} \end{bmatrix} \tag{4.41}
$$

From the derivation of the closure equation, the following system is obtained:

$$
\boldsymbol{\phi}_{/\boldsymbol{\xi}} \left\{ \begin{array}{c} \dot{\xi}^{(m)} \\ \dot{\xi}^{(m+1)} \end{array} \right\} + \boldsymbol{\phi}_{/\mathbf{x}_d} \left\{ \begin{array}{c} \dot{\varphi}^{(m)} \\ \dot{\zeta}^{(m)} \end{array} \right\} = \mathbf{0} \tag{4.42}
$$

So the term $\boldsymbol{\Psi}_{\varphi}$ that relates the relative damper angles to the lag $\xi^{(m)}$ and $\xi^{(m+1)}$ can be computed, this term will be used to transform the damping and stiffness matrix from the damper relative coordinate to the lag ones.

Considering the five-blade configuration, the general form of the global problem involves five closure equations, one for each damper. Each closure equation can be formally expressed as a function of the five lag angles. In the following expression, the first subscript

denotes the index n of the closure equation (with $n = 1, \dots, 5$), while the second subscript indicates whether the real or imaginary part of the equation is considered, the subscript 1 stands for the real part, while the subscript 2 for the imaginary part.

$$
\begin{bmatrix}
\phi_{1_1/\xi^{(1)}} & \phi_{1_1/\xi^{(2)}} & 0 & 0 & 0 \\
\phi_{1_2/\xi^{(1)}} & \phi_{1_2/\xi^{(2)}} & 0 & 0 & 0 \\
0 & \phi_{2_1/\xi^{(2)}} & \phi_{2_1/\xi^{(3)}} & 0 & 0 \\
0 & \phi_{2_2/\xi^{(2)}} & \phi_{2_2/\xi^{(3)}} & 0 & 0 \\
0 & 0 & \phi_{3_1/\xi^{(3)}} & \phi_{3_1/\xi^{(4)}} & 0 \\
0 & 0 & \phi_{3_2/\xi^{(3)}} & \phi_{3_2/\xi^{(4)}} & 0 \\
0 & 0 & 0 & \phi_{4_1/\xi^{(5)}} & \phi_{4_1/\xi^{(5)}} \\
0 & 0 & 0 & \phi_{4_2/\xi^{(5)}} & \phi_{4_2/\xi^{(5)}} \\
\phi_{5_1/\xi^{(1)}} & 0 & 0 & 0 & \phi_{5_1/\xi^{(5)}} \\
\phi_{5_2/\xi^{(1)}} & 0 & 0 & 0 & \phi_{5_2/\xi^{(5)}}
\end{bmatrix}
\begin{Bmatrix}
\dot{\xi}^{(1)} \\ \dot{\xi}^{(2)} \\ \dot{\xi}^{(3)} \\ \dot{\xi}^{(4)} \\ \dot{\xi}^{(5)}
\end{Bmatrix} +
$$

$$
\begin{bmatrix}
\phi_{1_1/\varphi^{(1)}} & 0 & 0 & 0 & 0 & \phi_{1_1/\zeta^{(1)}} & 0 & 0 & 0 & 0 \\
\phi_{1_2/\varphi^{(1)}} & 0 & 0 & 0 & 0 & \phi_{1_2/\zeta^{(1)}} & 0 & 0 & 0 & 0 \\
0 & \phi_{2_1/\varphi^{(2)}} & 0 & 0 & 0 & 0 & \phi_{2_1/\zeta^{(2)}} & 0 & 0 & 0 \\
0 & \phi_{2_2/\varphi^{(2)}} & 0 & 0 & 0 & 0 & \phi_{2_2/\zeta^{(2)}} & 0 & 0 & 0 \\
0 & 0 & \phi_{3_1/\varphi^{(3)}} & 0 & 0 & 0 & 0 & \phi_{3_1/\zeta^{(3)}} & 0 & 0 \\
0 & 0 & \phi_{3_2/\varphi^{(3)}} & 0 & 0 & 0 & 0 & \phi_{3_2/\zeta^{(3)}} & 0 & 0 \\
0 & 0 & 0 & \phi_{4_1/\varphi^{(4)}} & 0 & 0 & 0 & 0 & \phi_{4_1/\zeta^{(4)}} & 0 \\
0 & 0 & 0 & \phi_{4_2/\varphi^{(4)}} & 0 & 0 & 0 & 0 & \phi_{4_2/\zeta^{(4)}} & 0 \\
0 & 0 & 0 & 0 & \phi_{5_1/\varphi^{(5)}} & 0 & 0 & 0 & 0 & \phi_{5_1/\zeta^{(5)}} \\
0 & 0 & 0 & 0 & \phi_{5_2/\varphi^{(5)}} & 0 & 0 & 0 & 0 & \phi_{5_2/\zeta^{(5)}}
\end{bmatrix}
\begin{Bmatrix}
\dot{\varphi}^{(1)} \\ \dot{\varphi}^{(2)} \\ \dot{\varphi}^{(3)} \\ \dot{\varphi}^{(4)} \\ \dot{\varphi}^{(5)} \\ \dot{\zeta}^{(1)} \\ \dot{\zeta}^{(2)} \\ \dot{\zeta}^{(3)} \\ \dot{\zeta}^{(4)} \\ \dot{\zeta}^{(5)}
\end{Bmatrix} = \mathbf{0} \tag{4.43}
$$

As showed in the geneal description of the method, § 4.1, the solution of the closure equation gives a direct link between the kinematic variables of the problem, $\boldsymbol{\xi}$, which are the lag angles $\xi^{(m)}$ and $\xi^{(m+1)}$ and the internal coordinates $\mathbf{x}_d$, the rod angle $\zeta^{(m)}$ and damper rotation $\varphi^{(m)}$, the other geometrical parameters are constant variables.

Matrix $\mathbf{C}_{\varphi x_d}$ extracts the relative rotations of the dampers, the internal kinematic variable of our interest in order to compute the moment acting on the blade, from the internal kinematic coordinates of the problems, its dimension will be (N_b, N_d), specifically for the problem consider, $(5, 10)$, the first (N_b, N_b) block will be an identity matrix, while the last block a zeros matrix.

$$
\dot{\boldsymbol{\varphi}} = -\mathbf{C}_{\varphi x_d} \boldsymbol{\phi}_{x_d}^{-1} \boldsymbol{\phi}_{\xi} \dot{\boldsymbol{\xi}} \tag{4.44}
$$

So matrix Ψ_{φ} can be defined as:

$$
\dot{\boldsymbol{\varphi}} = \Psi_{\varphi} \dot{\boldsymbol{\xi}} \tag{4.45}
$$

The matrix of stiffness and damping can be transformed, leading to the their expression as function of the lag angles, similarly a more general expression of the stiffness and damping matrix can be obtained considering the other viscolelastic joints along the damper path, between the hub and the link, and between the damper and the link.

For each joint, the relative contribution to the global stiffness can be expressed by exploiting the PVW formulation:

$$\delta\boldsymbol{\xi}^T\mathbf{K}_\xi\boldsymbol{\xi} = \delta\boldsymbol{\xi}^T\mathbf{K}_\mathrm{H}\boldsymbol{\xi} + \delta\boldsymbol{\zeta}^T\mathbf{K}_\mathrm{R}\boldsymbol{\zeta} + \delta\boldsymbol{\eta}^T\mathbf{K}_\mathrm{A}\boldsymbol{\eta} + \delta\boldsymbol{\varphi}^T\mathbf{K}_\varphi\boldsymbol{\varphi} \tag{4.46}$$

An analogous holds for the damping matrix:

$$\delta\boldsymbol{\xi}^T\mathbf{C}_\xi\dot{\boldsymbol{\xi}} = \delta\boldsymbol{\xi}^T\mathbf{C}_\mathrm{H}\dot{\boldsymbol{\xi}} + \delta\boldsymbol{\zeta}^T\mathbf{C}_\mathrm{R}\dot{\boldsymbol{\zeta}} + \delta\boldsymbol{\eta}^T\mathbf{C}_\mathrm{A}\dot{\boldsymbol{\eta}} + \delta\boldsymbol{\varphi}^T\mathbf{C}_\varphi\dot{\boldsymbol{\varphi}} \tag{4.47}$$

The relative rotations φ and ζ are already defined as internal kinematic coordinates of the problem and have therefore been computed from the closure equations. In contrast, the rotation $\eta^{(m)}$ can be expressed as a function of the other two, according to: $\eta^{(m)} = \varphi^{(m)} - \zeta^{(m)} - \Delta\psi$.

As done for the relative rotation of the damper φ, the other relative rotations of the joints, since they are all expressed as function of the internal kinematic variables $\mathbf{x}_d$, can be easily obtained via their respective extraction matrix: $\mathbf{C}_{\varphi x_d}, \mathbf{C}_{\eta x_d}, \mathbf{C}_{\zeta x_d}$.

So the expression of the stiffness and damping matrix as function of the relative rotation each damper finally becomes:

$$\mathbf{K}_\xi = \Psi_\varphi^T\mathbf{K}_\varphi\Psi_\varphi + \Psi_\eta^T\mathbf{K}_\mathrm{A}\Psi_\eta + \Psi_\zeta^T\mathbf{K}_\mathrm{R}\Psi_\zeta + \mathbf{K}_\mathrm{H} \tag{4.48}$$

$$\mathbf{C}_\xi = \Psi_\varphi^T\mathbf{C}_\varphi\Psi_\varphi + \Psi_\eta^T\mathbf{C}_\mathrm{A}\Psi_\eta + \Psi_\zeta^T\mathbf{C}_\mathrm{R}\Psi_\zeta + \mathbf{C}_\mathrm{H} \tag{4.49}$$

Due to symmetry considerations, since the rotor can be considered isotropic with the same geometrical properties for all the dampers and blades, the terms that relate the relative angle φ to the lag angles $\boldsymbol{\xi}$ result in being the same for all the closure equations.

Considering only the first closure equation, that relates the first damper $\varphi^{(1)}$ to blade 1 and blade 2:

$$\dot{\varphi}^{(1)} = \begin{bmatrix}\Psi_{\varphi 1} & \Psi_{\varphi 2}\end{bmatrix}\begin{Bmatrix}\dot{\xi}^1\\ \dot{\xi}^2\end{Bmatrix} \tag{4.50}$$

Analogous considerations can be done for the extraction matrix of the other rotations of

the viscoelastic joints.

The data used for modeling the IB kinematics, representative of a generic medium-weight helicopter, are reported in Table 4.1.

Table 4.1: Model Parameters.

Parameter	**Value**	**Units**
Number of blades, N_b	5	–
Blade mass, m_b	75.	kg
Blade mass static moment, S_ξ	115	kg m
Blade mass moment of inertia, I_ξ	400.	kg m^2
Lag hinge offset, e	0.25	m
Lag spring, K_φ	18000.	N m rad^{-1}
Lag damper, C_φ	2200.	N m s rad^{-1}
Horizontal Lag Hinge offset, x_H	0.250	m
Vertical Lag Hinge offset, y_H	0	m
Horizontal Rod end, blade m+1, x_R	0.100	m
Vertical Rod end, blade m+1,y_R	-0.100	m
Horizontal Damper position, x_D	0.150	m
Vertical Damper position, y_D	0.030	m
Horizontal Rod end, blade m, x_A	0.200	m
Vertical Rod end, blade m, y_A	0.200	m
Rod length, ℓ	0.246	m
Transmission ratio, Ψ_φ	[-1.5045 , 0.6320]	–

4.2.2. Isolated Rotor Analysis

To advance beyond the Hammond model's idealized framework—which restricts hub motion to generalized in-plane displacements—this analysis incorporates realistic rotor properties. By leveraging the previously derived relationship between the rotational damper's relative angle and the blade's lead-lag angles, isolated systems, and subsequently the coupled GR problem, can now be evaluated using physical rotational dampers rather than simplified theoretical analogs.

The initial isolated rotor analysis was carried out to assess the damping present in the various multiblade modes of the initial IB model. These values were then used as a basis for comparison between different damper architectures and to evaluate different damper configurations. The goal was to determine, for the same damping on the MBC modes, what damper characteristics were required.

The stiffness and damping matrices can be written as functions of the blade lead-lag

angles by using the relations in Eq.(4.45), as shown in Eq.(4.48) and Eq. (4.49).

Once all the problem matrices have been transformed into the blade coordinate system, the multiblade coordinate formalism can be applied, as shown in § 2.3, for a five-blade rotor, this involves defining five multiblade coordinates: collective coordinate ξ_0, the first pair of cyclic coordinates ξ_{1c} and ξ_{1s}, and the second pair of cyclic coordinates ξ_{2c} and ξ_{2s}.

Using this approach, the blade equations of motion—excluding the airframe dynamics—can be expressed as

$$\mathbf{M}_b\ddot{\mathbf{q}}_b + \mathbf{C}_b\dot{\mathbf{q}}_b + \mathbf{K}_b\mathbf{q}_b = \mathbf{0} \tag{4.51}$$

It can be observed that since there is no airframe, there cannot be coupling between multiblade modes and airframe modes.

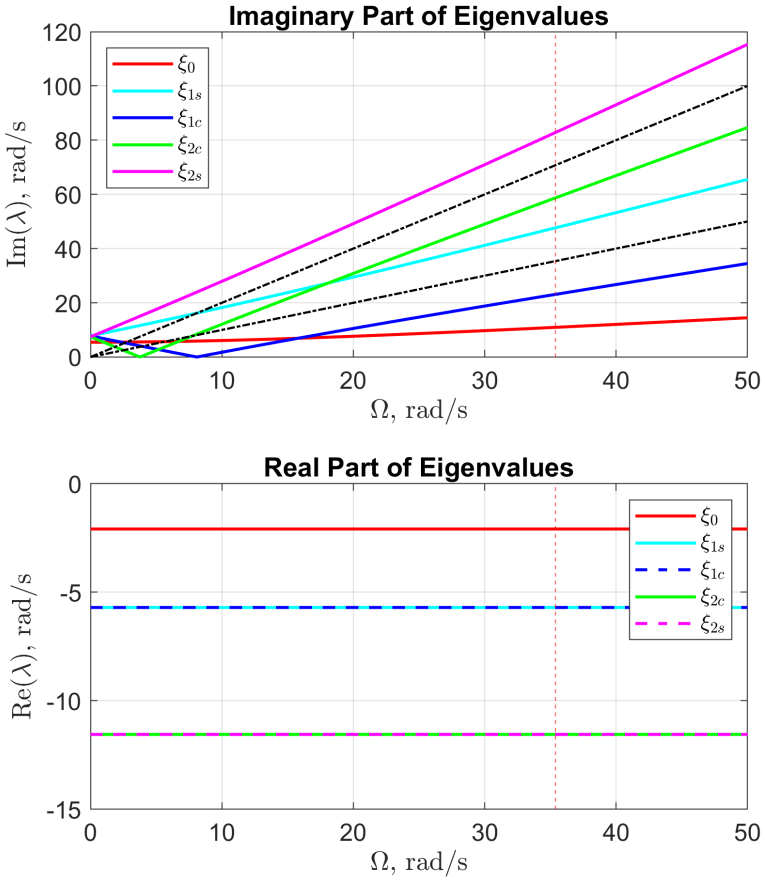

Figure 4.1: Isolated rotor eigenvalues of the GR problem.

The results reveal the presence of three distinct modal families: the collective mode ξ_0,

the first cyclic pair ξ_{1_c} and ξ_{1_s} (mutually coincident), and the second cyclic pair ξ_{2_c} and ξ_{2_s}, which are also coincident. As expected, in the absence of an airframe, no coupling between the modes is observed, and no instability arises.

In terms of frequency behavior, the progressive and regressive components of each modal pair can be identified by analyzing the lag frequency, given by:

$$\nu_\xi = \sqrt{e\frac{S_\xi}{I_\xi} + \frac{K_\xi}{\Omega^2 I_\xi}}, \tag{4.52}$$

where the contribution of the lag stiffness arises from the spring component of the damper system. The modal frequencies can thus be interpreted in terms of the sum and difference between the rotor speed ω and the natural lag frequency ω_ξ, corresponding respectively to the progressive mode $(\omega + \omega_\xi)$ and the regressive mode $(\omega - \omega_\xi)$.

4.2.3. Rotor Coupled with Airframe Analysis

The airframe in-plane displacements, x and y, are represented as a linear combination of six rigid-body modes, offering a more comprehensive model compared to the simplified two-mode representation adopted by Hammond. This formulation enables the individual assessment of each airframe mode evolution, rather than restricting the analysis to only the two principal in-plane modes.

The position of the hub center can be expressed as

$$\mathbf{q}_a = \begin{Bmatrix} x \\ y \end{Bmatrix} = \mathbf{U}\mathbf{q} \tag{4.53}$$

where the vector $\mathbf{q}$ collects the six modes: lateral, longitudinal, vertical, yaw, pitch, and roll of the airframe. The matrix $\mathbf{U}$ collects the in-plane component of these modes. Considering the presence of the airframe, the blade equations in blade coordinates have the same formulation of Eq. (2.5a).

The airframe equation has the same form as Eq. (2.5b), but the airframe matrices are written in order to take into account the modal mass, damping ratio, and frequency of each mode.

$$\mathbf{M}_a = \begin{bmatrix} m_\phi & \cdots & 0 \\ \vdots & \ddots & \vdots \\ 0 & \cdots & m_\phi \end{bmatrix} \tag{4.54}$$

where m_ϕ stands for the modal mass of mode ϕ.

$$\mathbf{C}_a = \begin{bmatrix} \zeta_1 \cdot \omega_1 & 0 & \cdots & 0 \\ 0 & \zeta_2 \cdot \omega_2 & \cdots & 0 \\ \vdots & \vdots & \ddots & \vdots \\ 0 & 0 & \cdots & \zeta_n \cdot \omega_n \end{bmatrix} \tag{4.55}$$

where ζ_i stands for the damping coefficient of the ith mode, with frequency ω_i.

$$\mathbf{K}_a = \begin{bmatrix} \omega_1^2 & 0 & \cdots & 0 \\ 0 & \omega_2^2 & \cdots & 0 \\ \vdots & \vdots & \ddots & \vdots \\ 0 & 0 & \cdots & \omega_n^2 \end{bmatrix} \tag{4.56}$$

The damping and frequency values of the different airframe modes are reported in Table 4.2.

Table 4.2: Frequency and damping values for the airframe modes of a generic medium-weight helicopter.

Mode	$\boldsymbol{\omega}$	$\boldsymbol{\zeta}$	**x**	**y**
Lat.	1.50	0.0750	0.0000E+00	2.0000E-02
Long.	2.20	0.0750	2.0000E-02	0.0000E-03
Yaw	2.40	0.0750	0.0000E+00	1.0000E-02
Vert.	3.70	0.0750	0.0000E-03	0.0000E-04
Pitch	4.60	0.0750	-2.0000E-02	0.0000E-04
Roll	5.00	0.0750	0.0000E-04	2.2000E-02

The final coupled system, considering all five multiblade coordinates, plus the airframe in-plane movement, given by the six mode shapes, results in an $(N_b + N_\phi)$ system, but the only coupled portion is still the one related to the 1st cyclic.

The resultant matrix of the global system has the following form

$$\mathbf{M} = \begin{bmatrix} \mathbf{M}_{\text{bmb}} & \mathbf{T}^T(\mathbf{S}_b\mathbf{U}) \\ (\mathbf{S}_b\mathbf{U})^T\mathbf{T} & \mathbf{M}_a \end{bmatrix} \tag{4.57}$$

$$\mathbf{C} = \begin{bmatrix} \mathbf{C}_{\text{bmb}} & \mathbf{0}_{N_b \times N_\phi} \\ \mathbf{0}_{N_\phi \times N_b} & \mathbf{C}_a \end{bmatrix} \tag{4.58}$$

$$\mathbf{K} = \begin{bmatrix} \mathbf{K}_{\text{bmb}} & \mathbf{0}_{N_b \times N_\phi} \\ \mathbf{0}_{N_\phi \times N_b} & \mathbf{K}_a \end{bmatrix} \tag{4.59}$$

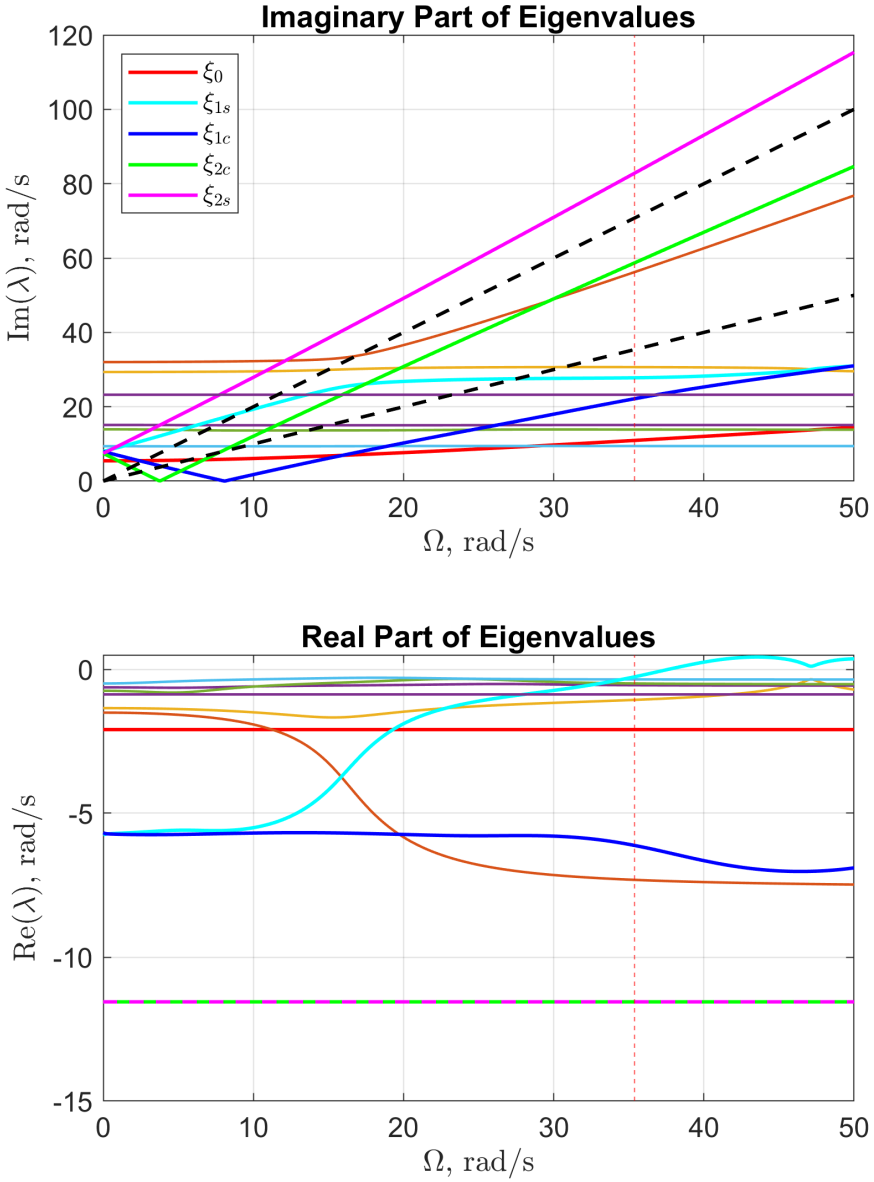

Figure 4.2: Rotor + Airframe real and imaginary part of eigenvalues of GR problem.

The multiblade modes are reported in the legend and are highlighted using a thicker line. It can be observed that the collective and second cyclic modes remains unaltered if compared with Fig. 4.1, as there is no interaction with the motion of the airframe horizontal lines at $\mathrm{Re}(\lambda) \approx -2$, rad/s for ξ_0 and $\mathrm{Re}(\lambda) \approx -11$, rad/s for ξ_{2_c} and ξ_{2_s} .

Some airframe mode shapes interact more with the rotor degrees of freedom, and their evolution can be seen, while others are less coupled and remain unaltered. Nonetheless, the interaction between the ξ_{1_s} mode and the pitch and roll airframe modes results in an instability.

A zoom of the Real part of the eigenvalues of Fig. 4.2 is presented in Fig. 4.3.

The bubble of instability can clearly be seen as it appears slightly above the nominal RPM, the interaction between the ξ_{1_s} mode (cyan) and the roll mode (yellow) can clearly be observed.

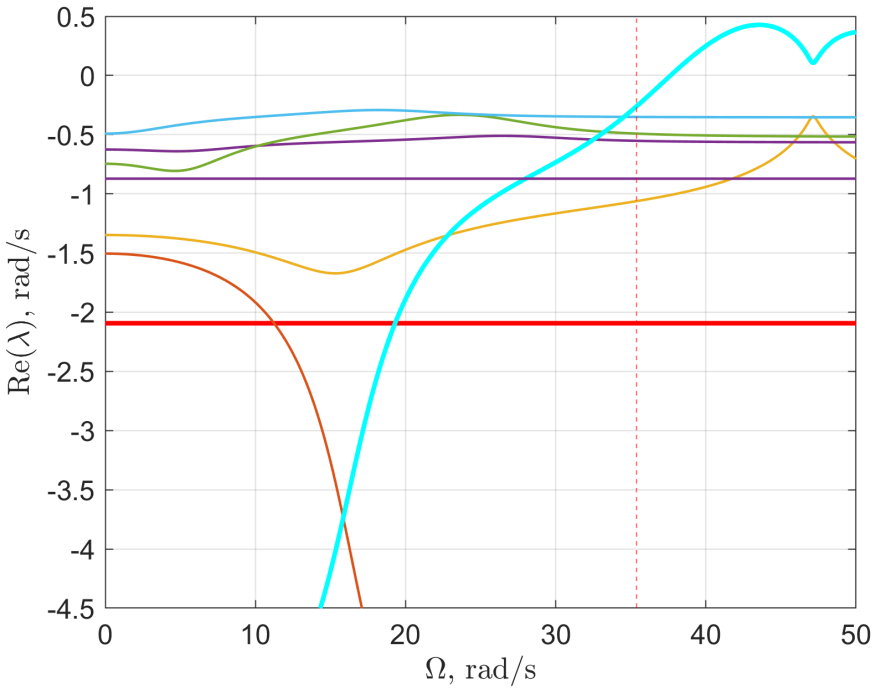

Figure 4.3: Zoom of Re of eigenvalues of Fig. 4.2, for IB

.

4.2.4. Application of the Sensitivity Problem to the Stiffness and Damping Terms

Similarly to the approach employed for the I2B problem in Chapter 3, the evolution of the critical eigenvalue, ξ_{1_s}—identified as critical since it becomes unstable after coupling with

the airframe—can be analyzed in terms of its sensitivity to the stiffness and damping of the joints. This analysis provides insight into whether increasing the stiffness/ damping results in a stabilizing or destabilizing effect on the system, and on which joint is more convenient to act.

Due to the linearity of the problem, each contribute of the stiffness $\mathbf{K}_{\mathrm{A}}, \mathbf{K}_{\mathrm{R}}, \mathbf{K}_{\mathrm{H}}$ and damping can be investigated separately.

Considering only the eigenvalue ξ_{1s}, its portion of the problem can be extracted from the GR sensitivity equations, Eqs. (3.36).

The derivatives of the mass and damping matrices with respect to the stiffness parameters are zero, whereas the derivative of the stiffness matrix includes non-zero terms. In contrast, when differentiating with respect to the damping parameters, only the stiffness and damping matrices contribute non-zero terms.

The derivatives are initially computed with respect to the relative joint rotations. Subsequently, by applying the coordinate transformation derived from the solution of the closure equations, they are expressed in the lead-lag coordinate system.

The derivative of the stiffness matrix can be expressed as

$$\mathbf{K}_{\xi} = \Psi_{\varphi}^{T}\mathbf{K}_{\varphi}\Psi_{\varphi} + \Psi_{\eta}^{T}\mathbf{K}_{\mathrm{A}}\Psi_{\eta} + \Psi_{\zeta}^{T}\mathbf{K}_{\mathrm{R}}\Psi_{\zeta} + \mathbf{K}_{\mathrm{H}}, \tag{4.60}$$

where the derivative respect K_{ζ}

$$\mathbf{K}_{\xi/K_{\zeta}} = \Psi_{\zeta}^{T}\mathbf{K}_{\mathrm{R}/K_{\zeta}}\Psi_{\zeta}, \tag{4.61}$$

respect K_{η}

$$\mathbf{K}_{\xi/K_{\eta}} = \Psi_{\eta}^{T}\mathbf{K}_{\mathrm{A}/K_{\eta}}\Psi_{\eta}, \tag{4.62}$$

respect K_{H}

$$\mathbf{K}_{\xi/K_{\mathrm{H}}} = \mathbf{K}_{\mathrm{H}/K_{\mathrm{H}}}. \tag{4.63}$$

Starting from this expression, the derivative of the global stiffness matrix for the entire system—comprising the blade in multiblade coordinates and the airframe with its six degrees of freedom—can be obtained.

Instead, considering the derivative of the damping terms, non-null contributions will also appear in the stiffness matrix expression in multiblade coordinates:

$$\mathbf{C}_\xi = \Psi_\varphi^T \mathbf{C}_\varphi \Psi_\varphi + \Psi_\eta^T \mathbf{C}_\mathrm{A} \Psi_\eta + \Psi_\zeta^T \mathbf{C}_\mathrm{R} \Psi_\zeta + \mathbf{C}_\mathrm{H}, \tag{4.64}$$

where derivative respect C_ζ

$$\mathbf{C}_{\xi/C_\zeta} = \Psi_\zeta^T \mathbf{C}_{\mathrm{R}/C_\zeta} \Psi_\zeta, \tag{4.65}$$

respect C_η

$$\mathbf{C}_{\xi/C_\eta} = \Psi_\eta^T \mathbf{C}_{\mathrm{A}/C_\eta} \Psi_\eta, \tag{4.66}$$

respect C_H

$$\mathbf{C}_{\xi/C_\mathrm{H}} = \mathbf{C}_{\mathrm{H}/C_\mathrm{H}}. \tag{4.67}$$

Since $\mathbf{K}_b$ is converted into MBC as follows:

$$\mathbf{K}_b = \mathbf{T}^T (\mathbf{K}_\xi \mathbf{T} + \mathbf{C}_\xi \dot{\mathbf{T}} + \mathbf{M}_\xi \ddot{\mathbf{T}}) \tag{4.68}$$

Also, the derivatives of the damping matrix, in non-rotating coordinates, will have non-null contributions with respect to the damping of the different joints.

As Ω increases, in order to ensure that the eigenvalue of the first cyclic progressive mode continues to be tracked, the sensitivity of the eigenvalue and its eigenvector with respect to the angular velocity must also be evaluated, similarly to what done in Chapter 3, its evolution is reported in Fig. 4.4.

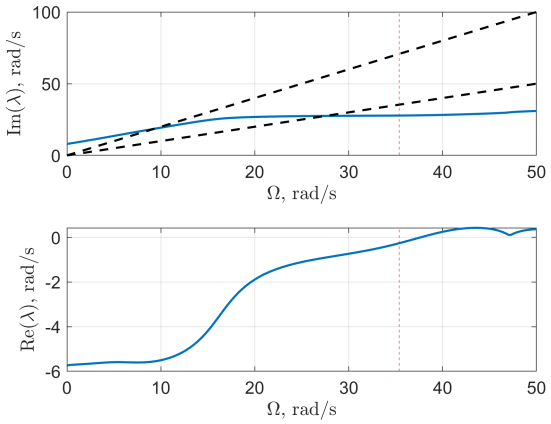

Figure 4.4: Evolution of critical eigenvalue vs Ω.

Regarding the sensitivity of this eigenvalue to the stiffness terms of the joints:

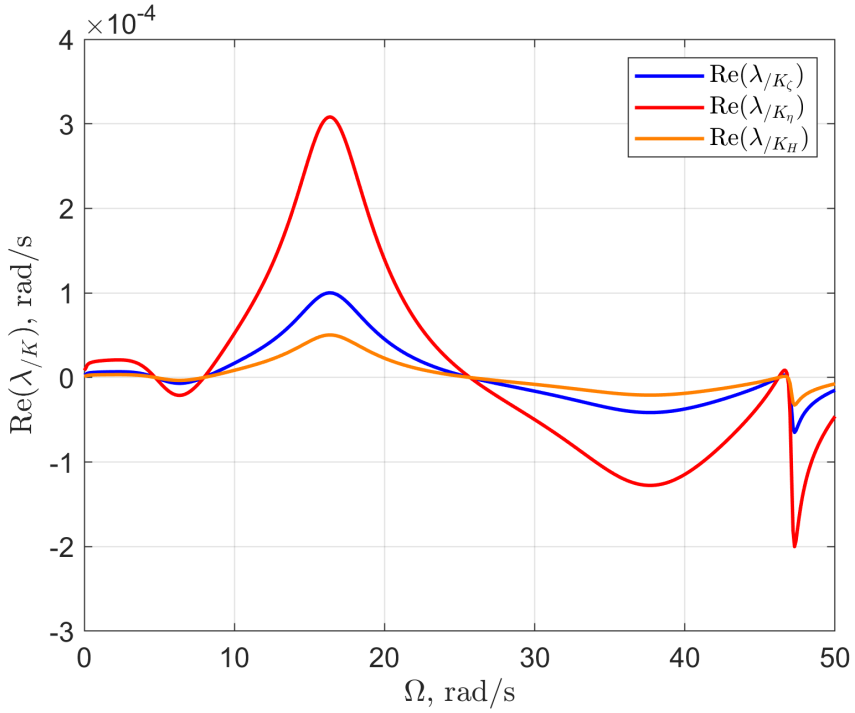

Figure 4.5: Real part of sensitivity of the critical eigenvalue to the stiffness terms K_ζ,K_η, K_H.

All three plots show similar trends: an initial phase where a destabilizing contribution is present (since Re(λ) is positive), followed by a stabilizing contribution at high RPM. This could be helpful in order to stabilize the eigenvalue since the instability appears at high RPM.

Considering instead the magnitude of the derivative, its value is meaningful. A variation of 1 in K, which is in N·m rad^{-1}, implies a change in the eigenvalue on the order of 1×10^{-4} up to 3×10^{-4} rad/s. Given that the stiffness values can easily reach thousands, strong variations in the eigenvalue can be achieved.

Instead, the results regarding the sensitivity of the critical eigenvalue to the damping terms of the joints are reported in Fig. 4.6.

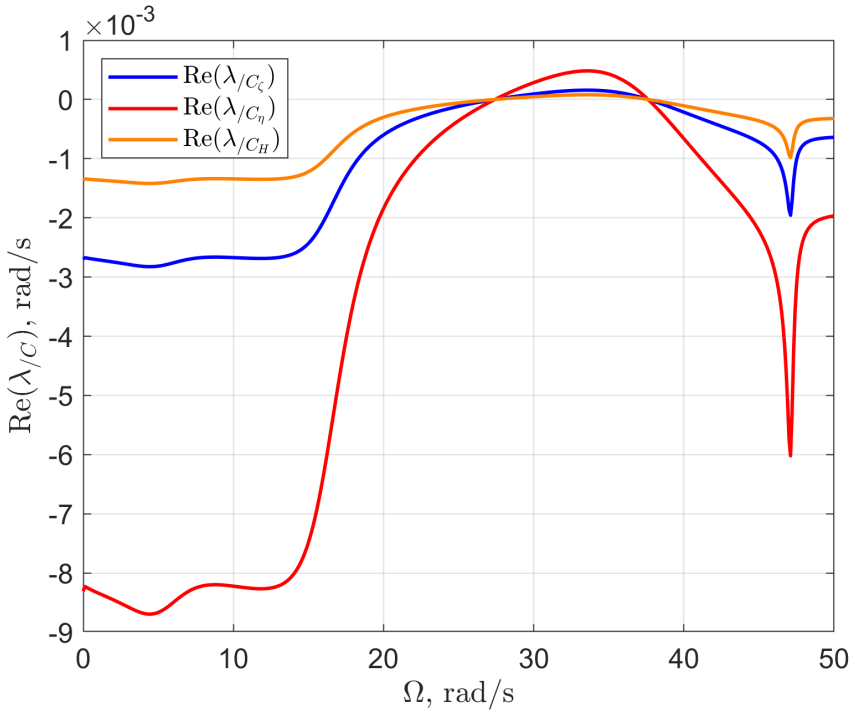

Figure 4.6: Real part of sensitivity of the critical eigenvalue to the damping terms C_ζ,C_η, C_H

Similarly to the analysis of the damping terms, all three joints exhibit a comparable impact on the critical eigenvalue. In terms of magnitude, the damping coefficients influence the real part of the eigenvalue approximately one order of magnitude more than the corresponding stiffness terms. Generally, across the entire RPM range, an increase in the damping coefficients contributes to a stabilizing effect on the critical eigenvalue, thus having a beneficial impact on the overall stability of the system.

To confirm the correctness of the applied method, (as done in Appendix B), a comparison has been performed between the eigenvalues computed by solving the second-order system after a perturbation of the stiffness and damping terms and those obtained through the sensitivity analysis.

Separately, a perturbation of 2700 Nm/rad was imposed on K_ζ, K_η, and K_H. Then, the difference between the results obtained through sensitivity analysis and those computed by solving the eigenvalue problem after perturbing the stiffness term of the joint was evaluated.

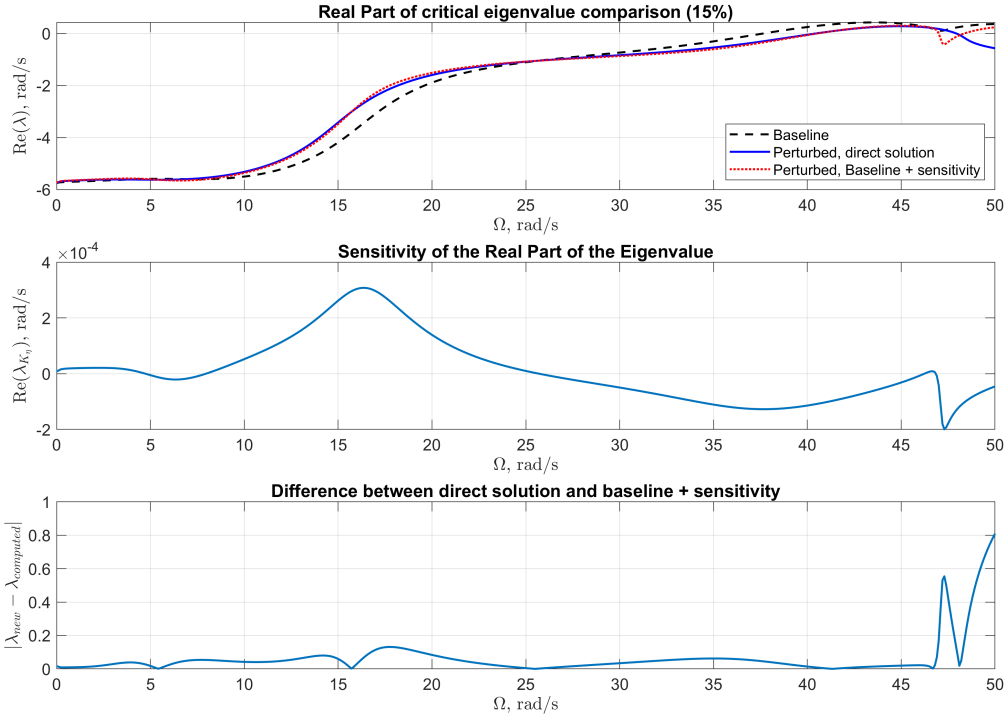

Figure 4.7: Sensitivity of the critical eig to K_η ($\Delta K = 15\%\ K_{\mathrm{d}_{\mathrm{nominal}}}$).

Although the large perturbation of 2700 Nm/rad, relative to the nominal value of 18000 Nm/rad, causes the instability bubble to nearly vanish, the discrepancy between the perturbed solution and the sum of the baseline solution and its sensitivity prediction remains significant.

Conversely, when a smaller perturbation is applied to the stiffness parameter (1% of the nominal K_d value), the change in the eigenvalue magnitude is reduced. In this case, the eigenvalue prediction obtained through sensitivity analysis closely matches the result from the direct computation, as illustrated in the Fig. 4.8.

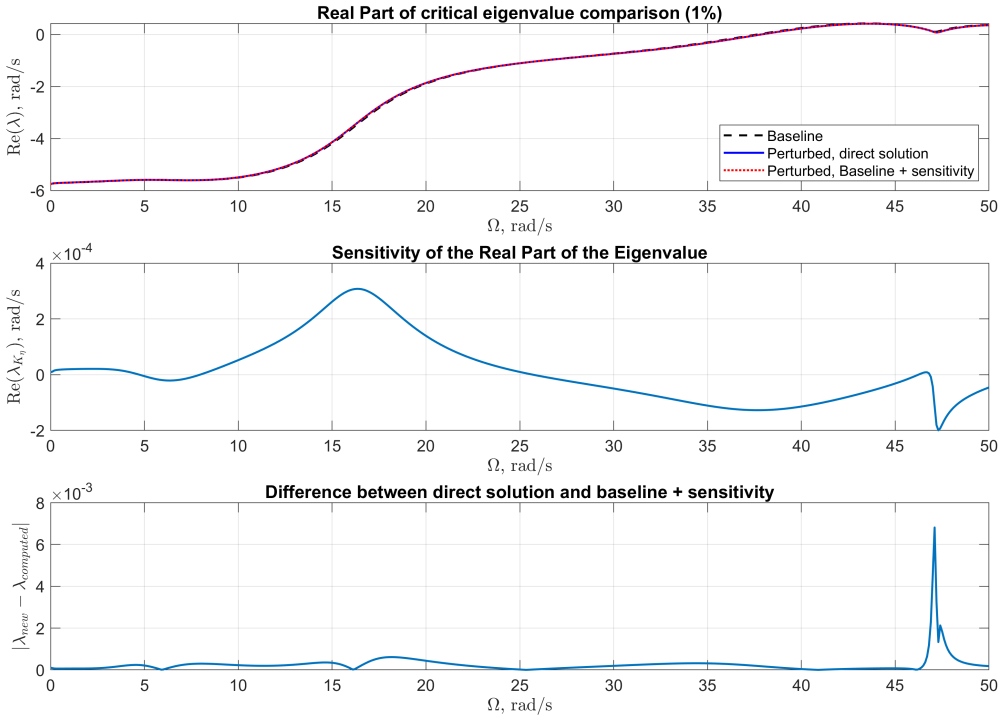

Figure 4.8: Sensitivity of the critical eig to K_η ($\Delta K = 1\%\ K_{\mathrm{d}_{\mathrm{nominal}}}$).

Similarly, the same approach was applied to the damping terms. Initially, a significant perturbation corresponding to 15% of the nominal damper value was imposed on the most sensitive joint, identified as C_η (see Fig. 4.6) in order to investigate whether the instability caused by the increase in damping could be mitigated, then a smaller perturbation of 1% of nominal C_d was applied, this allowed the identify how accurately the eigenvalue evolution could be tracked using the sensitivity approach.

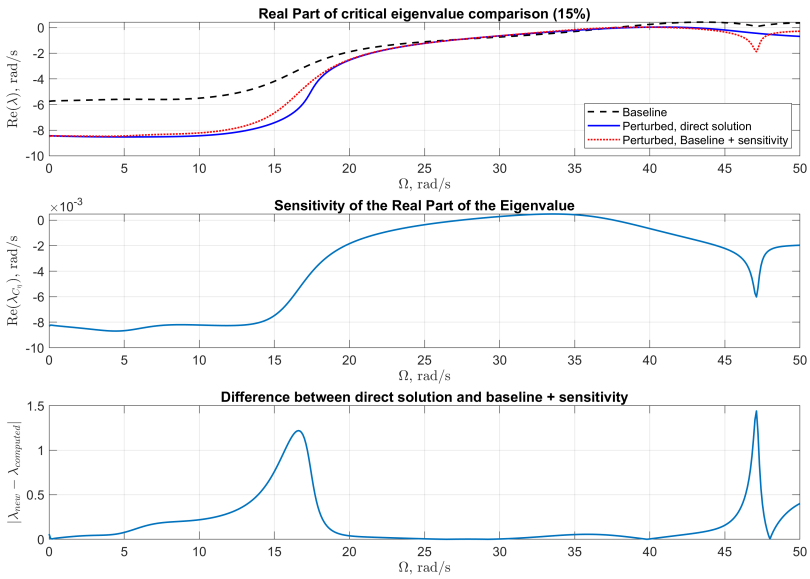

Figure 4.9: Sensitivity of the critical eig to C_η ($\Delta C = 15\%\ C_{\mathrm{d}_{\mathrm{nominal}}}$).

Compared to the perturbation imposed on the stiffness terms, a perturbation applied to the damping terms of the visco-elastic joint strongly affects the evolution of the eigenvalue, and it can be clearly observed how the instability disappears. Although the difference between the eigenvalue computed directly and that obtained through sensitivity significantly increases—especially in the region where the eigenvalue sensitivity exhibits a cusp, as shown in Fig. 4.6—the difference remains small in the other regions. This is further confirmed when a slight perturbation is applied to the stiffness terms, where differences are on the order of 1×10^{-3}, except near the cuspidal region.

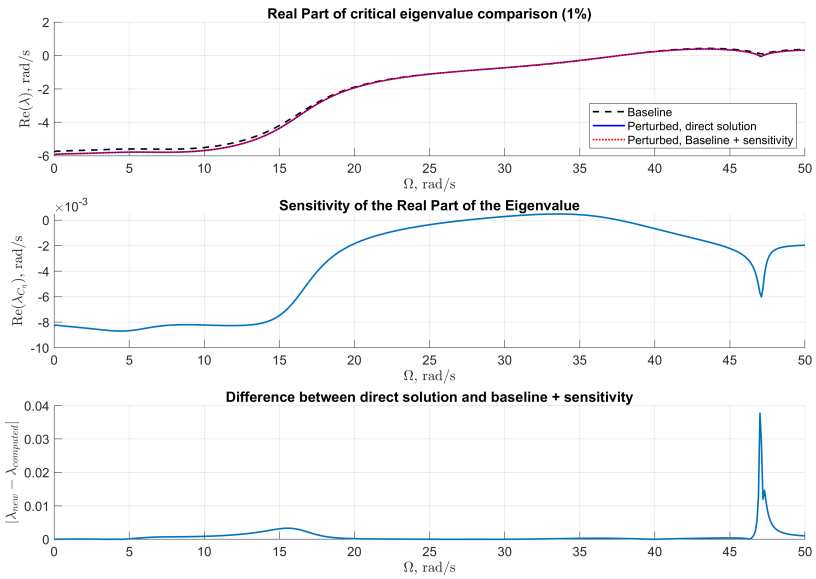

Figure 4.10: Sensitivity of the critical eig to C_η ($\Delta C = 1\%\ C_{\mathrm{d}_{\mathrm{nominal}}}$).

The remaining results for the perturbations of the stiffness and damping terms of the different joints are reported in Appendix B.

4.2.5. Equivalent Blade to Hub Damper Model

The general method introduced in § 4.1 is not limited by the specific damper arrangement of the rotor and can be extended to any possible configuration. In this section, it is applied to derive an equivalent BTH rotor model. The kinematics of this configuration are significantly simpler compared to the IB model, and the transformation matrix that relates the damper relative rotation to the lead-lag angles reduces to identity matrices, $\Psi_\varphi = \mathbf{I}$.

The key aspect in obtaining a comparable BTH model, suitable for direct comparison with the previously derived IB model, lies in the selection of the damper coefficients.

To determine these coefficients, the sensitivity of the eigenvalues with respect to the damper properties—C_d and K_d—as introduced in Chapter 3, is exploited. By tuning these parameters, it is possible to build a BTH rotor model that is dynamically equivalent to the IB model. The equivalence is achieved by adjusting the damper characteristics so that one of the primary cyclic modes involved in the GR problem matches both the frequency and damping of its counterpart in the IB configuration.

An iterative procedure exploiting the sensitivity of the first cyclic eigenvalue to the

damper's stiffness and damping terms is developed to determine the updated damper characteristics, and convergence is achieved for $K_{d,\mathrm{BTH}} = 37354.57\,\mathrm{Nm/rad}$ and damping $C_{d,\mathrm{BTH}} = 4565.60\,\mathrm{Nm{\cdot}s/rad}$.

In Fig. 4.13 is reported the solution of the blade equation, with no airframe, and it can be observed how the critical eigenvalue presents the same damping and frequency, at the nominal RPM, of the IB problem.

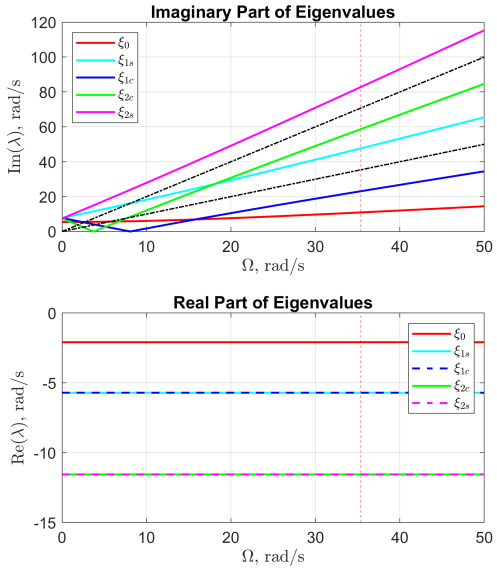

Figure 4.11: IB rotor model

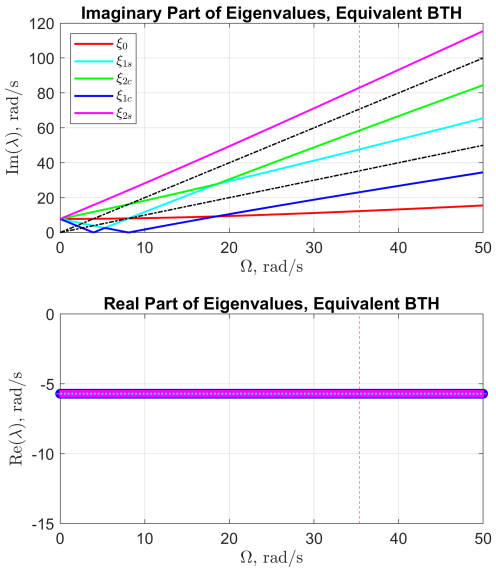

Figure 4.12: Equivalent BTH rotor model

Figure 4.13: Comparison between IB and equivalent BTH rotor models for isolated rotor analysis

In Fig. 4.13, it can be observed that the first cyclic modes exhibit the same imaginary and real parts as those of the IB isolated rotor analyzed at the nominal RPM, and therefore have identical frequencies and damping. Moreover, all the multiblade modes share the same real part, since the BTH damper formulation provides uniform damping across all modes.

4.3. Inter-2-Blade Model

Following the methodological approach established for the IB model in § 4.2, this section introduces a generalized description of the I2B configuration. The characterization incorporates multiple interdependent parameters, enabling both broad applicability across

operational contexts and enhanced problem space generalization through expanded degrees of freedom.

4.3.1. Geometry and Kinematic Model Definition

Considering an I2B setup with a rotational damper mounted on the root of blade $m+1$ and connected to blade m and $m+2$ by two rods.

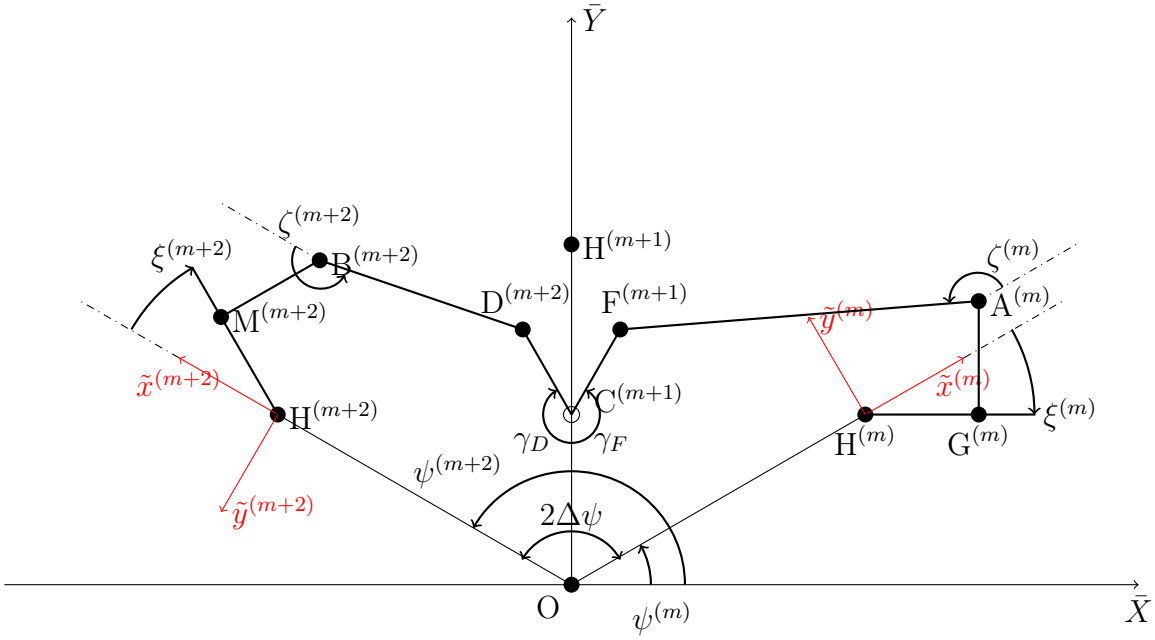

Recalling the geometry used in the IB scenario, the same value of lag hinge offset e, which lies along the x-direction, is adopted.

The length of the relevant geometrical parameters used in the problem is listed in Table 4.3:

Table 4.3: Geometrical Parameters I2B.

Parameter	Value	Expression
a	$\frac{e}{2}$	$\overline{\mathrm{G}^{(m)}\mathrm{A}^{(m)}}$
b	$\frac{e}{2}$	$\overline{\mathrm{M}^{(m+2)}\mathrm{B}^{(m+2)}}$
c_a	$\frac{e}{4}$	$\overline{\mathrm{H}^{(m)}\mathrm{G}^{(m)}}$
c_b	$\frac{e}{4}$	$\overline{\mathrm{H}^{(m+2)}\mathrm{M}^{(m+2)}}$
d	$\frac{e}{2}$	$\overline{\mathrm{C}^{(m+1)}\mathrm{D}^{(m+2)}}$
f	$\frac{e}{2}$	$\overline{\mathrm{C}^{(m+1)}\mathrm{F}^{(m+1)}}$
c_d	$\frac{e}{4}$	$\overline{\mathrm{OC}^{(m+1)}}$

As described in § 4.1 and performed in § 4.2, the development of the closure equations allows establishing the relationship between the kinematic variables, the lead-lag angles, and the internal variables of the system, namely the rod angles and the damper angles.

Initially, the lengths of the two rods were determined starting from a reference configuration. The reference condition chosen corresponds to the condition of zero lag, where the relative angle of the rod, denoted as $\zeta^{(m)}$, is set to 180 degrees. In this configuration, the rod is aligned parallel to the blade. By considering the other fixed geometric parameters and imposing the value of $\zeta^{(m)}$ through solving the closure equations under this reference condition, lead to a computed rod length ℓ equal to 0.1657 m.

Regarding the computation of the transmission ratios, unlike the IB problem, this scenario involves two distinct kinematic closure equations for each damper.

Considering the geometry of the I2B scheme, Fig. 4.3.1, the unknown is the relative rotation of the damper $\varphi^{(m+1)}$, which is given by the sum of two independent terms; the first, γ_F, is related to the mth blade, the second, γ_D, is related to the $(m+2)$th blade. Since the rotational damper is attached to the root of the $(m+1)$th blade, it is not subjected to the lag angle $\xi^{(m+1)}$. So the independent variables of the problems are the lag angles $\xi^{(m)}$ and $\xi^{(m+2)}$, similarly to the IB problem, two internal kinematic variables $\mathbf{x}_d$ can be written. The first, $\zeta^{(m)}$ is relative rotation of the rod of blade $\xi^{(m)}$, the second, $\zeta^{(m+2)}$, is the relative rotation of the rod for the half related to blade $m+2$.

The kinematic relationship that links the relative damper angle φ and the lag angles $\xi^{(m)}$ and $\xi^{(m+2)}$, can be obtained by developing two different closure equations.

The first is related to the right half of the model, and is represented by the figure of vertices: O, $\mathrm{H}^{(m)}$, $\mathrm{G}^{(m)}$, $\mathrm{A}^{(m)}$, $\mathrm{F}^{(m)}$ and $\mathrm{C}^{(m+1)}$.

- Hinge position on blade mth, considering the offset in $\bar{X}$ and $\bar{Y}$ direction equal to the IB problem, (y_H will be considered non-null later for the tuning of the I2B geometry):

$$p_{\mathrm{H}}^{(m)} = (x_{\mathrm{H}} + \mathrm{j}y_{\mathrm{H}})\mathrm{e}^{\mathrm{j}\psi^{(m)}} \tag{4.69}$$

- Extremity of the rod close to blade m, presents an offset both in the $\tilde{x}$ direction and $\tilde{y}$ of blade's local frame of reference, the offset along the blade is represented by c_a while chordwise offset is given by a:

$$p_{\mathrm{A}}^{(m)} = p_{\mathrm{H}}^{(m)} + (c_a + \mathrm{j}a)\mathrm{e}^{\mathrm{j}(\psi^{(m)}+\xi^{(m)})} \tag{4.70}$$

- Position of the damper on the root of blade $m+1$, where the position along the blade root is given by the parameter c_d:

$$p_{\mathrm{C}}^{(m+1)} = c_d \mathrm{e}^{\mathrm{j}\psi^{(m+1)}} \tag{4.71}$$

- Extremity of the rod close to blade $m+1$, where f is the length of the link between the damper and the extremity of the rod:

$$p_{\mathrm{F}}^{(m+1)} = p_{\mathrm{C}}^{(m+1)} + f\mathrm{e}^{\mathrm{j}(\psi^{(m+1)}+\pi+\gamma_F)} \tag{4.72}$$

- The same point $F^{(m+1)}$ can be retrieved starting from point $A^{(m)}$ and exploiting the length of the rod ℓ, and its relative rotation respect blade's m local reference frame $\zeta^{(m)}$:

$$p_{\mathrm{F}}^{(m+1)} = p_{\mathrm{A}}^{(m)} + \ell\mathrm{e}^{\mathrm{j}(\psi^{(m)}+\xi^{(m)}+\zeta^{(m)})} \tag{4.73}$$

Similarly to the IB case, the complex closure equation is obtained as:

$$p_{\mathrm{F,\,left}}^{(m+1)} = p_{\mathrm{F,\,right}}^{(m+1)} \tag{4.74}$$

Substituting the expression of all the points, the closure equation becomes:

$$c_f\mathrm{e}^{\mathrm{j}\psi^{(m+1)}} + f\mathrm{e}^{\mathrm{j}(\psi^{(m+1)}+\pi+\gamma_F)} = (x_{\mathrm{H}}+\mathrm{j}y_{\mathrm{H}})\mathrm{e}^{\mathrm{j}\psi^{(m)}} + (c_a+\mathrm{j}a)\mathrm{e}^{\mathrm{j}(\psi^{(m)}+\xi^{(m)})} + \ell\mathrm{e}^{\mathrm{j}(\psi^{(m)}+\xi^{(m)}+\zeta^{(m)})} \tag{4.75}$$

Having considered, at the moment, only the side of the equation related to blade m and $m+1$ the kinematic variables are the blade rotations, $\xi^{(m)}$, the damper rotation, γ_F, and the angle of the rod, $\zeta^{(m)}$.

The reference azimuth for each blade is $\psi^{(m)} = \psi_0 + m\Delta\psi$, with $\psi_0 = \Omega t$ when the rotor operates at constant angular velocity and $\Delta\psi = 2\pi/N_b$.

The equation can be simplified by multiplying it by $\mathrm{e}^{-\mathrm{j}\psi^{(m)}}$, yielding

$$-x_{\mathrm{H}} - \mathrm{j}y_{\mathrm{H}} - (c_a+\mathrm{j}a)\mathrm{e}^{\mathrm{j}\xi^{(m)}} - \ell\mathrm{e}^{\mathrm{j}(\xi^{(m)}+\zeta^{(m)})} + c_d\mathrm{e}^{\mathrm{j}\Delta\psi} - f\mathrm{e}^{\mathrm{j}(\Delta\psi+\gamma_F)} = 0 \tag{4.76}$$

Considering then the real and imaginary part of the complex equation Eq. (4.76):

$$c_f \cos\Delta\psi - f\cos(\Delta\psi+\gamma_F) - x_{\mathrm{H}} - \ell\cos(\xi^{(m)}+\zeta^{(m)}) - c_a\cos\xi^{(m)} + a\sin\xi^{(m)} = 0 \tag{4.77a}$$

$$c_f \sin\Delta\psi - f\sin(\Delta\psi+\gamma_F) - y_{\mathrm{H}} - \ell\sin(\xi^{(m)}+\zeta^{(m)}) - a\cos\xi(m) - c_a\sin\xi^{(m)} = 0 \tag{4.77b}$$

Following the same procedure, the closure equation for the left side of model is the relation between the blade lag angle $\xi^{(m+2)}$ and the left relative rotation of the damper γ_D and can be obtained by the closure equation of the vertices O, $\mathrm{H}^{(m+2)}$, $\mathrm{B}^{(m+2)}$, $\mathrm{D}^{(m+2)}$, $\mathrm{C}^{(m+1)}$

- Lag hinge of blade $m+2$:

$$p_{\mathrm{H}}^{(m+2)} = (x_{\mathrm{H}} + \mathrm{j}y_{\mathrm{H}})\mathrm{e}^{\mathrm{j}\psi^{(m+2)}} \tag{4.78}$$

- Extremity of the rod close to blade $m+2$, it presents an offset both in the $\tilde{x}$ direction and $\tilde{y}$ of blade's local frame of reference, the offset along the blade is represented by c_b while chordwise offset is given by b:

$$p_{\mathrm{B}}^{(m+2)} = p_{\mathrm{H}}^{(m+2)} + (c_b + \mathrm{j}b)\mathrm{e}^{\mathrm{j}(\psi^{(m+2)}+\xi^{(m+2)})} \tag{4.79}$$

- Position of the damper on the root of blade $m+1$, where the position along the blade root is given by the parameter c_d:

$$p_{\mathrm{C}}^{(m+1)} = c_d\mathrm{e}^{\mathrm{j}\psi^{(m+1)}} \tag{4.80}$$

- Extremity of the rod close to blade $m+1$, where d is the length of the link between the damper and the extremity of the rod:

$$p_{\mathrm{D}}^{(m+2)} = p_{\mathrm{C}}^{(m+1)} + d\mathrm{e}^{\mathrm{j}(\psi^{(m+1)}+\pi-\gamma_D)} \tag{4.81}$$

- The same point $\mathrm{D}^{(m+2)}$ can be retrieved starting from point $\mathrm{B}^{(m+2)}$ and exploiting the length of the rod ℓ, and its relative rotation with respect to the blade's $m+2$ local reference frame $\zeta^{(m+2)}$:

$$p_{\mathrm{D}}^{(m+2)} = p_{\mathrm{B}}^{(m+2)} + \ell\mathrm{e}^{\mathrm{j}(\psi^{(m+2)}+\xi^{(m+2)}+\zeta^{(m+2)})} \tag{4.82}$$

As in the previous case, the complex closure equation is obtained as:

$$p_{\text{D, left}}^{(m+2)} = p_{\text{D, right}}^{(m+2)} \tag{4.83}$$

Substituting the expression of each point, the closure equation becomes:

$$\begin{aligned} e\mathrm{e}^{\mathrm{j}\psi^{(m+2)}} + (c_b + \mathrm{j}b)\mathrm{e}^{\mathrm{j}(\psi^{(m+2)}+\xi^{(m+2)})} + \ell\mathrm{e}^{\mathrm{j}(\psi^{(m+2)}+\xi^{(m+2)}+\zeta^{(m+2)})} = \\ c_d\mathrm{e}^{\mathrm{j}\psi^{(m+1)}} + d\mathrm{e}^{\mathrm{j}(\psi^{(m+1)}+\pi-\gamma_D)} \end{aligned} \tag{4.84}$$

Having considered, only the side of the equation related to blade $m+1$ and $m+2$ the kinematic variables are the blade lag angle, $\xi^{(m+2)}$, the damper rotation, γ_D, and the angle of the rod, $\zeta^{(m+2)}$. As before, the equation can be simplified by multiplying it now by $\mathrm{e}^{-\mathrm{j}(\psi^{(m)}+\Delta\psi)}$, yielding:

$$-c_d + (x_{\mathrm{H}} + \mathrm{j}y_{\mathrm{H}})\mathrm{e}^{\mathrm{j}\Delta\psi} + (c_b + \mathrm{j}b)\mathrm{e}^{\mathrm{j}(\Delta\psi+\xi^{(m+2)})} + \ell\mathrm{e}^{\mathrm{j}(\Delta\psi+\xi^{(m+2)}+\zeta^{(m+2)})} + d\mathrm{e}^{-\mathrm{j}\gamma_D} = 0 \tag{4.85}$$

Considering then the real and imaginary part of the complex equation Eq. (4.85):

$$\begin{aligned} c_b\cos(\Delta\psi+\xi^{(m+2)}) - c_d - b\sin(\Delta\psi+\xi^{(m+2)}) + x_{\mathrm{H}}\cos\Delta\psi + d\cos\gamma_D \\ - y_{\mathrm{H}}\sin\Delta\psi + \ell\cos(\Delta\psi+\xi^{(m+2)}+\zeta^{(m+2)}) = 0 \end{aligned} \tag{4.86a}$$

$$\begin{aligned} b\cos(\Delta\psi+\xi^{(m+2)}) + c_b\sin(\Delta\psi+\xi^{(m+2)}) + y_{\mathrm{H}}\cos\Delta\psi + x_{\mathrm{H}}\sin\Delta\psi \\ - d\sin\gamma_D + \ell\sin(\Delta\psi+\xi^{(m+2)}+\zeta^{(m+2)}) = 0 \end{aligned} \tag{4.86b}$$

The real and imaginary parts of the two closure equations can be solved numerically for given values of the blade angles. The first closure equation is used to compute $\xi^{(m)}$, and starting from the reference condition, it allows determining the corresponding values of γ_F and $\zeta^{(m)}$. Similarly, the second one is used for $\xi^{(m+2)}$, from which the values of γ_D and $\zeta^{(m+2)}$ can be obtained.

Once the solution of the two closure equations $\boldsymbol{\phi}(\boldsymbol{\xi}, \mathbf{x}_d) = \mathbf{0}$ has been obtained, the relationship between the lead-lag angles and the dampers' relative rotations can be computed following the formulation of the general problem.

Respect the IB problem since have been used two different closure equations the size of the problem is doubled, the vector of the kinematic unknowns will have the following

expression:

$$\mathbf{x}_d = \begin{Bmatrix} \gamma_F \\ \gamma_D \\ \zeta^{(m)} \\ \zeta^{(m+2)} \end{Bmatrix} \tag{4.87}$$

where the relative rotation of the damper $\varphi^{(m)}$ is given by:

$$\varphi^{(m)} = \gamma_F^{(m)} - \gamma_D^{(m)} \tag{4.88}$$

From the computation of the time derivative of the closure equation the matrices that link the the lag angles to the relative damper angle can be obtained:

$$\boldsymbol{\phi}_{/\boldsymbol{\xi}} = \begin{bmatrix} \phi_{\mathrm{Re}_1/\xi^{(m)}} & \phi_{\mathrm{Re}_1/\xi^{(m+2)}} \\ \phi_{\mathrm{Im}_1/\xi^{(m)}} & \phi_{\mathrm{Im}_1/\xi^{(m+2)}} \\ \phi_{\mathrm{Re}_2/\xi^{(m)}} & \phi_{\mathrm{Re}_2/\xi^{(m+2)}} \\ \phi_{\mathrm{Im}_2/\xi^{(m)}} & \phi_{\mathrm{Im}_2/\xi^{(m+2)}} \end{bmatrix} \tag{4.89}$$

Having defined the closure equations as it follows: Re, Im part of Eq. (4.76), as Re_1 and Im_1, while Re, Im part of Eq. (4.85) as Re_2 and Im_2. The matrix relative to the derivative of the internal coordinates:

$$\boldsymbol{\phi}_{/\mathrm{x_d}} = \begin{bmatrix} \phi_{\mathrm{Re}_1/\gamma_F} & \phi_{\mathrm{Re}_1/\gamma_D} & \phi_{\mathrm{Re}_1/\zeta^{(m)}} & \phi_{\mathrm{Re}_1/\zeta^{(m+2)}} \\ \phi_{\mathrm{Im}_1/\gamma_F} & \phi_{\mathrm{Im}_1/\gamma_D} & \phi_{\mathrm{Im}_1/\zeta^{(m)}} & \phi_{\mathrm{Im}_1/\zeta^{(m+2)}} \\ \phi_{\mathrm{Re}_2/\gamma_F} & \phi_{\mathrm{Re}_2/\gamma_D} & \phi_{\mathrm{Re}_2/\zeta^{(m)}} & \phi_{\mathrm{Re}_2/\zeta^{(m+2)}} \\ \phi_{\mathrm{Im}_2/\gamma_F} & \phi_{\mathrm{Im}_2/\gamma_D} & \phi_{\mathrm{Im}_2/\zeta^{(m)}} & \phi_{\mathrm{Im}_2/\zeta^{(m+2)}} \end{bmatrix} \tag{4.90}$$

The expressions of the partial derivatives of the system equations with respect to the kinematic variables and internal coordinates are reported in Table 4.4.

Table 4.4: Partial derivatives of the closure equations with respect to kinematic and internal variables for I2B kinematic model.

Variable	$\phi_{\mathrm{Re}_1}, \phi_{\mathrm{Im}_1}$	$\phi_{\mathrm{Re}_2}, \phi_{\mathrm{Im}_2}$
$\xi^{(m)}$	$c_a \sin\xi^{(m)} + a\cos\xi^{(m)} + \ell\sin(\xi^{(m)} + \zeta^{(m)})$ $- c_a \cos\xi^{(m)} + a\sin\xi^{(m)} - \ell\cos(\xi^{(m)} + \zeta^{(m)})$	0
$\xi^{(m+2)}$	0	$- c_b \sin(\Delta\psi + \xi^{(m+2)}) - b\cos(\Delta\psi + \xi^{(m+2)})$ $- \ell\sin(\Delta\psi + \xi^{(m+2)} + \zeta^{(m+2)})$ $+ c_b \cos(\Delta\psi + \xi^{(m+2)}) - b\sin(\Delta\psi + \xi^{(m+2)})$ $+ \ell\cos(\Delta\psi + \xi^{(m+2)} + \zeta^{(m+2)})$
γ_F	$f\sin(\Delta\psi + \gamma_F)$ $- f\cos(\Delta\psi + \gamma_F)$	0
γ_D	0	$- d\sin(\gamma_D)$ $- d\cos(\gamma_D)$
$\zeta^{(m)}$	$\ell\sin(\xi^{(m)} + \zeta^{(m)})$ $- \ell\cos(\xi^{(m)} + \zeta^{(m)})$	0
$\zeta^{(m+2)}$	0	$- \ell\sin(\Delta\psi + \xi^{(m+2)} + \zeta^{(m+2)})$ $+ \ell\cos(\Delta\psi + \xi^{(m+2)} + \zeta^{(m+2)})$

From the derivation of the two closure equations, the following system is obtained:

$$\boldsymbol{\phi}_{/\boldsymbol{\xi}} \begin{Bmatrix} \dot{\xi}^{(m)} \\ \dot{\xi}^{(m+2)} \end{Bmatrix} + \boldsymbol{\phi}_{/\mathbf{x}_d} \begin{Bmatrix} \dot{\gamma}_F^{(m)} \\ \dot{\gamma}_D^{(m)} \\ \dot{\zeta}^{(m)} \\ \dot{\zeta}^{(m+2)} \end{Bmatrix} = \mathbf{0} \tag{4.91}$$

So the term Ψ_φ that relates the relative dampers' angle to the lag $\xi^{(m)}$ and $\xi^{(m+2)}$ can be computed. This term will be used to transform the damping and stiffness matrices from the relative damper coordinates to the lag coordinates.

Recalling the virtual work equivalence, Eq. (4.7), the matrices of stiffness and damping can be computed as a function of the lead-lag coordinates.

In the case of a 5-blade configuration, the general formulation leads to a system of 10 closure equations, corresponding to two equations per damper. By introducing the assumption of complete symmetry in the damper arrangement across the rotor, the problem can be significantly simplified, following an approach analogous to that adopted for the

IB configuration.

$$\dot{\varphi} = \dot{\gamma_F} - \dot{\gamma_D} = \mathbf{C}_{\gamma_F x_d}\dot{\mathrm{x}}_d - \mathbf{C}_{\gamma_D x_d}\dot{\mathrm{x}}_d = \left(-\mathbf{C}_{\gamma_F x_d}\boldsymbol{\phi}^{-1}_{/\mathrm{x_d}}\,\boldsymbol{\phi}_{/\boldsymbol{\xi}} + \mathbf{C}_{\gamma_D x_d}\boldsymbol{\phi}^{-1}_{/\mathrm{x_d}}\,\boldsymbol{\phi}_{/\boldsymbol{\xi}}\right)\dot{\boldsymbol{\xi}} \tag{4.92}$$

The matrices $\mathbf{C}_{\gamma x_d}$ extracts γ_F and γ_D from the vector and allows the relative damper rotations expression of the lead-lag angles to be obtained. So the matrix Ψ_φ can be defined as:

$$\dot{\boldsymbol{\varphi}} = \Psi_\varphi \dot{\boldsymbol{\xi}} \tag{4.93}$$

The matrix of stiffness and damping can be transformed, leading the their expression as a function of the lag angles:

$$\mathbf{C}_\xi = \Psi_\varphi^T \mathbf{C}_\varphi \Psi_\varphi \tag{4.94}$$

$$\mathbf{K}_\xi = \Psi_\varphi^T \mathbf{K}_\varphi \Psi_\varphi \tag{4.95}$$

Due to symmetry considerations, since the rotor can be considered isotropic with the same geometrical properties for all the dampers and blades, the vector that relates the relative angle φ to the lag angles $\boldsymbol{\xi}$ results in being the same for all the closure equations.

Considering only the first closure equation, the damper mounted on the blade of azimuth $\xi^{(1)}$, the relative damper rotation is related to the previous blade 5 and the consecutive one blade 2:

$$\dot{\varphi}^{(1)} = \begin{bmatrix}\Psi_1 & \Psi_2\end{bmatrix}\begin{Bmatrix}\dot{\xi}^5 \\ \dot{\xi}^2\end{Bmatrix} \tag{4.96}$$

Exploiting the symmetry of the rotor the global Ψ_φ matrix can be written as:

$$\Psi_\varphi = \begin{bmatrix} 0 & \Psi_2 & 0 & 0 & \Psi_1 \\ \Psi_1 & 0 & \Psi_2 & 0 & 0 \\ 0 & \Psi_1 & 0 & \Psi_2 & 0 \\ 0 & 0 & \Psi_1 & 0 & \Psi_2 \\ \Psi_2 & 0 & 0 & \Psi_1 & 0 \end{bmatrix} \tag{4.97}$$

4.3.2. Results for for Inter-2-Blade Configuration with Interblade Damper's Characteristics

Considering the same damper properties of the IB problem, the GR problem is solved for the symmetrical I2B configuration, as shown in the kinematic model, as can be seen in Fig. 4.14, this configuration is similar tot the one developed and studied in the previous thesis [1, 8] and presented in Chap. 3.

The transmission ratios for this I2B symmetrical configuration are:

$$\Psi_{\varphi} = \begin{bmatrix} -1.9067 & 1.9066 \end{bmatrix} \tag{4.98}$$

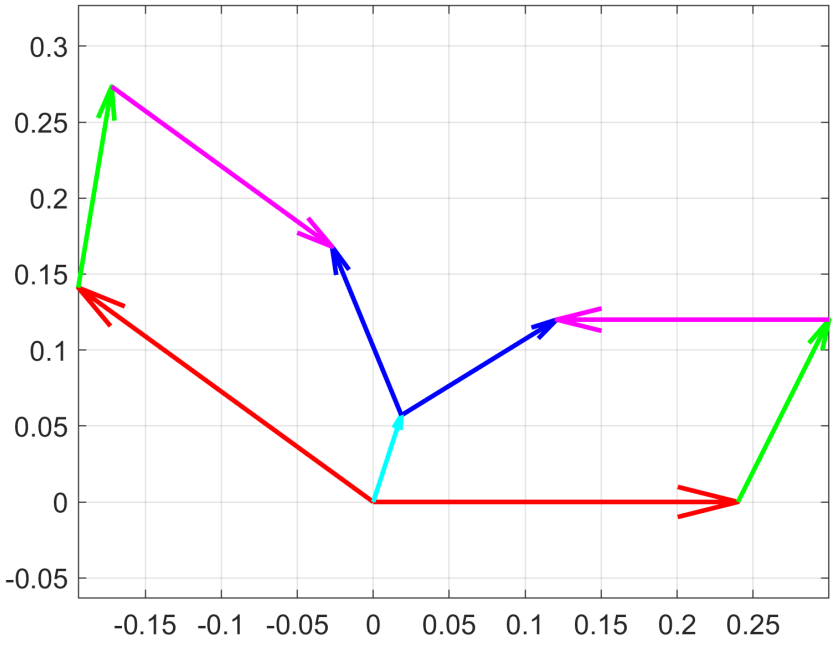

Figure 4.14: I2B symmetric configuration

Starting from this symmetrical configuration GR problem will be solved, initially with the same damper properties of the IB kinematic model, then, exploiting the sensitivity approach, damper's coefficients will be tuned in order to obtain the prescribed damping initially on the ξ_{1_c} mode maintaining the symmetry of the kinematics, then, by breaking the symmetry and also introducing damping on the collective mode ξ_0.

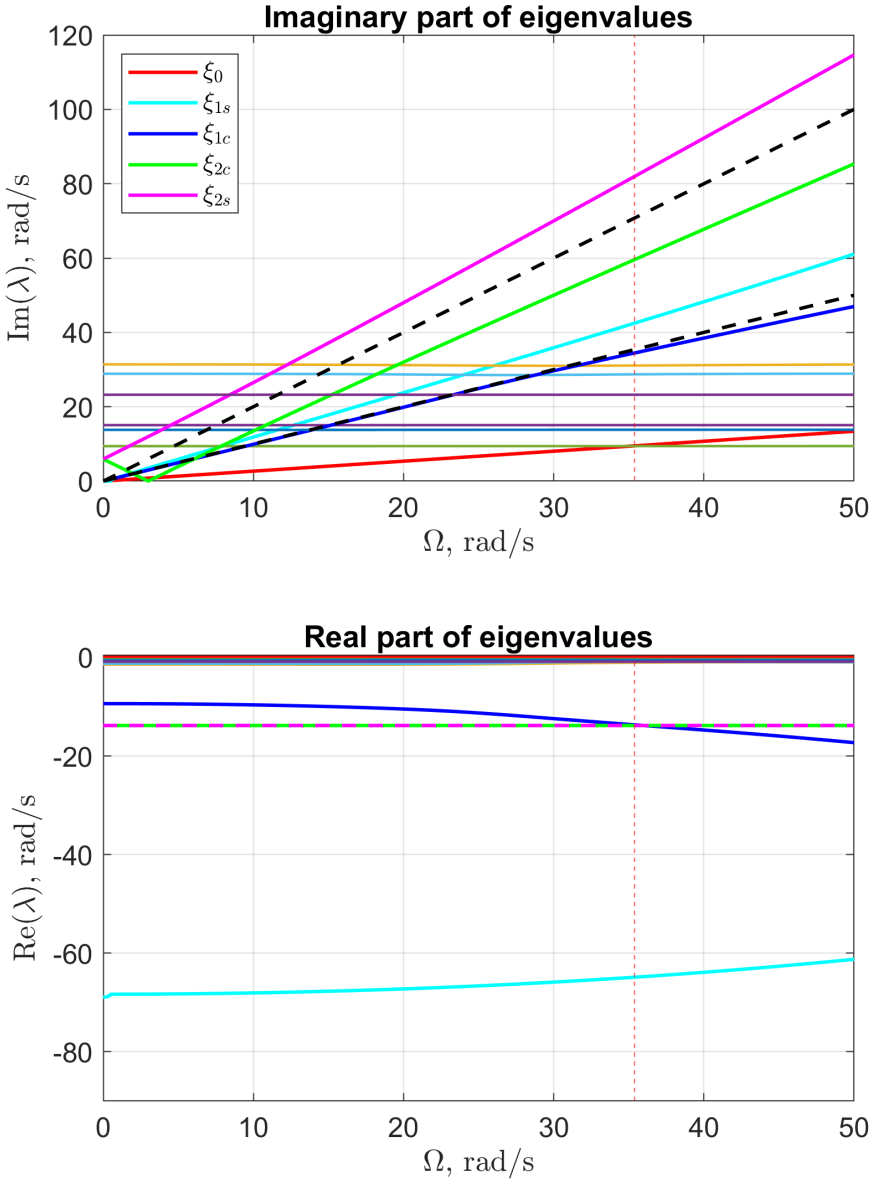

Figure 4.15: GR problem for I2B damper configuration with same damper properties of IB problem

As shown in Fig. 4.15, mounting a damper with mechanical characteristics identical to those of the IB problem is not ideal; the resulting eigenvalues indicate an overdamped system.

4.3.3. Damper Coefficients for the Inter-2-Blade Problem

To solve the ground resonance problem for a generic medium-weight helicopter with a defined geometry in the I2B configuration, the damper characteristics K_d and C_d from the IB problem cannot be directly applied, as has been shown in Fig. 4.15.

To obtain comparable results between the two configurations, appropriate damping and stiffness coefficients for the I2B damper must be identified. This is achieved by exploiting the sensitivity-based approach presented in Chapter 3.

Since the critical eigenvalue in the IB scenario corresponds to the first cyclic mode causing instability above nominal Ω, only the first cyclic multilblade coordinates ξ_{1_c} and ξ_{1_s} are considered, so the blade equation reduces to:

$$\mathbf{M}_{\mathrm{bmb}_q}\ddot{\mathbf{q}} + \mathbf{C}_{\mathrm{bmb}_q}\dot{\mathbf{q}} + \mathbf{K}_{\mathrm{bmb}_q}\mathbf{q} = \mathbf{0} \tag{4.99}$$

where the pedix $\mathbf{q}$ stands for the first cyclic couple, so the mass, damping and stiffness matrix are reduced only to the relevant MBC of the system.

For the IB problem, the known damper properties K_d and C_d allow direct computation of cyclic mode frequencies and damping. Using the kinematic relationship between damper rotation φ and blade lag angles $\boldsymbol{\xi}$, equivalent coefficients for the I2B problem K_ξ and C_ξ are derived.

For the I2B problem, the goal is to match the critical eigenvalue at nominal speed by adjusting damper coefficients. Starting from initial guesses $K_{d,I2B} = 0$ and $C_{d,I2B} = 0$, the critical eigenvalue is computed, and its sensitivities to K_d and C_d are evaluated by solving:

$$\begin{bmatrix} \lambda_{1c}^2\mathbf{M}_{\mathrm{I2B}} + \lambda_{1c}\mathbf{C}_{\mathrm{I2B}} + \mathbf{K}_{\mathrm{I2B}} & (2\lambda_{1c}\mathbf{M}_{\mathrm{I2B}} + \mathbf{C}_{\mathrm{I2B}})\mathbf{q} \\ \mathbf{q}^T & 0 \end{bmatrix} \begin{Bmatrix} \mathbf{q}_{/C_d} \\ \lambda_{/C_d} \end{Bmatrix} = \begin{pmatrix} -(\lambda_{1c}^2\mathbf{M}_{/C_d} + \lambda_{1c}\mathbf{C}_{/C_d} + \mathbf{K}_{/C_d})\mathbf{q} \\ 0 \end{pmatrix} \tag{4.100}$$

Similar expressions hold for stiffness sensitivity ($/K_d$) terms. Using these sensitivities, increments ΔK_d and ΔC_d are computed by solving the linear system:

$$\lambda_{1c,IB} = \lambda_{1c,I2B} + \lambda_{1c,I2B/K_d}\Delta K_d + \lambda_{1c,I2B/C_d}\Delta C_d \tag{4.101}$$

Separating real and imaginary parts yields to two equations, which are solved iteratively until convergence.

After a few iterations, the damper coefficients are $K_{d,\text{I2B}} = 2839.92$ N/rad and $C_{d,\text{I2B}} = 347.10$ Nms/rad such that the critical eigenvalue frequency and damping match those of the IB problem at nominal speed.

Isolated Rotor Analysis

Observing the GR problem for the isolated rotor scenario, Fig. 4.17, with no coupling to the airframe, it can be noted that, given the symmetric geometry of the I2B scheme, there is no damping on the collective modes. However, this will be further investigated in the next section. Instead, the cyclic regressive and progressive mode, on the other hand, have the same damping and frequency as the one in the IB scenario; therefore, the coefficients have been determined correctly. The main difference lies in the fact that the damping characteristics are significantly lower when compared to the IB problem, although their relative ratio remains the same.

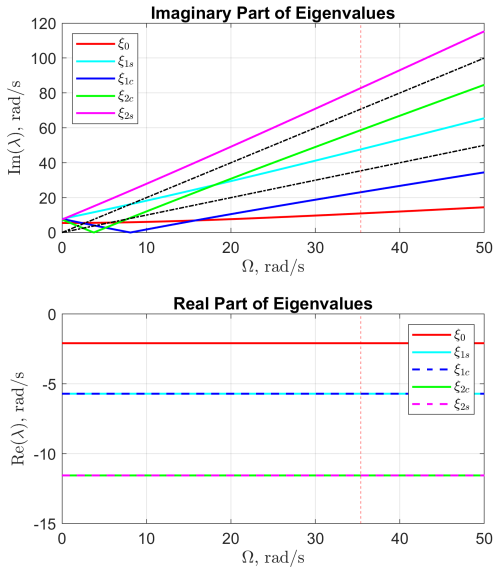

Figure 4.16: Isolated rotor IB GR

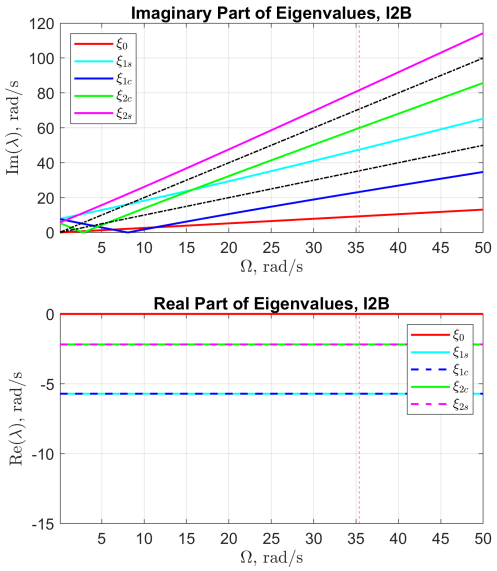

Figure 4.17: Isolated rotor I2B GR

Figure 4.18: Comparison between IB and I2B isolated rotor GR results

Rotor Coupled with Airframe Analysis

Regarding the coupled problem, the new damper coefficients exhibit a similar behavior to the IB problem. The coupling between the airframe and rotor modes results in

the same instability bubble observed in the IB problem, but with stiffness and damping characteristics that might be achieved with a smaller damper.

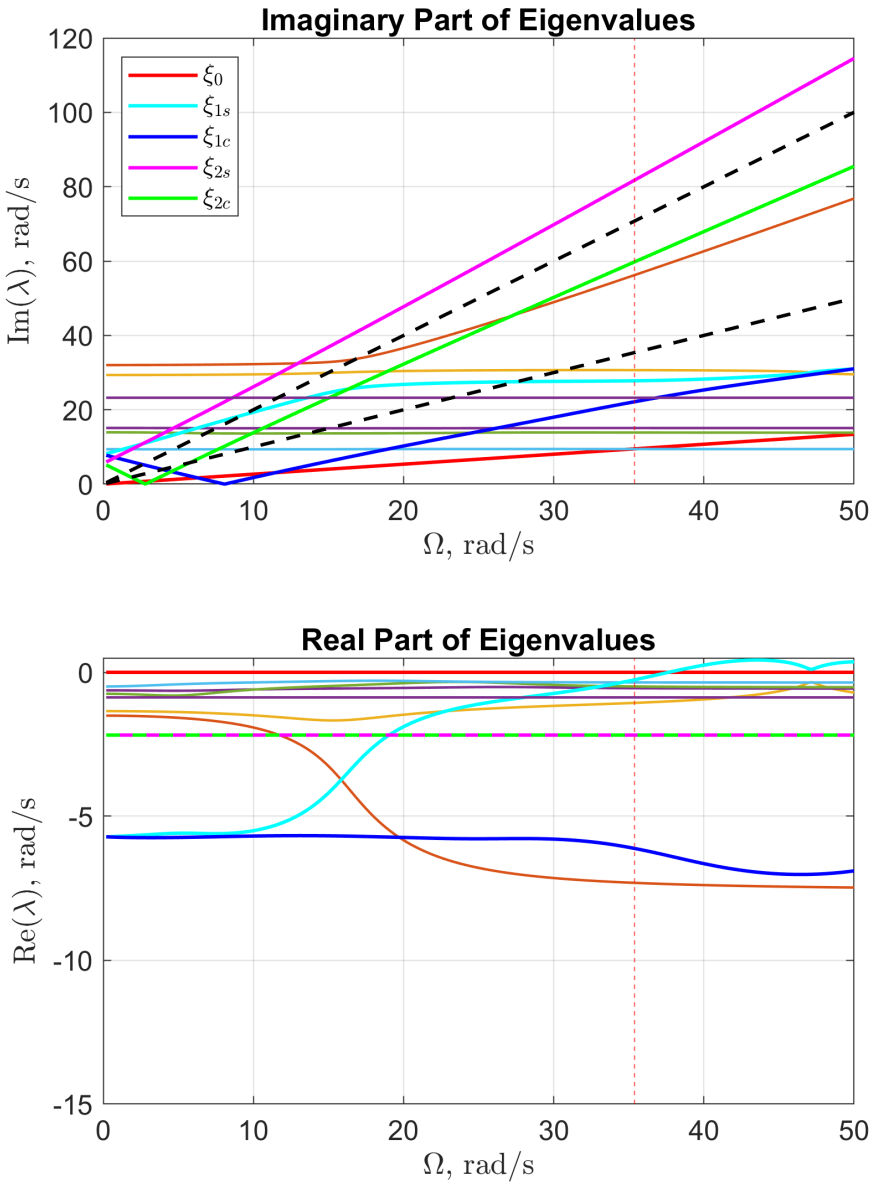

Figure 4.19: Rotor coupled with airframe, I2B problem, $\xi_{1c,s}$ tuning.

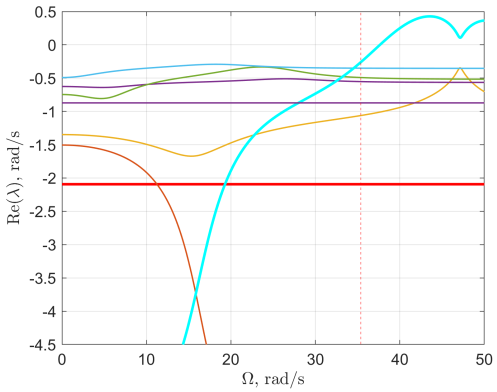

Figure 4.20: Zoom of real part – IB GR

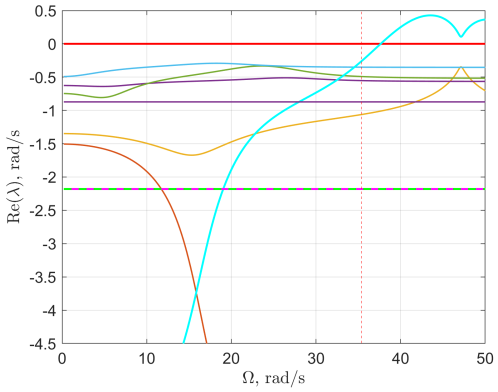

Figure 4.21: Zoom of real part – I2B GR (cyclic tuning)

Figure 4.22: Close-up comparison of the real part of the eigenvalues for IB and I2B in the critical region

Observing Fig. 4.21, it can be seen that the instability bubble has the same characteristics as in the IB case. It can also be observed that the ξ_0 mode, highlighted in red, has no damping. This will be a crucial aspect analyzed in the following section — namely, the breaking of the symmetry in the I2B kinematics (Fig. 4.14).

4.3.4. Introducing Damping also on the Collective Mode

As already pointed out in the GR results of the I2B problem with damper coefficient's tuned for the cyclic mode, a symmetrical configuration of the I2B geometry of the rotor doesn't provide any damping on collective lag mode ξ_0, but its symmetry can be broken by modifying the lengths of the rods d and f and other geometrical parameters to achieve the desired damping on the collective mode ξ_0, or at least a value comparable to the one present in the IB configuration. The target damping and natural frequency are those obtained in the IB model at the nominal angular speed. Therefore, the lengths of these rods can be tuned to match the prescribed values for the collective mode. Simultaneously, the damper characteristics K_d and C_d can be adjusted to achieve the required damping and frequency on the slower cyclic mode ξ_{1c}, as described in § 4.3.3.

Starting from Eq. (4.100), terms related to the sensitivity to the length of the arms have to be added, and also an equation related to the collective eigenvalue.

So the problem becomes:

$$\lambda_{1c,\mathrm{IB}} = \lambda_{1c,\mathrm{I2B}} + \lambda_{1c,\mathrm{I2B}/K_d}\,\Delta K_d + \lambda_{1c,\mathrm{I2B}/C_d}\,\Delta C_d + \lambda_{1c,\mathrm{I2B}/d}\,\Delta d + \lambda_{1c,\mathrm{I2B}/f}\,\Delta f \tag{4.102a}$$

$$\lambda_{0,\mathrm{IB}} = \lambda_{0,\mathrm{I2B}} + \lambda_{0,\mathrm{I2B}/K_d}\,\Delta K_d + \lambda_{0,\mathrm{I2B}/C_d}\,\Delta C_d + \lambda_{0,\mathrm{I2B}/d}\,\Delta d + \lambda_{0,\mathrm{I2B}/f}\,\Delta f \tag{4.102b}$$

By separating the real and imaginary part of Eq. (4.102) is obtained the system that has to be solved until convergence is obtained:

$$\begin{bmatrix} \mathrm{Re}(\lambda_{1\mathrm{c},\,\mathrm{I2B}/K_d}) & \mathrm{Re}(\lambda_{1\mathrm{c},\,\mathrm{I2B}/C_d}) & \mathrm{Re}(\lambda_{1\mathrm{c},\,\mathrm{I2B}/d}) & \mathrm{Re}(\lambda_{1\mathrm{c},\,\mathrm{I2B}/f}) \\ \mathrm{Im}(\lambda_{1\mathrm{c},\,\mathrm{I2B}/K_d}) & \mathrm{Im}(\lambda_{1\mathrm{c},\,\mathrm{I2B}/C_d}) & \mathrm{Im}(\lambda_{1\mathrm{c},\,\mathrm{I2B}/d}) & \mathrm{Im}(\lambda_{1\mathrm{c},\,\mathrm{I2B}/f}) \\ \mathrm{Re}(\lambda_{0,\,\mathrm{I2B}/K_d}) & \mathrm{Re}(\lambda_{0,\,\mathrm{I2B}/C_d}) & \mathrm{Re}(\lambda_{0,\,\mathrm{I2B}/d}) & \mathrm{Re}(\lambda_{0,\,\mathrm{I2B}/f}) \\ \mathrm{Im}(\lambda_{0,\,\mathrm{I2B}/K_d}) & \mathrm{Im}(\lambda_{0,\,\mathrm{I2B}/C_d}) & \mathrm{Im}(\lambda_{0,\,\mathrm{I2B}/d}) & \mathrm{Im}(\lambda_{0,\,\mathrm{I2B}/f}) \end{bmatrix} \begin{Bmatrix} \Delta K_d \\ \Delta C_d \\ \Delta d \\ \Delta f \end{Bmatrix} = \begin{pmatrix} \mathrm{Re}(\lambda_{1\mathrm{c},\,\mathrm{I2B}} - \lambda_{1\mathrm{c},\,\mathrm{IB}}) \\ \mathrm{Im}(\lambda_{1\mathrm{c},\,\mathrm{I2B}} - \lambda_{1\mathrm{c},\,\mathrm{IB}}) \\ \mathrm{Re}(\lambda_{0,\,\mathrm{I2B}} - \lambda_{0,\,\mathrm{IB}}) \\ \mathrm{Im}(\lambda_{0,\,\mathrm{I2B}} - \lambda_{0,\,\mathrm{IB}}) \end{pmatrix} \tag{4.103}$$

As done in § 4.3.3, from the isolated rotor problem, at the nominal angular speed, are now extracted the collective and cyclic slower components, ξ_0 and ξ_{1c}. Instead, for computing the sensitivity with respect to the lengths, the dependence is embedded in the kinematic model. As an example is computed the sensitivity for the arm f but for all the lengths, the process is analogous.

The mass matrix $\mathbf{M}_b$ has no dependence on the kinematics, so it will have null contribution, $\mathbf{M}_{b/f} = \mathbf{0}$.

Instead, the damping and stiffness matrices are strictly related to the geometry through the transformation matrix $\Psi_{\varphi_{I2B}}$.

$$\begin{aligned} \mathbf{C}_{\xi/f} &= \Psi^T_{\varphi_{I2B}/f}\mathbf{C}_{\varphi_{I2B}}\Psi_{\varphi_{I2B}} + \Psi^T_{\varphi_{I2B}}\mathbf{C}_{\varphi_{I2B}}\Psi_{\varphi_{I2B}/f} \\ \mathbf{C}_{b/f} &= \mathbf{T}^T(\mathbf{C}_{\xi/f}\mathbf{T} + 2\mathbf{M}_{\xi/f}\dot{\mathbf{T}}) = \mathbf{T}^T(\Psi^T_{\varphi_{I2B}/f}\mathbf{C}_{\varphi_{I2B}}\Psi_{\varphi_{I2B}} + \Psi^T_{\varphi_{I2B}}\mathbf{C}_{\varphi_{I2B}}\Psi_{\varphi_{I2B}/f})\mathbf{T} \end{aligned} \tag{4.104}$$

Similarly, for the stiffness matrix, its expression—when written in a non-rotating coordinate system—must also take into account the derivative of the damping matrix due to the MBC transformation.

$$\mathbf{K}_{\xi/f} = \mathbf{\Psi}^T_{\varphi_{I2B}/f}\mathbf{K}_{\varphi_{I2B}}\mathbf{\Psi}_{\varphi_{I2B}} + \mathbf{\Psi}^T_{\varphi_{I2B}}\mathbf{K}_{\varphi_{I2B}}\mathbf{\Psi}_{\varphi_{I2B}/f} \tag{4.105}$$

$$\mathbf{K}_{b/f} = \mathbf{T}^T\left(\mathbf{K}_{\xi/f}\mathbf{T} + \mathbf{C}_{\xi/f}\dot{\mathbf{T}} + \mathbf{M}_{\xi/f}\ddot{\mathbf{T}}\right) \tag{4.106}$$

$$\begin{aligned} &= \mathbf{T}^T\Big(\mathbf{\Psi}^T_{\varphi_{I2B}/f}\mathbf{K}_{\varphi_{I2B}}\mathbf{\Psi}_{\varphi_{I2B}}\,\mathbf{T} + \mathbf{\Psi}^T_{\varphi_{I2B}}\mathbf{K}_{\varphi_{I2B}}\mathbf{\Psi}_{\varphi_{I2B}/f}\,\mathbf{T} \\ &\quad + \mathbf{\Psi}^T_{\varphi_{I2B}/f}\mathbf{C}_{\varphi_{I2B}}\mathbf{\Psi}_{\varphi_{I2B}}\,\dot{\mathbf{T}} + \mathbf{\Psi}^T_{\varphi_{I2B}}\mathbf{C}_{\varphi_{I2B}}\mathbf{\Psi}_{\varphi_{I2B}/f}\,\dot{\mathbf{T}}\Big) \end{aligned} \tag{4.107}$$

To select an ideal geometry for the I2B configuration—aimed at achieving the desired damping on both the collective and cyclic modes—a more comprehensive model was developed, extending beyond the simplified scenario reported in (4.103) where only the lengths of the arms were considered.

In this generalized formulation, all the geometrical parameters listed in Table 3.2 are taken into account. Starting from the symmetric I2B configuration, which inherently exhibits no damping in the collective mode, an optimization problem was formulated.

Constraints were imposed on the allowable perturbations of each parameter, defining both lower and upper bounds. This was necessary to ensure compliance with the geometric constraints dictated by the rotor layout and to guarantee physical admissibility, such as requiring positive values for the damper characteristics.

At each iteration, the sensitivity of the two targeted eigenvalues, ξ_0 and ξ_{1_c}, with respect to the design parameters was evaluated. This sensitivity information was embedded in the transformation matrix, as presented in the general problem formulation (Eq. (4.103)). The optimization was solved by minimizing a penalty function, where each parameter variation was weighted according to its relative influence, thus prioritizing modifications that yield the desired eigenvalue shift with minimal deviation from the reference geometry.

Through a few iterations, comparable results in terms of damping and frequency for the I2B configuration, relative to the IB one, were achieved and are reported in Table 4.5, the transmission ratio obtained from the optimized geometry $\Psi_{\varphi,\text{I2B}}$ resulted to be:

$$\Psi_{\varphi,\text{I2B}} = \begin{bmatrix} -1.878 & 0.454 \end{bmatrix} \tag{4.108}$$

In Table 4.5 are reported the damping and frequency, as well as real and imaginary part of the collective mode and first cyclic regressive at nominal RPM; for both the IB problem and the I2B tuned one.

Table 4.5: Frequency, Damping ratio and Real and Imaginary parts for ξ_0 and ξ_{1c}.

Parameter	ξ_0 **(IB)**	ξ_0 **(I2B)**	**Diff [%]**	ξ_{1c} **(IB)**	ξ_{1c} **(I2B)**	**Diff [%]**
Freq., Hz	1.7415	1.7450	-0.20	3.8140	3.8145	-0.12
ξ, [–]	0.1913	0.1975	-3.12	0.2381	0.2278	4.55
Re, rad/s	-2.0935	-2.1652	-3.32	-5.7070	-5.4651	4.43
Im, rad/s	10.7402	10.7484	-0.08	23.2747	23.3618	-0.37

Although the slight variations in the real part of the eigenvalues, this method successfully introduces damping on the collective mode, while the damping on the cyclic remains the same. The damper coefficients obtained for this configuration are: $K_d = 6973.06\,\text{Nm/rad}$, $C_d = 854.62\,\text{Nms/rad}$.

The resulting geometry is no longer symmetrical, as can be seen in Fig. 4.23; this asymmetry allows for non-zero damping in the collective mode:

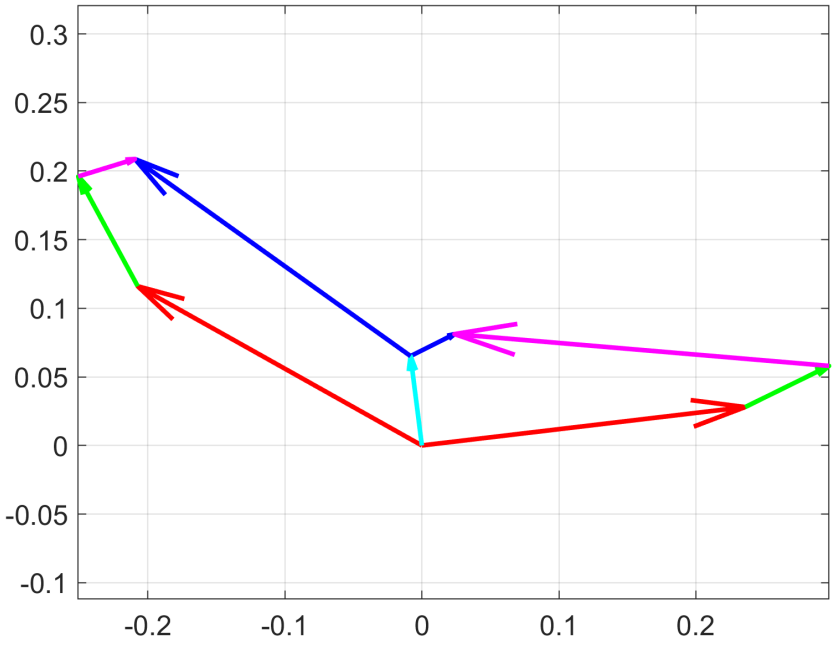

Figure 4.23: Damper geometry for damping on collective and cyclic modes

The comparison between the two kinematic models, IB and I2B, with coefficients tuned is summarized in Table 4.6. It can be observed that, with the I2B geometry, similar damping coefficients of collective and cyclic regressive modes are obtained with inferior

damper characteristics.

Table 4.6: Damper coefficients IB vs I2B, damping on ξ_0 and ξ_{1_c}

Configuration	**Damper stiffness,** K_d	**Damper Damping,** C_d
IB (original)	18000 N m rad^{-1}	2200 N m s rad^{-1}
I2B (tuned)	6973.06 N m rad^{-1}	854.63 N m s rad^{-1}

Having tuned the I2B kinematic model, it can be observed in detail the same behavior as for the IB problem appears in the I2B in the critical speed range. Also, the collective mode, ξ_0, highlighted in red, is now damped, whereas it was previously undamped while the cyclic progressive mode ξ_{1_s} highlighted in cyan present the same damping as for the IB problem.

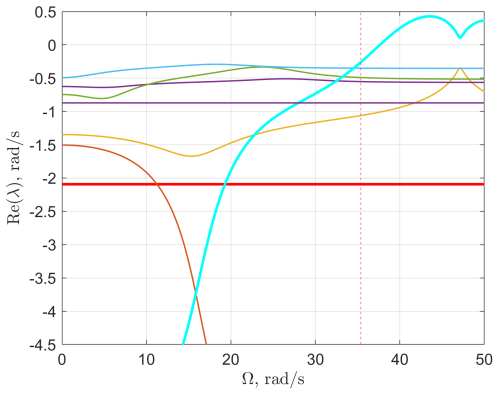

Figure 4.24: Zoom of real part – IB GR

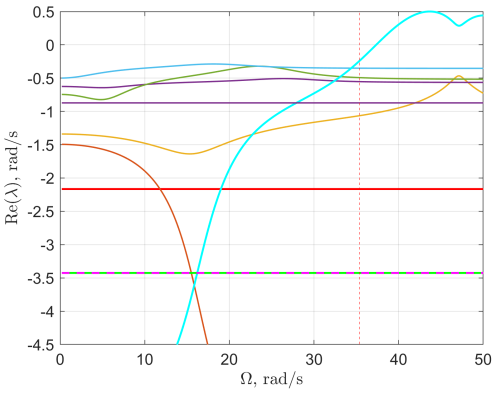

Figure 4.25: Zoom of real part – I2B GR

Figure 4.26: Close-up comparison of the real part of the eigenvalues for IB and I2B GR problems.

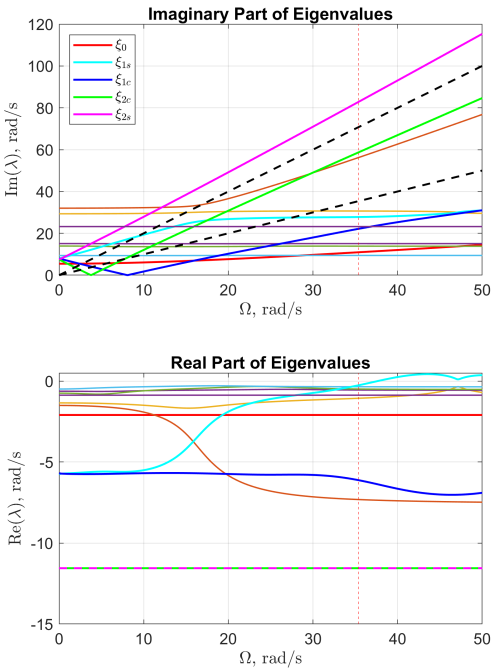

Figure 4.27: IB GR

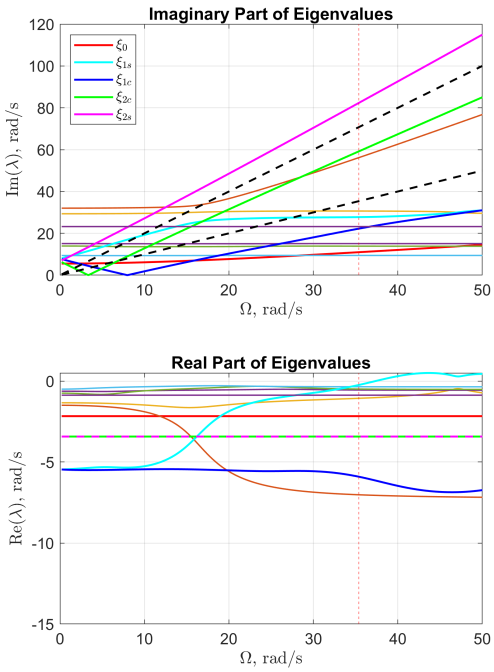

Figure 4.28: I2B GR tuned

Figure 4.29: Comparison between IB and I2B GR results.

4.4. Comparative Analysis of Different Damper Architectures

4.4.1. All Dampers Operative Comparison

In the previous sections, starting from a general model capable of reproducing different kinematic layouts and damper arrangements, a representative kinematic model of a modern medium-weight helicopter equipped with an IB damper arrangement was developed. Subsequently, alternative configurations were derived by exploiting eigenvalue sensitivity analyses of the GR problem.

An analysis of the damper coefficients required to achieve the same damping level on the multiblade mode is therefore presented. This was carried out to investigate how the damper configuration and the tuning of the coefficient affects the effective damping on the mode, recalling the amplification factors introduced in [13].

The different damper coefficients, obtained through sensitivity analysis for the various configurations, are reported in Table 4.7. Although these values may appear representa-

tive, the damper characteristics alone do not directly reveal how the multiblade modes are actually damped.

Table 4.7: Damper coefficients for different configurations

Configuration	**Damper stiffness,** K_d	**Damper Damping,** C_d
BTH (tuned ξ_{1c})	37354.57 N m rad^{-1}	4565.60 N m s rad^{-1}
IB (original)	18000 N m rad^{-1}	2200 N m s rad^{-1}
I2B (tuned ξ_{1c})	2839.92 N m rad^{-1}	347.10 N m s rad^{-1}

In order to have a meaningful element to compare the different damping on the multiblade mode, having assembled the different model (BTH and I2B) in order to have the same damping and frequency on ξ_{1_c}, the relative ratios between the damping coefficients of the first cyclic component can be computed.

The results are reported in Table 4.8, where the damping coefficient for the cyclic component, denoted as C_ξ, is extracted from the damping matrix transformed into multiblade coordinates, $\mathbf{C}_\mathrm{b}$, and normalized by the number of blades as $N_b/2$. This term arises from the transformation of the damping matrix. Subsequently, the ratio between the reference damping value $C_{\xi,\mathrm{BTH}}$ and the value extracted from the damping matrix is computed.

Table 4.8: Damper coefficients comparison between architectures

Configuration	ξ_{1_c} Damping, C_ξ	$C_{\xi,\mathrm{BTH}}/C_\xi$	**Ratio patent** Ξ
BTH (tuned)	4565.6 N m rad^{-1}	—	—
IB (original)	3303.7 N m rad^{-1}	1.3820	$2(1-\cos(\Delta\psi)) = 1.3820$
I2B (tuned)	1261.9 N m rad^{-1}	3.6180	$2(1-\cos(2\Delta\psi)) = 3.6180$

It can be observed that the coefficients reported in Table 4.8 exactly correspond to Ξ_1 and Ξ_2, as previously introduced and derived in [13]. Therefore, the advantage offered by the alternative damper configurations, as discussed within the generalized Deutsch criterion in Section 2.4, is preserved even when a more realistic kinematic model is considered and after the eigenvalue tuning has been performed.

This represents a further advancement in the analysis of the I2B damper configuration, since the coefficients provided in the patent were originally derived in the context of a simplified theoretical framework—namely, the "Hammond-type" problem—in which the model did not account for geometric details and was based on strong idealizations. Conversely, in the present study, the coefficients have been identified through the sensitivity of

eigenvalues with respect to the damper characteristics, starting from a model representative of a generic medium-weight helicopter, incorporating a realistic kinematic description.

The results obtained further confirm the effectiveness of the I2B damper arrangement, as—despite employing dampers with inferior characteristics (see Table 4.8)—the same stability margins as in the BTH and IB configurations are achieved for the GR problem.

In this section, not only is a comparison between the different damper architectures performed for the nominal GR problem, but also the performance of the various configurations is analyzed and compared in different failure scenarios.

- One damper inoperative
- Two adjacent dampers inoperative
- Two non-adjacent dampers inoperative

4.4.2. One Damper Inoperative

The failure condition was modeled by removing the contributions of the first damper from both the damping and stiffness matrices of the system, written as an expression of the relative damper rotation φ.

$$\mathbf{C}_\varphi = \begin{bmatrix} \cancel{C_\varphi} & 0 & 0 & 0 & 0 \\ 0 & C_\varphi & 0 & 0 & 0 \\ 0 & 0 & C_\varphi & 0 & 0 \\ 0 & 0 & 0 & C_\varphi & 0 \\ 0 & 0 & 0 & 0 & C_\varphi \end{bmatrix} \tag{4.109}$$

$$\mathbf{K}_\varphi = \begin{bmatrix} \cancel{K_\varphi} & 0 & 0 & 0 & 0 \\ 0 & K_\varphi & 0 & 0 & 0 \\ 0 & 0 & K_\varphi & 0 & 0 \\ 0 & 0 & 0 & K_\varphi & 0 \\ 0 & 0 & 0 & 0 & K_\varphi \end{bmatrix} \tag{4.110}$$

As shown in the general formulation of the problem, starting from the kinematic relationship, the transformation matrix Ψ_φ was defined. This matrix allows us to directly link the rotation of the damper to the blade lead-lag angles.

Due to the resulting loss of isotropy in the rotor, the GR equations were then derived following the Floquet Formalism presented in § 2.5.

Having also defined an equivalent BTH geometry and tuned K_d and C_d to match the damping on ξ_{1c}, as done for the I2B configuration, the comparison under a failure scenario among the three damper configurations—BTH, IB, and I2B—is presented in Fig. 4.30.

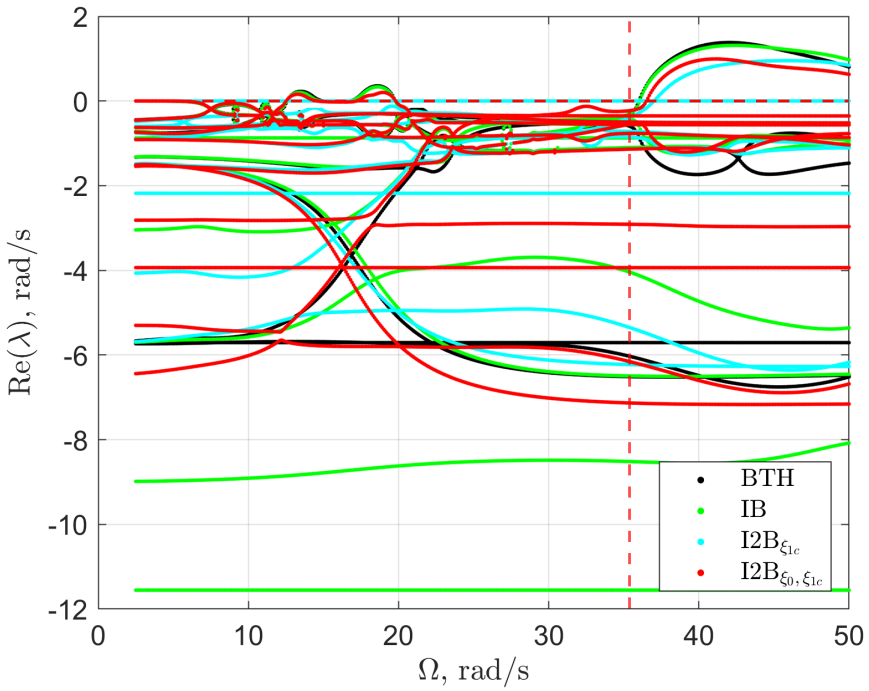

Figure 4.30: GR in case of damper failure, comparison between real part of eigenvalues for different damper configurations.

Figure 4.30 presents a comparison including two I2B configurations. The first, shown in cyan, corresponds to a case in which the collective mode remains undamped; this configuration does not exhibit low-RPM instability, unlike the BTH and IB architectures. The second, shown in red, includes damping on the collective mode and shows a dynamic response comparable to that of the BTH and IB cases. At higher RPM—beyond the nominal value—an instability region emerges, although it occurs at slightly higher rotational speeds and with reduced magnitude compared to the BTH and IB models. This behavior is consistent with the reduced damping characteristics employed in this I2B configuration, as summarized in Table 4.8. further quantitative details regarding the stability margin at nominal RPM and the peak real part of the unstable eigenvalues are reported in Table 4.9.

Table 4.9: Comparison between different architectures, one damper inoperative scenario.

Configuration	Re(λ) at nominal RPM	max Re(λ)	RPM at max Re(λ)
BTH (tuned)	-0.319 rad s^{-1}	$+1.381$ rad s^{-1}	400.87 RPM
IB (original)	-0.295 rad s^{-1}	$+1.314$ rad s^{-1}	404.68 RPM
I2B (tuned ξ_{1c})	-0.386 rad s^{-1}	$+0.952$ rad s^{-1}	437.59 RPM
I2B (tuned for ξ_0 and ξ_{1c})	-0.227 rad s^{-1}	$+0.993$ rad s^{-1}	392.47 RPM

4.4.3. Two Adjacent Dampers Inoperative

In this scenario is analyzed the failure of two consecutive dampers, starting from the general expression of the damping matrix, $\mathbf{C}_\varphi$, the failure condition is imposed as follows:

$$\mathbf{C}_\varphi = \begin{bmatrix} \cancel{C_\varphi} & 0 & 0 & 0 & 0 \\ 0 & \cancel{C_\varphi} & 0 & 0 & 0 \\ 0 & 0 & C_\varphi & 0 & 0 \\ 0 & 0 & 0 & C_\varphi & 0 \\ 0 & 0 & 0 & 0 & C_\varphi \end{bmatrix} \tag{4.111}$$

The same for the stiffness matrix in the relative damper rotation expression, $\mathbf{K}_\varphi$.

So independently from the damper arrangement, the failure condition is imposed for the four configurations as shown in Eq. (4.111), then the different problems are assembled with their respective coordinate transformation matrix Ψ_φ.

The results for the failure of two adjacent dampers, for the four different architectures, BTH tuned for damping on ξ_{1_c}, IB, I2B tuned on ξ_{1_c} and I2B tuned on ξ_0 and ξ_{1_c} are reported in Fig. 4.31.

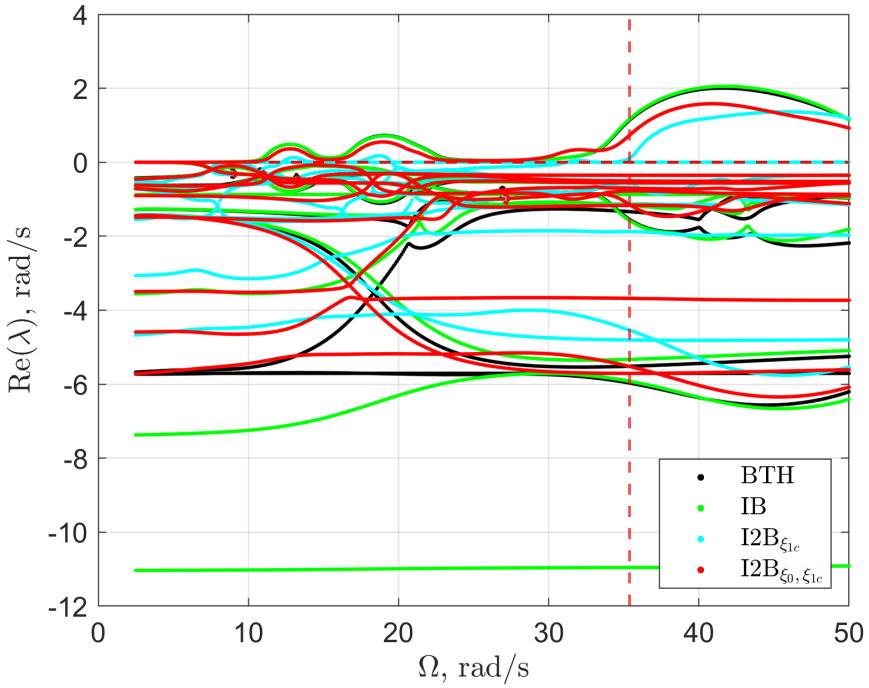

Figure 4.31: GR in case of two adjacent dampers failure, comparison between real part of eigenvalues for different damper configurations.

As in the single-damper failure case, the BTH, IB, and the I2B configuration tuned for both ξ_0 and ξ_{1_c} exhibit comparable behavior, with a localized instability region observed between 10 and 23 rad/s. In contrast, the I2B configuration tuned solely for ξ_{1_c} displays improved stability in the low RPM range.

Regarding the high-RPM instability, the ξ_{1_c}-only tuned I2B configuration exhibits a slightly more stable response compared to the BTH and IB cases, as the onset of instability occurs later respect the other configurations with lower magnitude.

Overall, the I2B architecture demonstrates enhanced stability characteristics. This improvement is attributed to higher residual damping in blades 1 and 2 (assuming failure of dampers 1 and 2), a consequence of the specific I2B geometry. In fact, under this failure scenario, the I2B layout ensures the presence of some residual damping in all blades. As a result, the primary instability shifts closer to the nominal angular velocity, adn results to be less critical if compared to the BTH and IB configurations.

The results for the 2 adjacent dampers failure problem are summarized in Table 4.10.

Table 4.10: Comparison between different architectures, two adjacent dampers inoperative.

Configuration	Re(λ) at nominal RPM	max Re(λ)	RPM at max Re(λ)
BTH (tuned)	+1.142 rad s^{-1}	+2.004 rad s^{-1}	397.25 RPM
IB (original)	+1.172 rad s^{-1}	+2.053 rad s^{-1}	398.20 RPM
I2B (tuned ξ_{1c})	+0.109 rad s^{-1}	+1.362 rad s^{-1}	437.35 RPM
I2B (tuned for ξ_0 and ξ_{1c})	+0.736 rad s^{-1}	+1.581 rad s^{-1}	390.56 RPM

In this particular failure scenario, the I2B arrangement demonstrates superior stability performance compared to the other two configurations. This is evident from the stability margin at the nominal RPM, which is less critical for the I2B case with respect to the BTH and IB configurations. Furthermore, the instability bubble exhibits a significantly lower magnitude in the I2B case.

4.4.4. Two non-Adjacent Dampers Inoperative

In this scenario is analyzed the failure of two non consecutive dampers, starting from the general expression of the damping matrix, $\mathbf{C}_\varphi$, the condition is imposed as:

$$\mathbf{C}_\varphi = \begin{bmatrix} \cancel{C_\varphi} & 0 & 0 & 0 & 0 \\ 0 & C_\varphi & 0 & 0 & 0 \\ 0 & 0 & \cancel{C_\varphi} & 0 & 0 \\ 0 & 0 & 0 & C_\varphi & 0 \\ 0 & 0 & 0 & 0 & C_\varphi \end{bmatrix} \tag{4.112}$$

The same for the stiffness matrix in the relative damper rotation expression, $\mathbf{K}_\varphi$. Now the inoperative dampers are the ones mounted on blades 1 and 3, in the section before were the ones on blades 1 and 2. The results of the GR equations for the four different arrangements are represented in Fig. 4.32.

Similarly to the previous case, the I2B configuration proves to be the most stable among the three arrangements, exhibiting only minor peaks at lower RPM, with the instability bubble appearing beyond the nominal RPM, even though the magnitude of instability is increased with respect to the other failure scenarios. It can be observed that the I2B configuration tuned only ξ_{1c} grants stability also at the nominal RPM. The stability margin of each configuration is reported in Table 4.11.

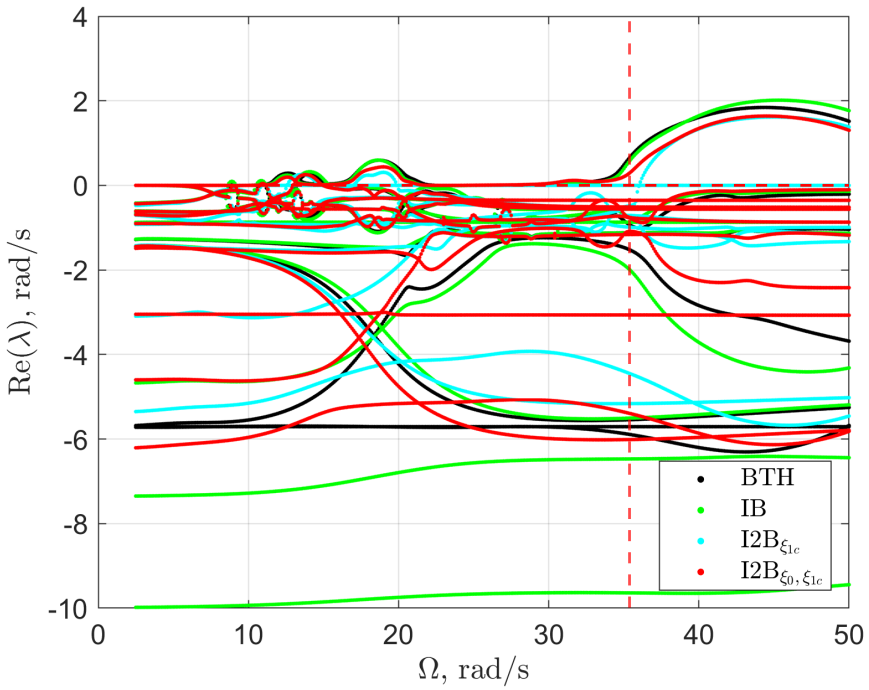

Figure 4.32: GR in case of two non-adjacent dampers failure, comparison between real part of eigenvalues for different damper configurations.

Table 4.11: Comparison between different architectures, two non-adjacent dampers inoperative.

Configuration	**Re(λ) at nominal RPM**	**max Re(λ)**	**RPM at max Re(λ)**
BTH (tuned)	$+0.662$ rad s^{-1}	$+1.842$ rad s^{-1}	423.98 RPM
IB (original)	$+0.584$ rad s^{-1}	$+2.014$ rad s^{-1}	432.58 RPM
I2B (tuned ξ_{1c})	-0.513 rad s^{-1}	$+1.617$ rad s^{-1}	429.71 RPM
I2B (tuned for ξ_0 and ξ_{1c})	$+0.296$ rad s^{-1}	$+1.640$ rad s^{-1}	424.94 RPM

5 | Analysis With Complete Aeroelastic Rotor Model

Ultimately, the damper kinematics—both for the IB and I2B configurations—are implemented within MASST, which provides high-fidelity rotor models. As a preliminary step, a comparison is conducted between ground resonance results obtained for the rotor in vacuo, i.e., neglecting aerodynamic contributions from the blades. This comparison aims to verify the consistency of the results with those derived from a Hammond-like model, while incorporating the realistic damper kinematics developed in Chapter 4.

In MASST, the dampers operate as control systems. A set of sensors, placed at specific nodes of the rotor grid, measures blade rotations and their velocities. The sensor outputs are passed to actuator transfer functions that encode the kinematic relationships of both the IB and I2B configurations. Based on these inputs, the transformation matrices and blade angular positions—expressed in the MBC frame—are computed, enabling the assembly of the complete ground resonance problem. Unlike the simplified Hammond model, which typically considers only the lag degrees of freedom, the MASST implementation supports full three-dimensional blade kinematics (flap, lag, and pitch), at least for the IB configuration, thus requiring an extended MBC transformation matrix $\mathbf{T}$.

The complete model couples the rotor dynamics (evaluated at discrete rotational speeds), the airframe with its rigid-body modes, the rotor–airframe interaction, and the lead–lag control system described above.

In the following, results are presented for both damper architectures (IB and I2B). First, the 2D analysis is shown for the rotor in vacuo. Subsequently, for the IB configuration, a 3D analysis is conducted that includes aerodynamic contributions and dynamic interactions, which cannot be captured by the classical Hammond-like problem formulation.

5.1. 2D Damper Models Comparisons

5.1.1. Interblade Comparison

In Fig. 5.1, the results obtained using the two different approaches are presented. The first refers to the GR problem, extended from the classical Hammond formulation by introducing additional degrees of freedom in the airframe model and considering more realistic kinematics; this solution is represented with a continuous line. The second approach is based on the MASST tool, where the results were computed for discrete values of the rotor angular velocity and are depicted using circular markers.

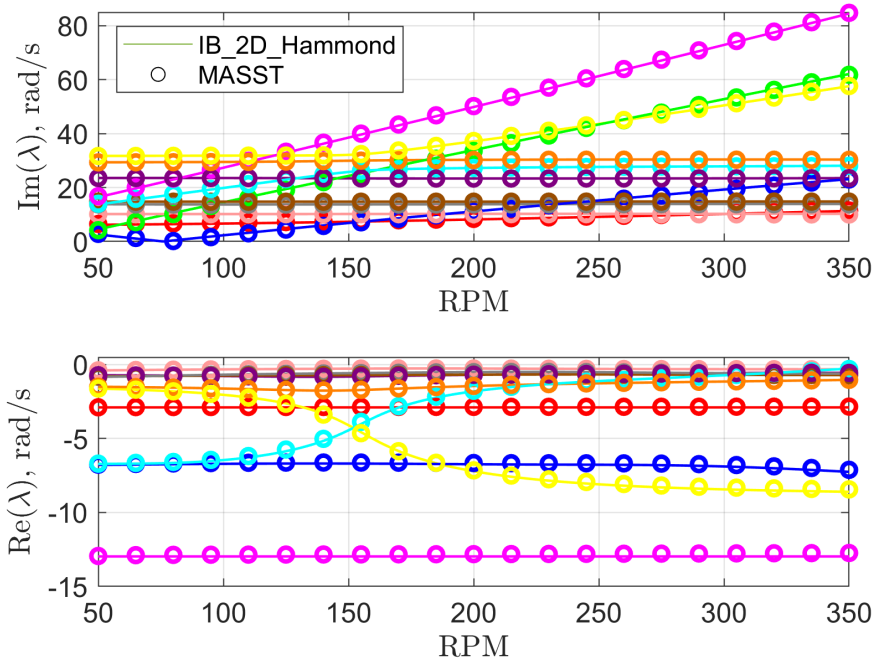

Figure 5.1: Comparisons of the real and imaginary part of eigenvalues

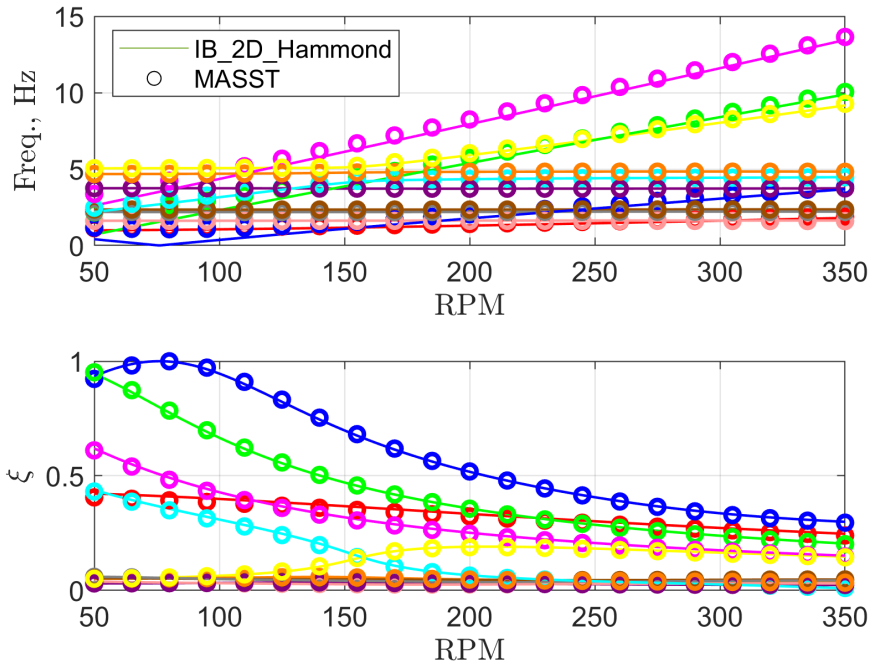

Figure 5.2: Comparison between damping factor ξ and frequency between the two methods

For both figures, it can be observed that the results obtained using the different tools are in good agreement.

5.1.2. Inter-2-Blade Comparison

The I2B asymmetrical architecture was also implemented in MASST, specifically the configuration tuned to provide the prescribed damping on the collective and regressive modes. The corresponding comparisons are reported below:

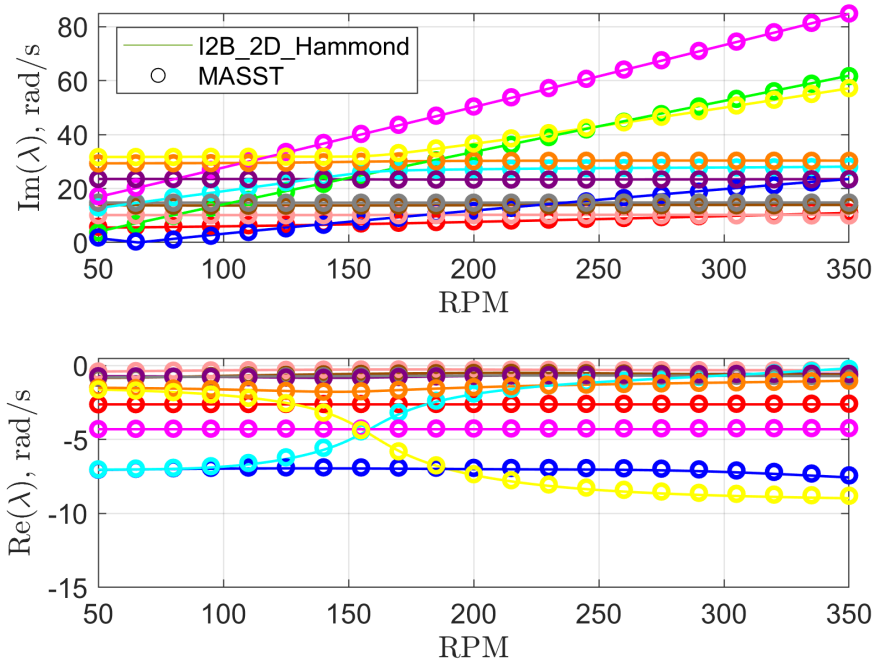

Figure 5.3: Comparisons of the real and imaginary parts of eigenvalues

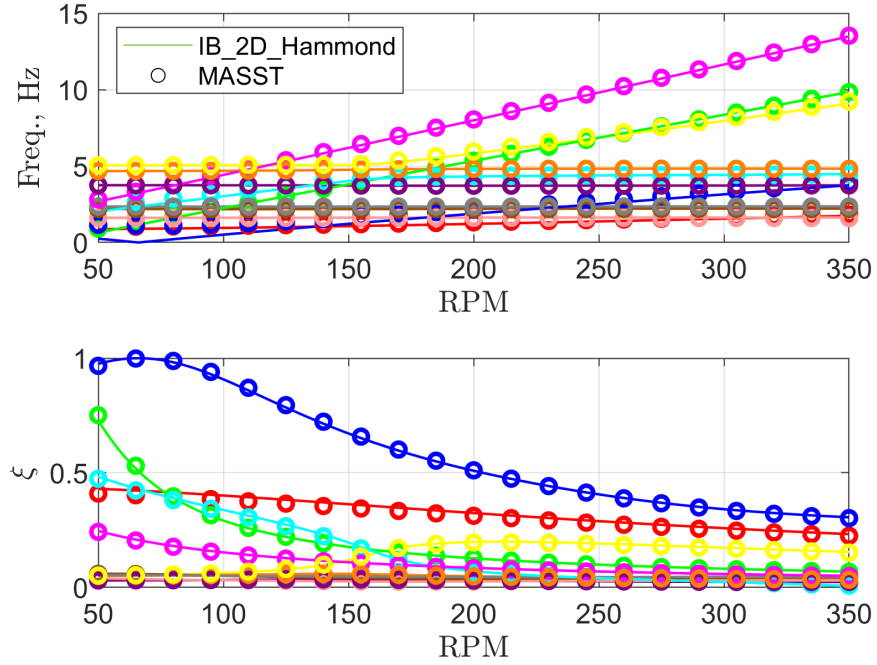

Figure 5.4: Comparison between damping factor ξ and frequency between the two methods

5.2. 3D Damper Models Comparions

5.2.1. Interblade 3D Model

For the IB configuration described in § 4.2, vertical offsets were introduced at the relevant kinematic points of the geometry to reproduce a fully three-dimensional kinematic model. This allowed for the generation and importation into MASST of a 3D representation of the damper, in which the classical GR equations were extended to include the blade flap and pitch angles—degrees of freedom that were previously neglected in the simplified Hammond-like problem.

This extension enabled the formulation of a new kinematic relationship, where the relative damper rotation $\varphi^{(m)}$ is influenced not only by the lag angles of blades m and $m+1$, denoted as $\xi^{(m)}$ and $\xi^{(m+1)}$, but also by their respective pitch and flap angles, $\theta^{(m)}, \theta^{(m+1)}$ and $\beta^{(m)}, \beta^{(m+1)}$.

Due to the introduction of this more comprehensive 3D kinematic model and the inclusion of aerodynamic properties in the rotor model within MASST, the new GR results are no longer directly comparable to those obtained from the classical Hammond model, which is based on a 2D formulation and neglects aerodynamic effects. Therefore, the updated GR predictions were compared with results from the industrial software CAMRAD-JA, which supports similar modeling capabilities, allowing for a meaningful comparison of the newly implemented approach.

In Fig. 5.5, the six rigid body modes are shown, along with the cyclic lag modes ξ_{1s} and ξ_{1c}, and the cyclic flap modes β_{1s} and β_{1c}. This was made possible by the implementation of a 3D kinematic model. Similarly to the lag modes, the regressive and cyclic flap modes are associated with the dimensionless flapping frequency:

$$\nu_\beta = \sqrt{1 + \frac{eS_\beta}{I_\beta} + \frac{k_\beta}{\Omega^2 I_\beta}} \tag{5.1}$$

where the terms correspond to the flap dynamics (analogous to those used in the lag analysis). This frequency is significantly higher than that of the dimensionless lag frequency ν_ξ, resulting in a pronounced separation between the two modes. The results obtained by the two methods correctly track the evolution of the cyclic and flapping regressive modes.

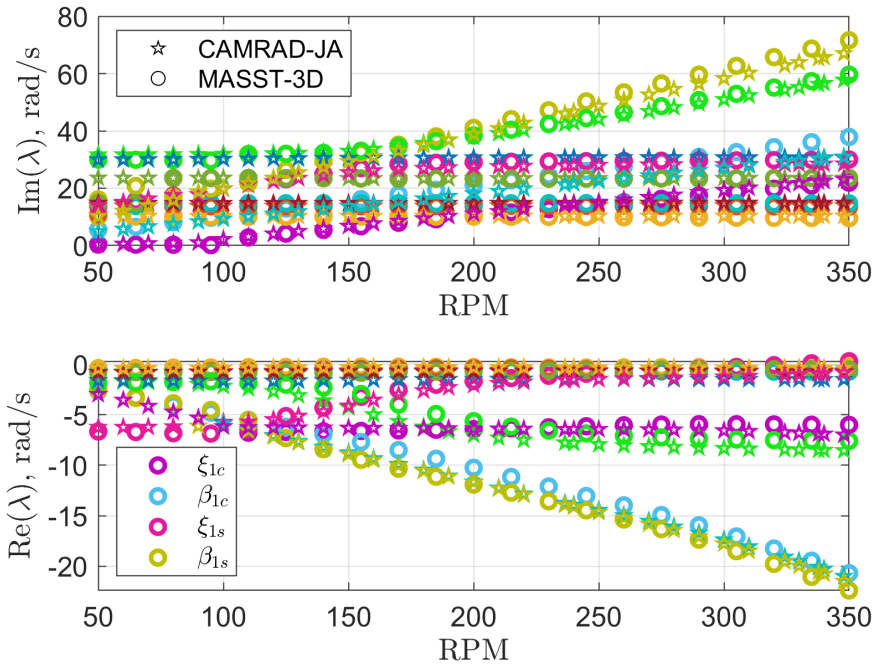

Figure 5.5: Comparisons of the real and imaginary parts of eigenvalues, CAMRAD-JA vs MASST.

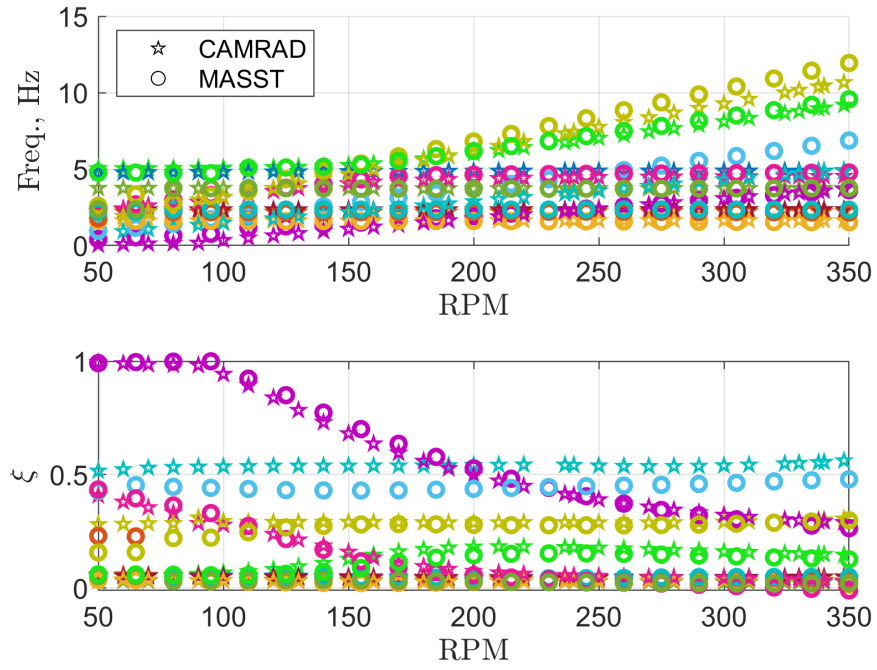

Figure 5.6: Comparison between damping factor ξ and frequency between the two methods.

6 | Conclusions and Future Developments

In the first chapters of this thesis, a brief overview of the ground resonance phenomenon was presented, outlining its physical nature and the derivation of its governing equations. This introductory framework was essential to clarify the role of lag dampers and how different damper architectures influence rotorcraft stability. The three primary configurations were introduced, and their stability behavior was analyzed under both nominal and failure conditions.

Once the mathematical models were established, a sensitivity-based approach was introduced, focusing on the eigenvalue problem's dependence on both geometrical and non-geometrical parameters. This method was directly applied to the ground resonance model, with results verified for the nominal case (ADO), while a mathematical formulation and preliminary results were also provided for the ODI problem. Building upon this sensitivity analysis, a refined kinematic model—representative of a medium-weight helicopter—was developed. This model incorporated both the IB and I2B damper kinematic configurations, enabling a more realistic assessment of their performance. Ground resonance simulations were performed for both configurations, providing comparative insights.

The sensitivity-based method was subsequently employed to optimize the geometry of the I2B configuration, with the aim of achieving stability performance comparable to the IB reference case. The optimization process successfully demonstrated that the I2B configuration, when properly tuned, can maintain the theoretical benefits initially predicted.

Finally, both damper kinematics were implemented in the MASST simulation environment, allowing for a higher-fidelity evaluation. At this stage, comparisons were performed in 2D, neglecting aerodynamic effects, to ensure consistency with the previous ground resonance models. Then for the IB kinematic model a 3D model, capable of introducing the influence of the pitch and flap angle of the blades was formulated in MASST and its GR results were compared employing another industrial software, CAMRAD-JA. This implementation represents a key step toward bridging the gap between theoretical studies and

full-system, high-fidelity simulations.

The work presented in this thesis provides additional insight into the I2B damping configuration. Its implementation in MASST represents a significant advancement, moving toward a more realistic and comprehensive analysis framework and laying the groundwork for future performance-based evaluations of real damper architectures.

In conclusion, this research has addressed previously unexplored aspects of inter-blade and inter-2-blade damping mechanisms, with a particular focus on the kinematic implementation. A realistic kinematic model has been developed, capable of reproducing the geometry of a modern medium-weight helicopter rotor.

The theoretical advantages of the I2B architecture—initially proposed in the literature—have been confirmed using the sensitivity-based optimization approach. Notably, the damper coefficients obtained are consistent with those reported in existing patents [13], thereby reinforcing the validity of the proposed methodology.

Moreover, the sensitivity method introduced here offers broad design potential, enabling tailored solutions while respecting realistic design constraints.

The next steps toward a practical implementation of this configuration should include:

- Extension to full 3D kinematic models also for the I2B tuned geometry, allowing for complete representation of blade motion.
- Inclusion of aerodynamic effects, to fully capture rotor-blade and rotor-airframe interactions.
- Integration of CAD/FEM-based analyses for structural stress evaluation on the dampers.
- Further investigations using MASST to explore coupled aeroelastic behaviors under operational conditions.

This thesis establishes a solid foundation for these future developments and contributes to advancing the understanding and design of alternative rotor damping architectures.

Bibliography

[1] A. Alvaro. A comparative study of the impact of innovative lead-lag damping configurations on helicopter stability and loads. Master's thesis, Politecnico di Milano, 2024. Academic Year 2023/24.

[2] G. Cassoni, A. Zanoni, A. Tamer, and P. Masarati. Stability of rotorcraft ground resonance by estimating Lyapunov characteristic exponents from multibody dynamics. In ASME IDETC/CIE 2022, St. Louis, Missouri, USA, August 14–17 2022. https://doi.org/10.1115/DETC2022-88995.

[3] R. P. Coleman. Theory of self-excited mechanical oscillations of hinged rotor blades. ARR 3G29, NACA, July 1943.

[4] R. P. Coleman and A. M. Feingold. Theory of self-excited mechanical oscillations of helicopter rotors with hinged blades. Report 1351, NACA, 1958.

[5] M. L. Deutsch. Ground Vibrations of Helicopters. Journal of the Aeronautical Sciences, 13(5):223–228, 1946. https://doi.org/10.2514/8.11359.

[6] Certification Specifications, Acceptable Means of Compliance and Guidance Material for Large Rotorcraft. European Union Aviation Safety Agency (EASA), 2024. URL `https://www.easa.europa.eu/en/document-library/certification-specifications/cs-29-amendment-11`. CS-29, Amendment 11.

[7] L. Frison, A. Zanoni, and P. Masarati. The inter-2-blade lead-lag damper concept. In 78th Forum of the Vertical Flight Society, Fort Worth, TX, USA, May 20–22 2022.

[8] L. A. Frison. Innovative damping system for lead-lag dynamics in articulated rotor. Master's thesis, Politecnico di Milano, 2021. Academic Year 2020/21.

[9] C. E. Hammond. An application of Floquet theory to prediction of mechanical instability. Journal of the American Helicopter Society, 19(4):14–23, 1974. https://doi.org/10.4050/JAHS.19.14.

[10] iStockPhoto. Main rotor su sfondo bianco, 2024. URL `https://www.istockphoto.`

com/it/foto/main-rotore-su-sfondo-bianco-gm175510280-20906786. Licenza iStock standard, immagine utilizzata a fini accademici.

[11] Jaypee. Main rotor head of eurocopter ec155. https://it.m.wikipedia.org/wiki/File:EC155_Main_rotor_head.jpg. Accessed: 2025-06-08.

[12] W. Johnson. Rotorcraft Aeromechanics. Cambridge University Press, 2013.

[13] P. Masarati and L. Frison. Rotore per elicottero a smorzamento migliorato, 2021. Italian Patent No. 102021000018017.

[14] P. Masarati and A. Zanoni. Projection continuation sensitivity for eigensolution continuation of multibody systems in minimal coordinate set form. In 7th International Conference on Multibody System Dynamics — IMSD 2024, Madison, WI, USA, June 9–13 2024.

[15] D. A. Peters and K. H. Hohenemser. Application of the Floquet transition matrix to problems of lifting rotor stability. Journal of the American Helicopter Society, 16 (2):25–33, 1971. https://doi.org/10.4050/JAHS.16.25.

[16] squorch. Ground resonance – rear view. https://youtu.be/D2tHA7KmRME?si=aQOFYTOM3fy-xLcK, 2006. Video.

[17] A. Tamer and P. Masarati. Periodic stability and sensitivity analysis of rotating machinery. In Proceedings of the 9th International Conference on Rotor Dynamics IFToMM ICORD 2014, Milan, Italy, September 22–25 2014. https://doi.org/10.1007/978-3-319-06590-8_170.

A | Kinematic Models for Hammond Problem

In this Appendix, the complete kinematic relations for both the IB and I2B configurations used in this thesis are reported. These expressions are reproduced from Appendix C of [1] to provide clarity and completeness in the current discussion.

For the IB model, the relations describe the connection between the lead-lag angles and the lengthening of the linear viscoelastic damper. For the I2B model, the relations refer instead to the coupling between the lead-lag motion and the rotation of the rotational damper.

A.1. Interblade Kinematic Relations

Considering the IB model illustrated in Fig. C.1, the origin of the kinematic framework is placed at the lead-lag hinge of blade $m+1$, which defines the global reference frame (depicted in gray). For each blade, two additional local reference frames are introduced:

- one associated with a generic lead-lag displacement, denoted by subscript 2;
- one corresponding to the reference configuration, i.e., zero lead-lag angle, denoted by subscript 1.

The positions of the damper attachment points for each blade, expressed in their respective local reference frames, are:

$$\mathbf{r}_2^B = \begin{bmatrix} b \\ c_b \\ 0 \end{bmatrix}, \tag{A.1}$$

$$\mathbf{r}_2^A = \begin{bmatrix} a \\ c_a \\ 0 \end{bmatrix}.$$

The rotation matrices describing the transformation from the reference configuration (subscript 1) to the current configuration (subscript 2) for the attachment points B_{i+1} and A_i are:

$$\mathbf{R}_{21}^{B} = \begin{bmatrix} \cos\xi_{i+1} & \sin\xi_{i+1} & 0 \\ -\sin\xi_{i+1} & \cos\xi_{i+1} & 0 \\ 0 & 0 & 1 \end{bmatrix}, \tag{A.2}$$

$$\mathbf{R}_{21}^{A} = \begin{bmatrix} \cos\xi_{i} & \sin\xi_{i} & 0 \\ -\sin\xi_{i} & \cos\xi_{i} & 0 \\ 0 & 0 & 1 \end{bmatrix}. \tag{A.3}$$

The transformation from the reference frame of each blade to the global frame (centered at the origin) is also a planar rotation matrix, defined by the angle ϕ, which is complementary to the inter-blade angular spacing $\Delta\psi$:

$$\mathbf{R}_{10}^{B} = \begin{bmatrix} \sin\phi & -\cos\phi & 0 \\ \cos\phi & -\sin\phi & 0 \\ 0 & 0 & 1 \end{bmatrix}, \tag{A.4}$$

$$\mathbf{R}_{10}^{A} = \begin{bmatrix} \sin\phi & -\cos\phi & 0 \\ \cos\phi & -\sin\phi & 0 \\ 0 & 0 & 1 \end{bmatrix}. \tag{A.5}$$

Having defined the required rotation matrices, the positions of the damper attachment points can now be expressed in the global reference frame of the kinematic model:

$$\mathbf{r}_{0}^{B} = \mathbf{R}_{10}^{B}\mathbf{R}_{21}^{B}\mathbf{r}_{2}^{B}, \tag{A.6}$$

$$\mathbf{r}_{0}^{A} = \mathbf{R}_{10}^{A}\mathbf{R}_{21}^{A}\mathbf{r}_{2}^{A} + \begin{bmatrix} l_e \\ 0 \\ 0 \end{bmatrix}. \tag{A.7}$$

The length of the damper l_i can be computed as the distance between the two attachment points, both expressed in the global reference frame:

$$\mathbf{l}_i = \mathbf{r}_{0}^{B} - \mathbf{r}_{0}^{A}. \tag{A.8}$$

Assuming small displacements, a linearization around the equilibrium condition can be

performed. This allows expressing the damper length l_i as a first-order approximation in terms of the lead-lag angles. The resulting coefficients, which link the damper extension velocity to the lead-lag angular velocities, are the same used in Appendix C:

$$l_i = \sqrt{\mathbf{l}_i \mathbf{l}_i^T} \approx L_0 + \left.\frac{\partial l_i}{\partial \xi_i}\right|_E \Delta\xi_i + \left.\frac{\partial l_i}{\partial \xi_{i+1}}\right|_E \Delta\xi_{i+1}. \tag{A.9}$$

The corresponding coefficients linking the damper length variation to the lead-lag angles are defined as:

$$L_{\xi A} = \frac{\partial l_i}{\partial \xi_i}, \tag{A.10}$$

$$L_{\xi B} = \frac{\partial l_i}{\partial \xi_{i+1}}. \tag{A.11}$$

A.2. Inter-2-Blade Kinematic Relations

With reference to the I2B model adopted for the analysis of the Hammond-like problem developed in Chapter 3, and shown in Fig. 3.1, this section derives the kinematic relations linking the lead-lag rotation of the blades to the relative rotation of the damper.

For this configuration, the origin of the coordinate system is located at the rotor hub. The global reference frame, denoted by the letter h, is highlighted in gray. Each local reference frame is labeled using a lowercase letter corresponding to the point it refers to, along with subscripts 1 and 2 to distinguish between the undeformed and deformed configurations, respectively.

The kinematic model considers the position of four key points: A_i, B_{i+2}, D_{i+1}, and F_{i+1}.

Considering the first blade, characterized by the azimuthal angle ξ_i, the point A_i in its local reference frame can be expressed as:

$$\mathbf{r}_2^A = \begin{bmatrix} -a & c_a & 0 \end{bmatrix}^T \tag{A.12}$$

The rotation matrix that allows us to transform from the local reference frame to the global reference frame, centered at the hub, is:

$$\mathbf{R}_{21}^{A} = \begin{bmatrix} \cos\xi_i & \sin\xi_i & 0 \\ -\sin\xi_i & \cos\xi_i & 0 \\ 0 & 0 & 1 \end{bmatrix} \tag{A.13}$$

$$\mathbf{R}_{10}^{A} = \begin{bmatrix} \cos\Delta\psi & \sin\Delta\psi & 0 \\ -\sin\Delta\psi & \cos\Delta\psi & 0 \\ 0 & 0 & 1 \end{bmatrix} \tag{A.14}$$

Once these two matrices are obtained, it is possible to express the position of the point A in the hub reference frame as:

$$\mathbf{r}_0^A = \mathbf{R}_{10}^A \left([0 \quad e \quad 0]^T + \mathbf{R}_{21}^A \mathbf{r}_2^A \right) \tag{A.15}$$

Where:

$$\Delta\psi = 2\pi / N_{\text{blades}} \tag{A.16}$$

The same can be done for the point B_{i+2}, belonging to the blade with azimuthal angle ξ_{i+2}, where the position in the local reference frame is:

$$\mathbf{r}_2^B = \begin{bmatrix} b & c_b & 0 \end{bmatrix}^T \tag{A.17}$$

The rotation matrices in this case are:

$$\mathbf{R}_{21}^{B} = \begin{bmatrix} \cos\xi_{i+2} & \sin\xi_{i+2} & 0 \\ -\sin\xi_{i+2} & \cos\xi_{i+2} & 0 \\ 0 & 0 & 1 \end{bmatrix} \tag{A.18}$$

$$\mathbf{R}_{10}^{B} = \begin{bmatrix} \cos\Delta\psi & -\sin\Delta\psi & 0 \\ \sin\Delta\psi & \cos\Delta\psi & 0 \\ 0 & 0 & 1 \end{bmatrix} \tag{A.19}$$

Therefore, the position in the hub reference frame is:

$$\mathbf{r}_0^B = \mathbf{R}_{10}^B \left([0 \quad e \quad 0]^T + \mathbf{R}_{21}^B \mathbf{r}_2^B \right) \tag{A.20}$$

As for the geometry related to the second blade, the central one, with azimuthal angle

ξ_{i+1}, the point D_{i+1} is expressed in the local reference frame as:

$$\mathbf{r}_2^D = \begin{bmatrix} d & 0 & 0 \end{bmatrix}^T \tag{A.21}$$

The rotation matrices are:

$$\mathbf{R}_{21}^D = \begin{bmatrix} \cos\gamma_D & -\sin\gamma_D & 0 \\ \sin\gamma_D & \cos\gamma_D & 0 \\ 0 & 0 & 1 \end{bmatrix} \tag{A.22}$$

and

$$\mathbf{R}_{10}^D = \begin{bmatrix} 0 & 1 & 0 \\ -1 & 0 & 0 \\ 0 & 0 & 1 \end{bmatrix} \tag{A.23}$$

Therefore, the position in the global hub reference frame is:

$$\mathbf{r}_0^D = \begin{bmatrix} 0 & e & 0 \end{bmatrix}^T + \mathbf{R}_{10}^D \left(\begin{bmatrix} c_d & 0 & 0 \end{bmatrix}^T + \mathbf{R}_{21}^D \mathbf{r}_2^D \right) \tag{A.24}$$

In a completely analogous way for the point F_i, with the parameters f, γ_F, and c_f.

$$\mathbf{r}_2^F = \begin{bmatrix} f & 0 & 0 \end{bmatrix}^T \tag{A.25}$$

The rotation matrices are:

$$\mathbf{R}_{21}^F = \begin{bmatrix} \cos\gamma_F & -\sin\gamma_F & 0 \\ \sin\gamma_F & \cos\gamma_F & 0 \\ 0 & 0 & 1 \end{bmatrix} \tag{A.26}$$

and

$$\mathbf{R}_{10}^F = \begin{bmatrix} 0 & 1 & 0 \\ -1 & 0 & 0 \\ 0 & 0 & 1 \end{bmatrix} \tag{A.27}$$

Therefore, the position in the global hub reference frame is:

$$\mathbf{r}_0^F = \begin{bmatrix} 0 & e & 0 \end{bmatrix}^T + \mathbf{R}_{10}^F \left(\begin{bmatrix} c_f & 0 & 0 \end{bmatrix}^T + \mathbf{R}_{21}^F \mathbf{r}_2^F \right) \tag{A.28}$$

. Once the position of each rod end is expressed in the global reference frame, the vectors representing the rods can be computed as:

$$\mathbf{l}_{AF} = \mathbf{r}_0^F - \mathbf{r}_0^A, \tag{A.29}$$

$$\mathbf{l}_{BD} = \mathbf{r}_0^D - \mathbf{r}_0^B. \tag{A.30}$$

Assuming small displacements and applying a linearization, it is possible to derive expressions for the dimensionless transmission coefficients $\Psi_{\xi\gamma_D}$ and $\Psi_{\xi\gamma_F}$. Under the hypothesis that the rods are sufficiently stiff, the contributions to damper rotation arising from the blade lead-lag angles and from the damper orientation must balance each other in magnitude but with opposite sign. This constraint ensures that the rod lengths remain constant.

As a result, the direct relationships used in Chapter 3 can be derived to relate the lead-lag motion of the blades to the damper rotation.

B | Comparison of Sensitivity Results

This Appendix contains the evaluation of the differences, for each geometrical parameter, between the eigenvalues obtained by solving the original GR system with a slight modification of the parameters (5% variation of the nominal value listed in Table 3.3) and those computed using the sensitivity results derived from solving the GR equation for the nominal scenario.

The parameter variation remains within a range that ensures that the system stays close to the equilibrium condition, where the linearization remains valid.

For each of the geometrical parameters for which the sensitivity was computed, the difference between the eigenvalue obtained through the direct solution and the one estimated via the sensitivity approach was evaluated as follows:

$$\lambda_{\text{baseline+sensitivity}} = \lambda_{\text{baseline}} + \frac{\partial \lambda}{\partial p}(p - p_0), \tag{B.1}$$

$$\text{difference} = \lambda_{\text{direct}} - \lambda_{\text{baseline+sensitivity}}, \tag{B.2}$$

where λ_{direct} denotes the eigenvalue obtained directly from the solution of the ground resonance problem with the perturbed parameter p.

B.1. Chordwise Position of Damper Attachment Points

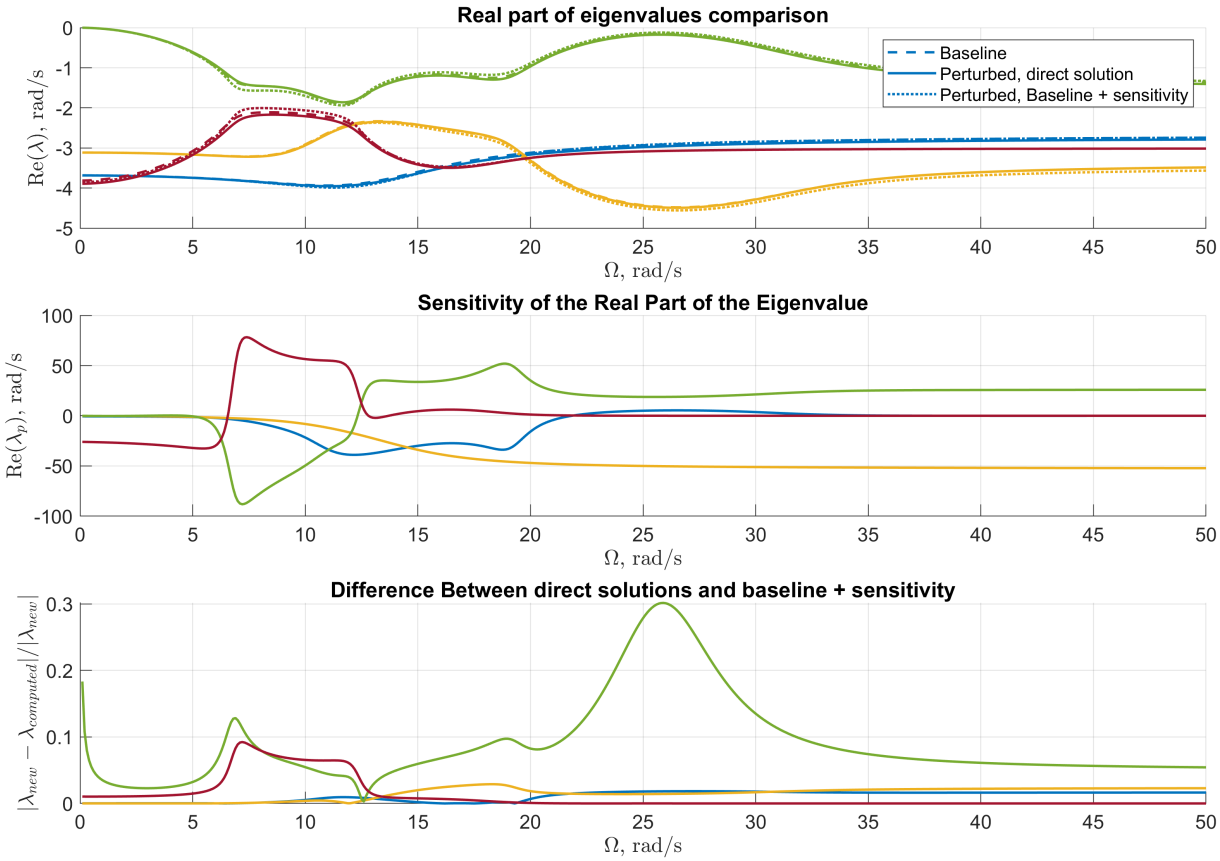

Figure B.1: Eigenvalues evolution, real part of the sensitivity with respect to chordwise perturbation and difference between results, for a positive perturbation of parameter a

Due to symmetry considerations, since the sensitivity of the eigenvalues respect the chordwise positive, as well for all the other geometrical parameters is the same independently from the side only one case for each parameter is reported.

As can be observed, the method accurately approximates the eigenvalues. The weighted difference between the newly obtained eigenvalues and the computed ones remains low. The high peak around 0.3 for the critical eigenvalue can be justified by the fact that, in reality, the absolute difference is minimal (on the order of 1/100). However, since the eigenvalue itself is very small, this results in a noticeable peak.

All these results were considered for a 5% variation of the nominal parameter, which corresponds to an actual difference of around 4 mm for the chordwise parameter.

B.2. Radial Position of Damper Attachment Points

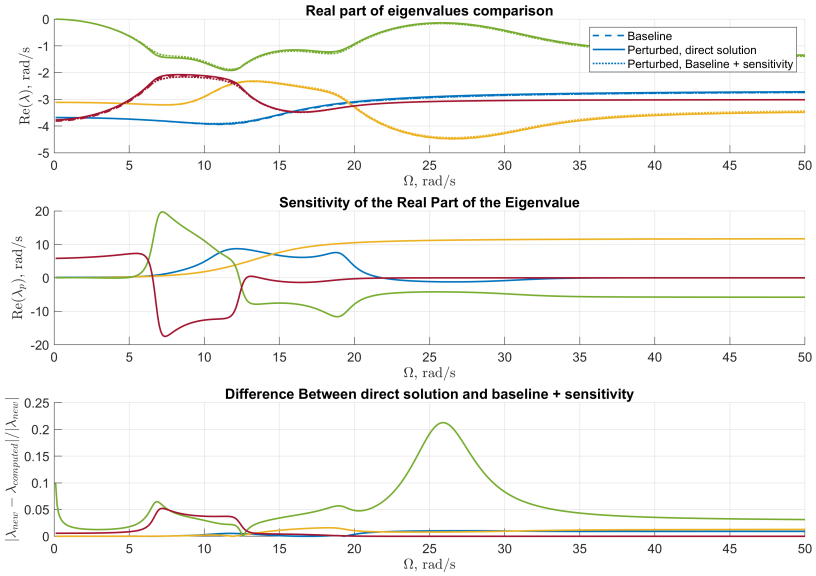

Figure B.2: Eigenvalues evolution, real part of the sensitivity with respect to radial perturbation and difference between results, for a positive perturbation of parameter c_a

B.3. Middle Arms Length

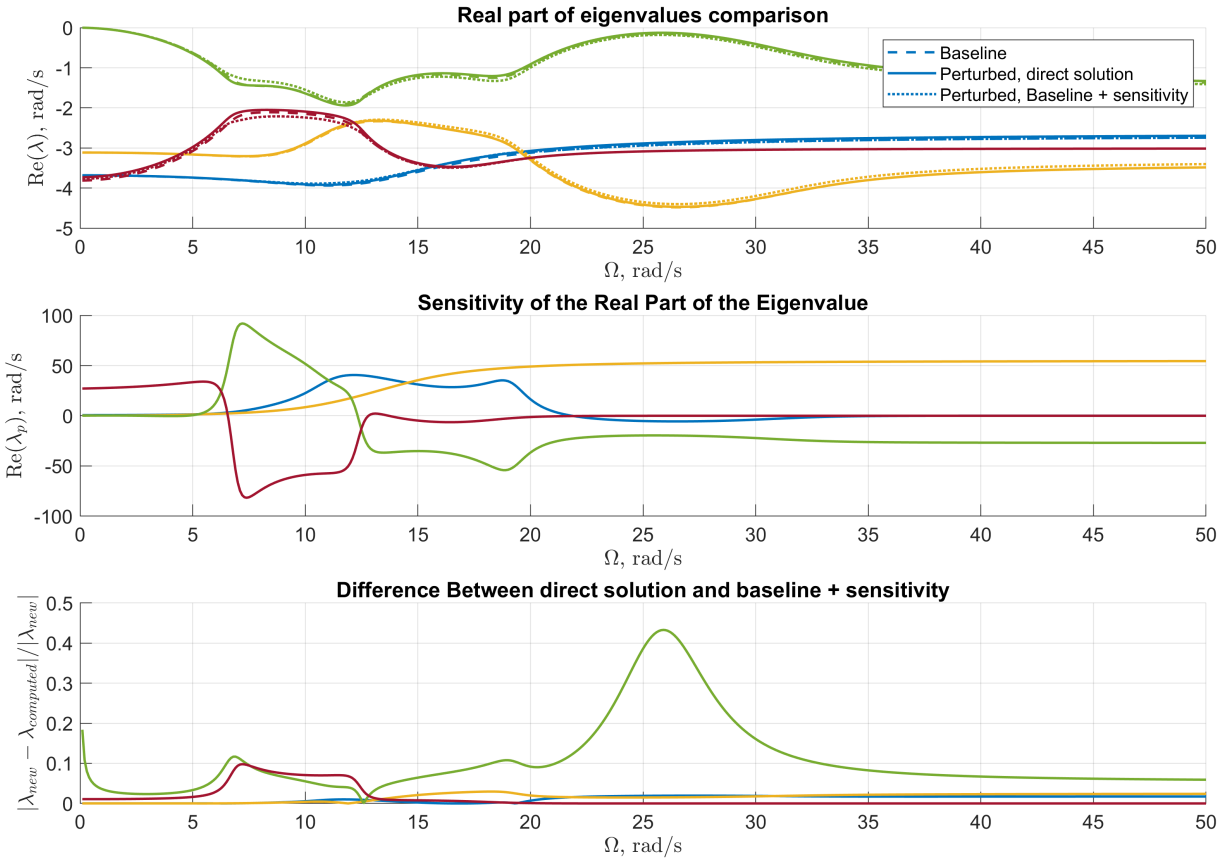

Figure B.3: Eigenvalues evolution, real part of the sensitivity with respect to middle arms length perturbation and difference between results, for a positive perturbation of parameter d

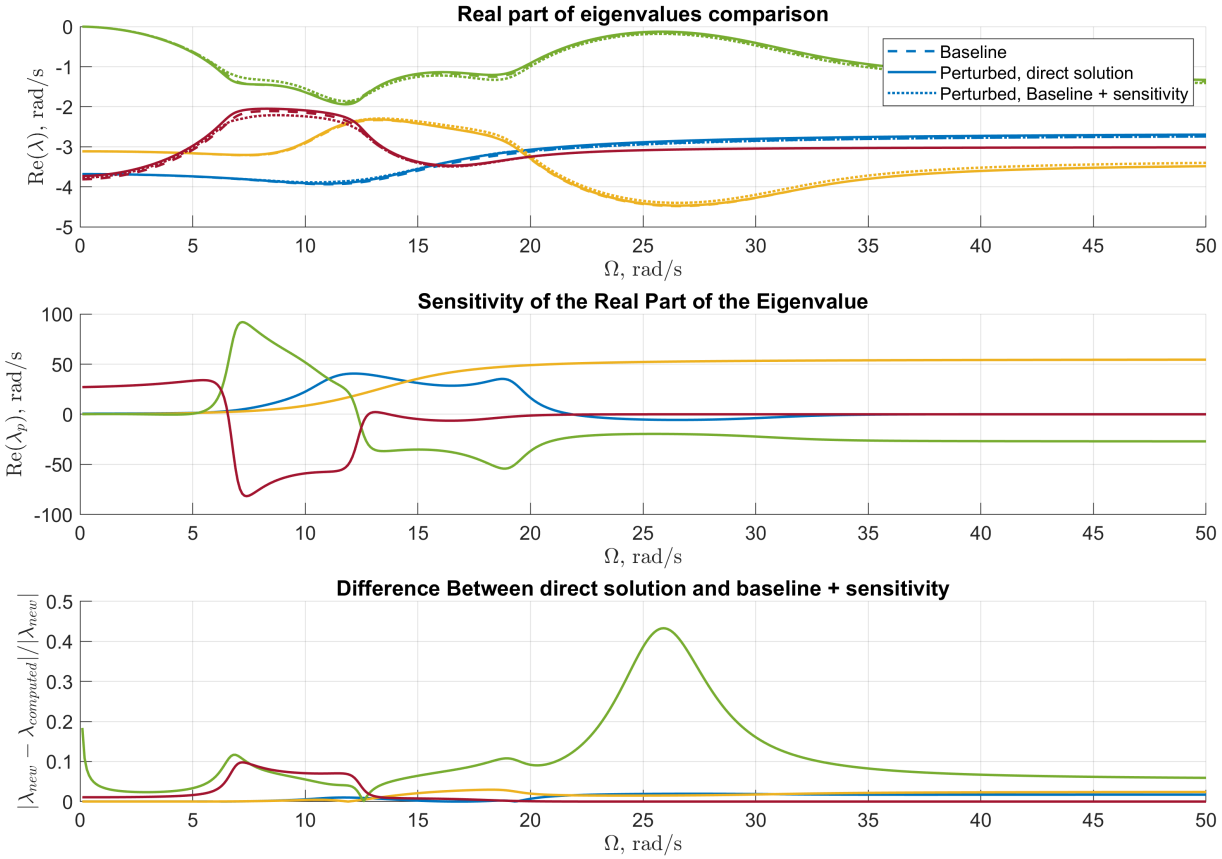

Figure B.4: Eigenvalues evolution, real part of the sensitivity with respect to middle arms length perturbation and difference between results, for a positive perturbation of parameter f

B.4. Hinge Middle Blade

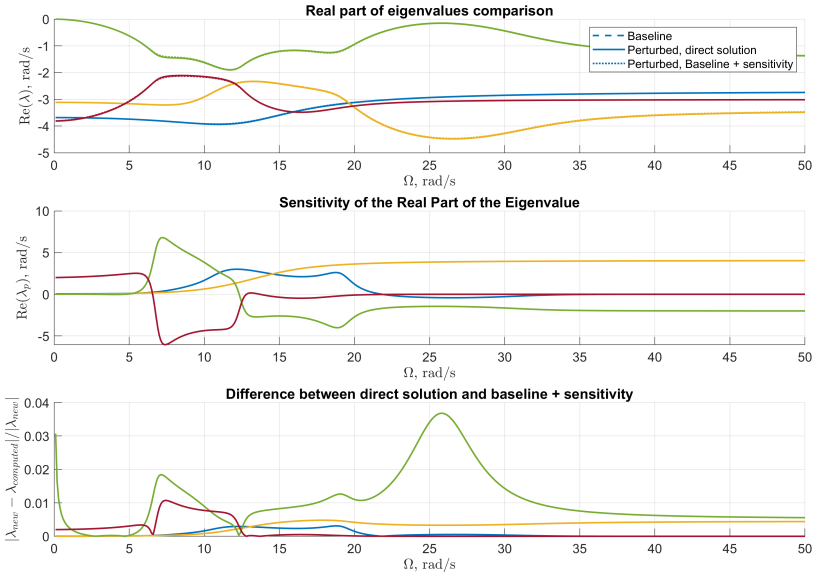

Figure B.5: Eigenvalues evolution, real part of the sensitivity with respect to hinge offset on the middle blade and difference between results, for a positive perturbation of parameter c_d

B.5. Sensitivity of Stiffness Terms

This section reports the sensitivity and evolution of the critical eigenvalues due to perturbations of the stiffness terms of the joints in the model presented in Section 4.2. For each joint, results are shown first for a strong perturbation of 15% of the nominal stiffness value, followed by a slight perturbation of 1%.

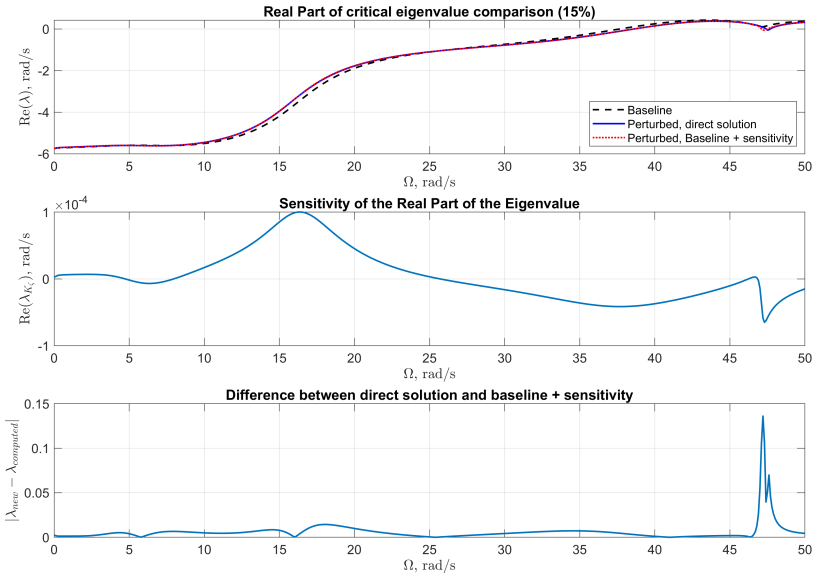

Figure B.6: Sensitivity of the critical eig to K_ζ ($\Delta K = 15\%\ K_{\mathrm{d}_{\mathrm{nominal}}}$)

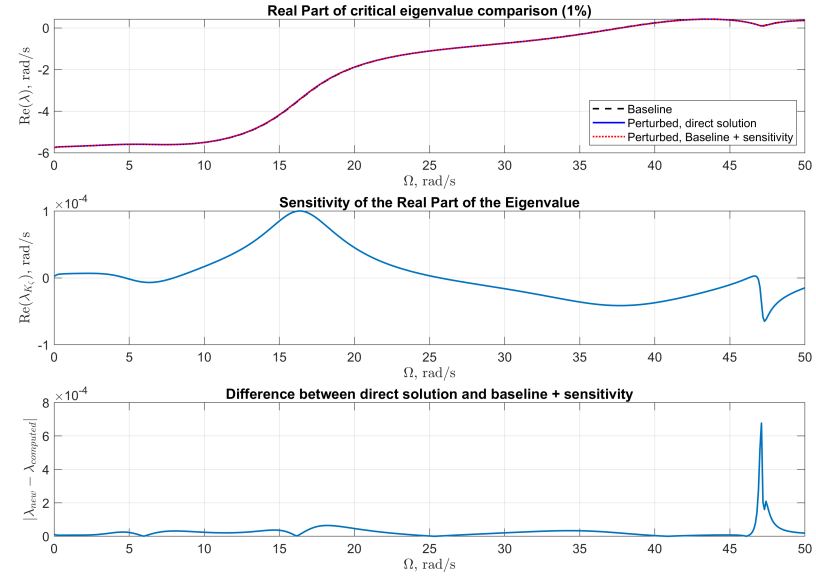

Figure B.7: Sensitivity of the critical eig to K_ζ ($\Delta K = 1\%\ K_{\mathrm{d}_{\mathrm{nominal}}}$)

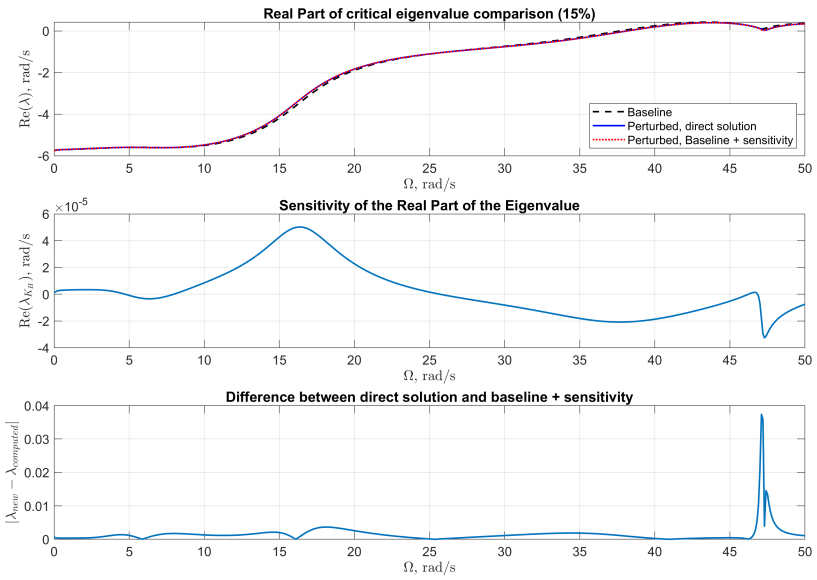

Figure B.8: Sensitivity of the critical eig to K_H ($\Delta K = 15\%\ K_{\mathrm{d}_{\mathrm{nominal}}}$)

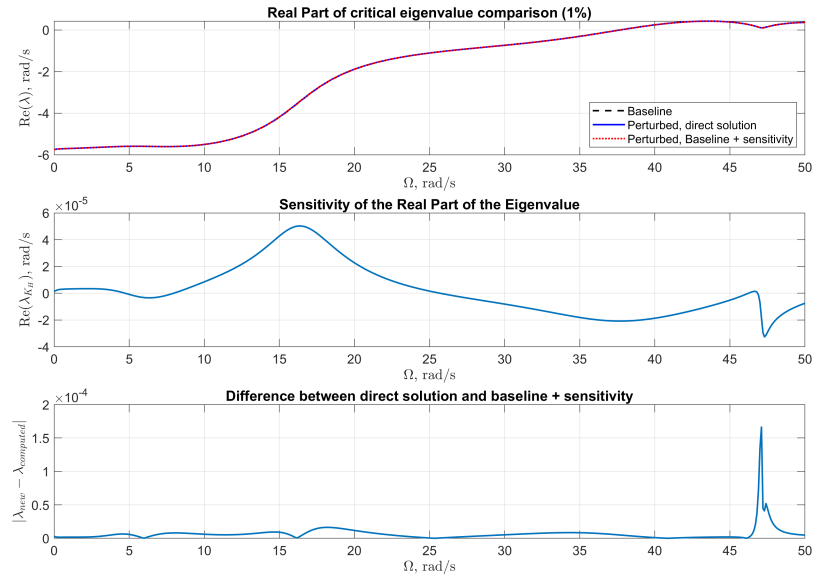

Figure B.9: Sensitivity of the critical eig to K_H ($\Delta K = 1\%\ K_{\mathrm{d}_{\mathrm{nominal}}}$)

B.6. Sensitivity of Damping Terms

This section reports the sensitivity and evolution of the critical eigenvalues due to perturbations of the damping terms of the joints in the model presented in § 4.2. For each joint,

results are shown first for a strong perturbation of 15% of the nominal stiffness value, followed by a slight perturbation of 1%.

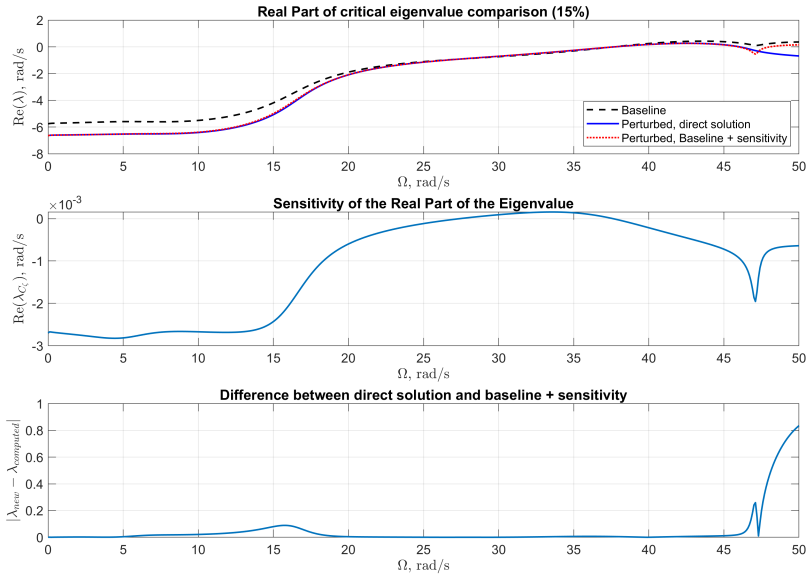

Figure B.10: Sensitivity of the critical eig to C_ζ ($\Delta K = 15\%\ C_{\mathrm{d}_{\mathrm{nominal}}}$)

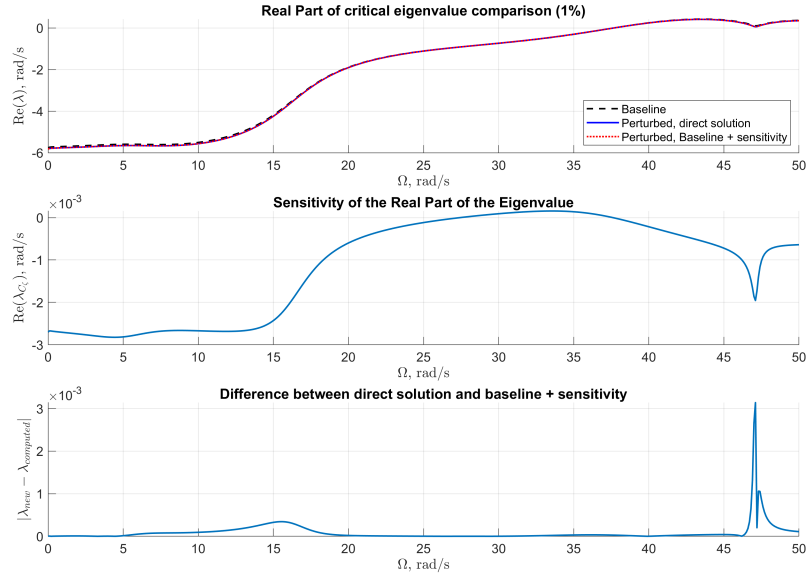

Figure B.11: Sensitivity of the critical eig to C_ζ ($\Delta C = 1\%\ C_{\mathrm{d}_{\mathrm{nominal}}}$)

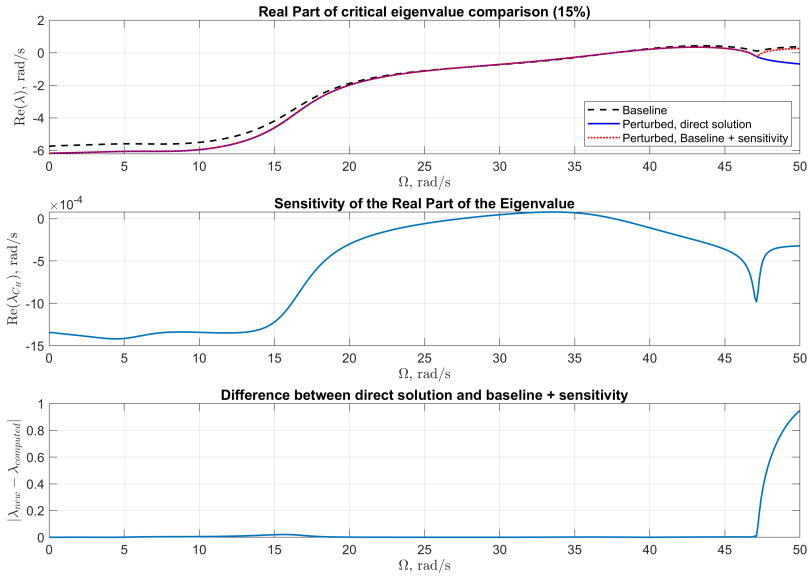

Figure B.12: Sensitivity of the critical eig to C_H ($\Delta C = 15\%\ C_{\mathrm{d_{nominal}}}$)

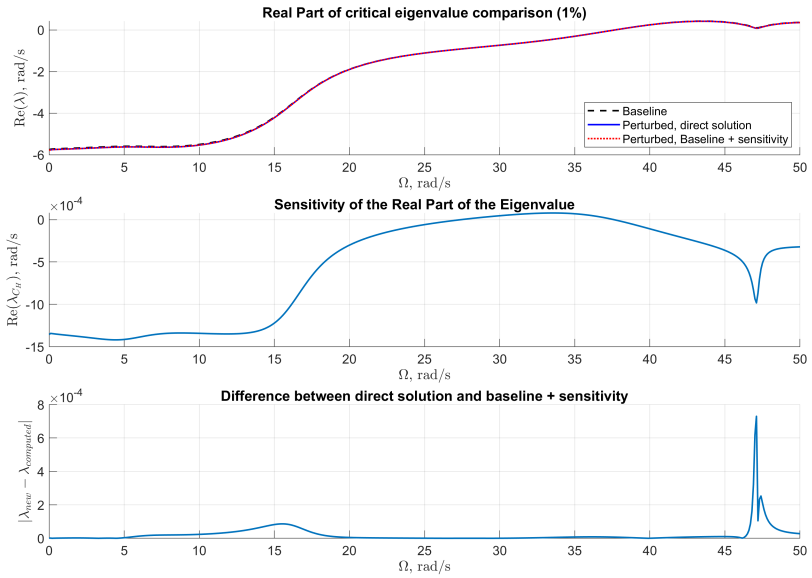

Figure B.13: Sensitivity of the critical eig to C_H ($\Delta C = 1\%\ C_{\mathrm{d_{nominal}}}$)

C | Sensitivity of Loads to Geometrical Parameters

The application of the sensitivity approach is not limited to the analysis of the system's eigenvalues and, consequently, to the assessment of dynamic stability, but it also proves useful in evaluating how variations in system parameters affect the loads transmitted by the damper to the blade.

In this Appendix, starting from the general formulation of the IB and I2B problem and still referring to the Hammond rotor data (see Table 3.1), the influence of geometric modifications in the damper kinematics on the load transfer from the rotor to the blade is investigated.

C.1. Interblade Load Formulation

To enable a comparison between the two configurations, IB and I2B—as previously done for the I2B case in Fig. 3.1—a general IB kinematic model must first be introduced.

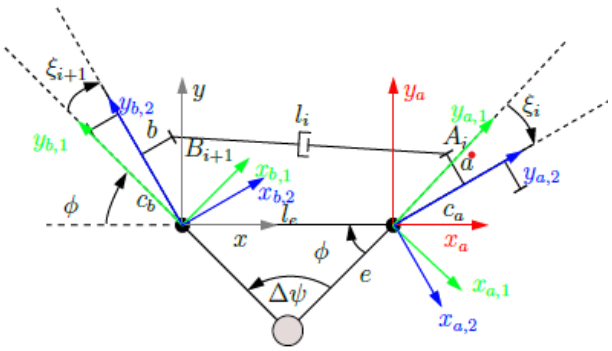

Figure C.1: General IB damper arrangement with respective local reference frames

Compared to the I2B configuration, which was analyzed in Chapter 3, in this scenario, the relation between the azimuth angle and the damping moment arises from the lengthening

velocity of the viscous damper, rather than from a relationship between the angle of the rotational damper and the lead-lag angles.

The length of the damper can be expressed as a function of:

$$l_i = f(\xi_i, \xi_{i+1}, N_b, a, c_a, b, c_b) \tag{C.1}$$

Fewer parameters are involved compared to the I2B scenario, but its sensitivity can be studied to observe how, for the same geometrical values, variations in these parameters affect the load transmitted from the damper to the airframe.

The damper can be assumed to follow the following constitutive law:

$$F_{d,i} = K_{d,i}(l_i - l_o) + C_{d,i}\dot{l}_i, \tag{C.2}$$

where l_i represents the distance between the attachment points of the damper on the two arms. The position along the blade, as in the I2B case, is determined by the parameters a and c_a, respectively: the chordwise attachment positions of the blade to the damper and the radial attachment positions at the damper.

C.2. Inter-2-Blade Load Formulation

As previously stated, given the chosen damper configuration, the I2B scenario differs from the IB configuration in that the damper is rotational. In the I2B case, the damping moment arises from the relative rotation of the damper, differently from the lengthening velocity of the IB problem. Based on the geometric relationships defining the damper in the I2B configuration, it is possible to express the angular rotation of the damper on the central blade—identified by the azimuthal angle ξ_i—as the sum of the angles γ_D and γ_F, determined through the following expressions:

$$\gamma_D = \Psi_{\xi\gamma_D}\xi_{i+1} \tag{C.3}$$

$$\gamma_F = \Psi_{\xi\gamma_F}\xi_{i-1} \tag{C.4}$$

where the two azimuthal angles represent the angles of the previous and next blades relative to the central blade, ξ_i.

The dimensionless coefficients that relate the azimuthal angle to the damper angle on the central blade depend on several geometric parameters, which are condensed into this

dimensionless proportionality coefficient. Therefore, the dependence of these coefficients on the individual geometric parameters has been analyzed, following an approach similar to the one used in the study of the sensitivity of the eigenvalues with respect to the same parameters.

C.3. Loads Formulation and Setup of the Sensitivity Problem

The load generated on the damper i can be defined as follows:

$$\varphi_i = K\theta + C\dot{\theta} \tag{C.5}$$

This expression represents the constitutive law of a purely viscous damper. Independent from the configuration—IB or I2B—, the first term, multiplied by the coefficient K, is related to the stiffness, while the second is related to the damping. The load can be a function of different variables:

- **Interblade configuration:** The load depends on the damper length l_i and its derivative $\dot{l}_i$.
- **Inter-2-blade configuration:** The load is a function of the angles at the middle blade, γ_D and γ_F, along with their derivatives.

For the IB case, the expression becomes:

$$\varphi_{i,\mathrm{IB}} = K_{\mathrm{IB}} \left(L_{\xi B}\xi_{i+1} - L_{\xi A}\xi_i\right) + C_{\mathrm{IB}} \left(L_{\xi B}\dot{\xi}_{i+1} - L_{\xi A}\dot{\xi}_i\right) \tag{C.6}$$

where $L_{\xi B} = \frac{\partial l_i}{\partial \xi_{i+1}}$ and $L_{\xi A} = \frac{\partial l_i}{\partial \xi_i}$, more information regards the kinematic model for the IB problem can be found in Appendix A.

In the I2B configuration, θ is given by the two angles corresponding to the damper rotation on the central blade:

$$\theta = \gamma_D - \gamma_F \tag{C.7}$$

Thus, substituting into equation Eq. (C.5), the load expression can be rewritten as:

$$\varphi_{i,\mathrm{I2B}} = K_{\mathrm{I2B}}(\Psi_{\xi\gamma_D}\dot{\xi}_{i+1} - \Psi_{\xi\gamma_F}\dot{\xi}_{i-1}) + C_{\mathrm{I2B}}(\Psi_{\xi\gamma_D}\dot{\xi}_{i+1} - \Psi_{\xi\gamma_F}\dot{\xi}_{i-1}) \tag{C.8}$$

C.3.1. Expression of n-th Harmonic Load and its Sensitivity to p

Equations C.6 and C.8 present the damper loads as explicit functions of the blades' azimuthal positions. While this formulation clearly relates the loads to the instantaneous angular positions of each blade, it is more insightful and practical to express these loads in terms of their harmonic content.

By decomposing the loads into a sum of harmonic components, one can analyze and interpret the influence of each harmonic order on the overall rotor dynamics.

To set the stage for this harmonic decomposition, the general azimuthal angle $\xi^{(m)}$ associated with the mth blade is defined as follows:

$$\xi^{(m)} = \xi_0 + \sum_{n=-\infty}^{+\infty} \xi_n e^{jn(\Omega t + m\Delta\psi)} \tag{C.9}$$

where $\Delta\psi = 2\pi/N_{\text{blades}}$.

As for the lead-lag angular velocity of the mth blade:

$$\dot{\xi}^{(m)} = j\Omega \sum_{n=-\infty}^{+\infty} n\xi_n e^{jn(\Omega t + m\Delta\psi)} \tag{C.10}$$

That is, the azimuthal angle is expressed as a contribution of infinite harmonics, each harmonic contribution being characterized by its amplitude ξ_n.

Substituting the expressions from Eq. (C.9) and Eq. (C.10) into Eqs. (C.6) and (C.8) yield a relation that represents the load transmitted from the damper to the airframe in terms of harmonic components.

By focusing specifically on the azimuthal angles $\xi^{(0)}$ and $\xi^{(2)}$, and isolating the contribution of the nth harmonic, the general expression for the load, for the I2B formulation, transmitted from the ith damper to the corresponding blade can be written as:

$$\varphi_{n,\text{I2B}} = \xi_n e^{jn\Omega t}\Big(K_{\text{I2B}}(\Psi_{\xi\gamma_D} - \Psi_{\xi\gamma_F} e^{2jn\Delta\psi}) + jn\Omega C_{\text{I2B}}(\Psi_{\xi\gamma_D} - \Psi_{\xi\gamma_F} e^{2jn\Delta\psi})\Big) \tag{C.11}$$

A similar expression is obtained for the load transmitted by the damper in the IB configu-

ration, where the relevant azimuthal positions are $\xi^{(0)}$ and $\xi^{(1)}$. The general nth harmonic load can be expressed as follows:

$$\varphi_{n,\mathrm{IB}} = \xi_n e^{jn\Omega t}\Big(K_{\mathrm{IB}}(L_{\xi B} - L_{\xi A}e^{jn\Delta\psi}) + jn\Omega C_{\mathrm{IB}}(L_{\xi B} - L_{\xi A}e^{jn\Delta\psi})\Big) \tag{C.12}$$

Once the individual harmonic contribution has been isolated, recognizing that the geometric dependence is contained within the coefficients L_ξ for the IB configuration and Ψ_ξ for the I2B configuration, the sensitivity of the nth harmonic load with respect to a generic geometric parameter p for the IB problem can be expressed as:

$$\varphi_{n,\mathrm{IB}/p} = K_{\mathrm{IB}}(L_{\xi B/p} - L_{\xi A/p}e^{jn\Delta\psi}) + jn\Omega C_{\mathrm{IB}}(L_{\xi B/p} - L_{\xi A/p}e^{jn\Delta\psi}) \tag{C.13}$$

where the derivative with respect to the parameters p is evaluated as follows:

$$\frac{\partial L_{\xi B}}{\partial p} = \frac{\partial}{\partial p}\left(\frac{\partial \|B - A\|}{\partial \xi_i}\right) \tag{C.14}$$

due to its simpler geometry, the only parameters considered for differentiation will be c_a, c_b, a, b from Table 3.1.

For the I2B problem instead, by factoring out the oscillatory term $\xi_n e^{jn\Omega t}$, the expression simplifies to:

$$\varphi_{n,\mathrm{I2B}/p} = K_{\mathrm{I2B}}(\Psi_{\xi\gamma_D/p} - \Psi_{\xi\gamma_F/p}e^{2jn\Delta\psi}) + jn\Omega C_{\mathrm{I2B}}(\Psi_{\xi\gamma_D/p} - \Psi_{\xi\gamma_F/p}e^{2jn\Delta\psi}) \tag{C.15}$$

where the derivative with respect to the parameters p is evaluated as follows:

$$\frac{\partial \Psi_{\xi\gamma_D}}{\partial p} = \frac{\partial}{\partial p}\left(-\frac{\frac{\partial \|F-A\|}{\partial \xi_{i-1}}}{\frac{\partial \|F-A\|}{\partial \gamma_F}}\right) \tag{C.16}$$

The derivatives of this dimensionless coefficient will be evaluated with respect to the following geometric parameters, which are considered influential with regard to the kinematics of the damper. Subsequently, the sensitivity of the load with respect to this coefficient will be analyzed. The parameters under consideration are the same as those in Table 3.1.

C.4. Load Sensitivity Results

The sensitivity of the load coefficient with respect to key geometrical parameters was investigated for both rotor configurations: IB and I2B.

In each case, the sensitivity of the modulus of the nth harmonic component was evaluated with respect to selected geometrical parameters, considering both the contribution associated with the stiffness coefficient K and that related to the damping factor C.

The expression under analysis was the following:

$$|\varphi_n|_{/p} = \left(\sqrt{\mathrm{Re}(\varphi_n)^2 + \mathrm{Im}(\varphi_n)^2}\right)_{/p} = \frac{\mathrm{Re}(\varphi_n)\mathrm{Re}(\varphi_n)_{/p} + \mathrm{Im}(\varphi_n)\mathrm{Im}(\varphi_n)_{/p}}{|\varphi_n|} \tag{C.17}$$

where the real part of the nth harmonic is given by the sum of the real part of the K and C coefficients expressed in Eq. (C.13) and Eq. (C.15).

According to Eq. (C.15), the damping factor C exhibits a dependence on Ω, meaning that at higher angular speeds, its influence becomes more significant. In the results shown below, Figs. C.2 and C.3 report the values for a nominal angular velocity of $\Omega = 40$ rad/s.

Furthermore, due to its dependence on the harmonic order n, higher-order harmonics contribute more significantly to the overall response.

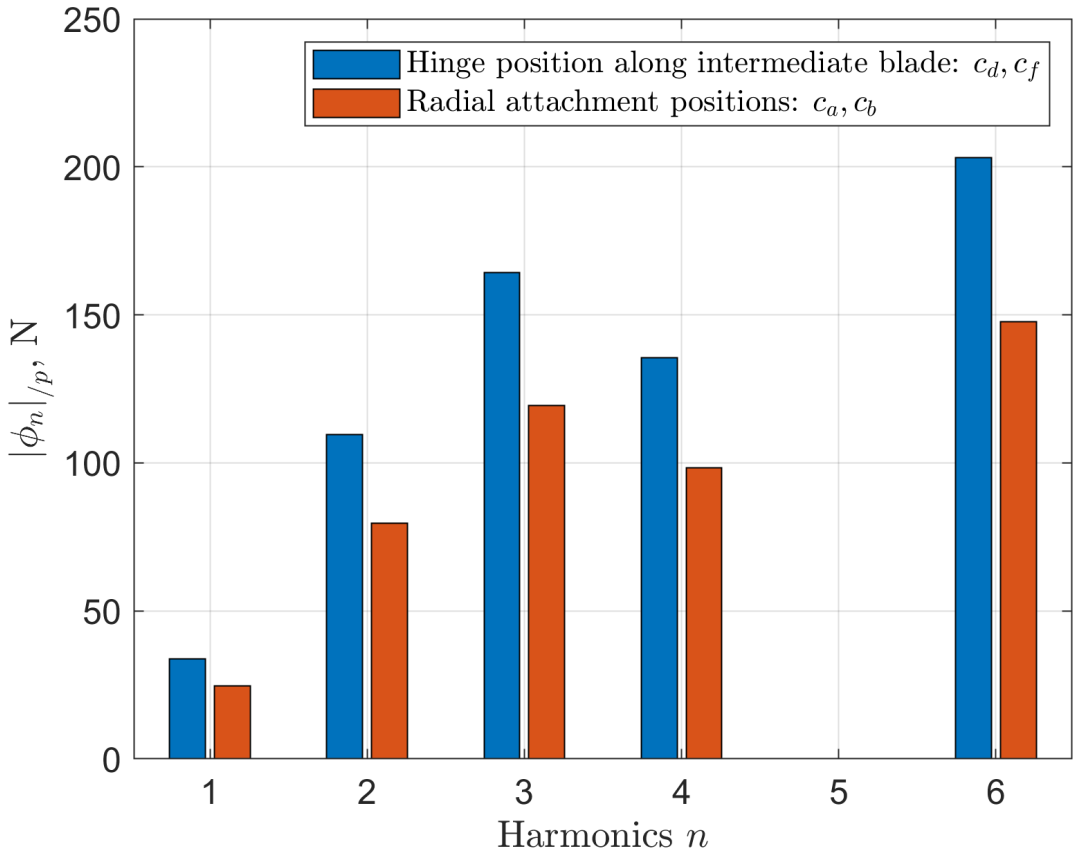

Figure C.2: Sensitivity of the modulus of the nth harmonic respect the key geometrical parameters, IB configuration

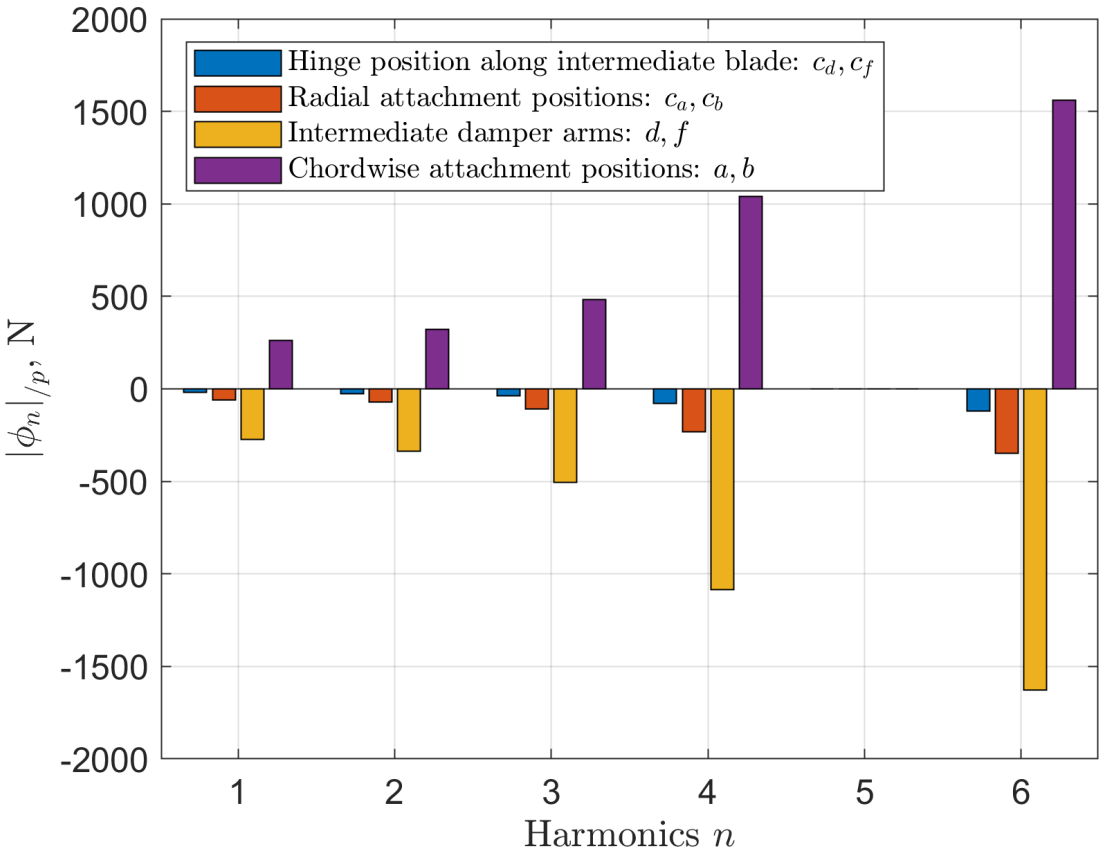

Figure C.3: Sensitivity of the modulus of the nth harmonic respect the key geometrical parameters, IB configuration, I2B configuration

For both results, the contribution of the 5th harmonic disappears. This occurs because the exponential term associated with the harmonic provides only a real unitary contribution, corresponding to a five-blade rotor. This term multiplies the dimensionless coefficient in the expressions for the same geometrical parameters.

The reason the 5th harmonic vanishes lies in the type of expression used to investigate sensitivity. Observing Eq. (C.17), we note that there is a product between the real and imaginary parts of the nth harmonic contribution and its derivative with respect to parameter p. While the derivative itself is not zero, as stated earlier, it is zero relative to the nth load expression.

Since $|\Psi_{\xi\gamma_D}| = |\Psi_{\xi\gamma_F}|$ due to the symmetry of the problem, and for the 5th harmonic where the exponential term provides a purely unitary contribution, the resulting term is zero, making the overall expression vanish.

Regarding the sensitivity of the modulus, it can be observed that for both the IB and I2B

dampers, there is a growing contribution related to the harmonic content. Specifically, the higher the harmonic order, the greater the sensitivity. This behavior is embedded in the expression for the damping coefficient, which directly depends on the harmonic order.

List of Figures

List of Tables

List of Symbols

Variable	Description	SI unit
θ	Pitch angular rotation	rad
β	Flap angular rotation	rad
ξ	Lag angular rotation	rad
φ	Relative damper rotation	rad
Ω	Angular velocity of main rotor	rad/s
$\Delta\psi$	Angle between blades	rad
ψ	Azimuthal position	rad
λ	Eigenvalue	rad/s
ω	Natural frequency	Hz
ζ	Damping ration	-
γ_F, γ_D	Rotation of damper for I2B problem	rad

List of Acronyms

BTH	Blade To Hub
IB	Interblade
I2B	Inter-Two-Blade
GR	Ground Resonance
VWP	Virtual Work Principle
ADO	All Dampers Operative
ODI	One Damper Inoperative
MBC	Multi Blade Coordinates
GDC	Generalized Deutsch Criterion
LTP	Linear Time Periodic
EASA	European Union Aviation Safety Agency